

POWERED PARAGLIDER LONGITUDINAL
DYNAMIC MODELING AND EXPERIMENTATION

By

COLIN P. GIBSON

Bachelor of Science in Mechanical and Aerospace

Engineering

Oklahoma State University

Stillwater, OK

2014

Submitted to the Faculty of the
Graduate College of the
Oklahoma State University
in partial fulfillment of
the requirements for
the Degree of
MASTER OF SCIENCE
December, 2016

POWERED PARAGLIDER LONGITUDINAL
DYNAMIC MODELING AND EXPERIMENTATION

Thesis Approved:

Dr. Andrew S. Arena

Thesis Adviser

Dr. Joseph P. Conner

Dr. Jamey D. Jacob

Name: COLIN P. GIBSON

Date of Degree: DECEMBER, 2016

Title of Study: POWERED PARAGLIDER LONGITUDINAL DYNAMIC MODELING
AND EXPERIMENTATION

Major Field: MECHANICAL AND AEROSPACE ENGINEERING

Abstract: Paragliders and similar controllable decelerators provide the benefits of a compact packable parachute with the improved glide performance and steering of a conventional wing, making them ideally suited for precise high offset payload recovery and airdrop missions. This advantage over uncontrollable conventional parachutes sparked interest from Oklahoma State University for implementation into its Atmospheric and Space Threshold Research Oklahoma (ASTRO) program, where payloads often descend into wooded areas. However, due to complications while building a powered paraglider to evaluate the concept, more research into its design parameters was deemed necessary. Focus shifted to an investigation of the effects of these parameters on the flight behavior of a powered system.

A longitudinal dynamic model, based on Lagrange's equation for adaptability when adding free-hanging masses, was developed to evaluate trim conditions and analyze system response. With the simulation, the effects of rigging angle, fuselage weight, center of gravity (cg), and apparent mass were calculated through step thrust input cases. Test flights evaluated the behavior of the paraglider, and the design was revised based on observations and analysis. Rigging angle sets the power-off glide slope as well as thrust capacity and input response damping. At more negative angles the glide slope is steeper, can handle more thrust, and damps quicker at a lower frequency. The fuselage weight, or loading, affects thrust capacity and power-off sink rate, with heavier gliders capable of larger thrust inputs but faster descent speed; however, the glide slope remains unchanged. As the cg position is placed forward of the attachment point the incidence angle and thrust line will rotate downward, while the opposite occurs moving aft. For the test vehicle, a slightly forward position allowed for the greatest thrust input, and far forward reduced performance for equivalent thrust compared to far aft. Three test flights were performed. The paraglider displayed lateral oscillations due to fuselage-parafoil twisting and wing anhedral, despite its inherent keel effect. A wider parafoil mounting configuration provides increased twist resistance, which can otherwise cause sideslips and dihedral induced rolling, and adjusted rigging reduced wing arc.

TABLE OF CONTENTS

Chapter	Page
1. INTRODUCTION	1
1.1. Motivation.....	1
1.2. Objectives	2
1.3. Background	3
1.3.1. Conventional Parachutes.....	3
1.3.2. Rogallo Wings	4
1.3.3. Parafoils	5
1.3.4. Paraglider Applications.....	6
2. REVIEW OF LITERATURE	8
2.1. Wind Tunnel Tests.....	8
2.1.1. Nicolaides	8
2.1.2. Furfaro et al.....	10
2.1.3. Uddin & Mashud.....	13
2.2. Aerodynamic Coefficients	14
2.3. Computational Fluid Dynamics	16
2.4. “Apparent Mass”.....	18
2.5. Glide Angle.....	20
2.6. Paraglider Steering.....	23
2.7. Throttle Only Control	24
2.8. Dynamic Models.....	25
2.8.1. Quisenberry.....	26
2.8.2. Chambers	26
2.9. Lagrange Equation	29
3. EQUIPMENT & DESIGN.....	34
3.1. Paraglider Test Vehicle.....	34
3.1.1. Components	34
3.1.2. Mass Properties	38
3.2. Powerplant Sizing and Testing	39
3.3. Line Rigging	45

Chapter	Page
4. ANALYSIS.....	49
4.1. Incidence Angle	49
4.2. System.....	51
4.3. Aerodynamic Data	59
4.4. Analytical Model	61
4.5. Simulation.....	67
4.6. Validation.....	71
5. RESULTS	76
5.1. Simulation Analyses	76
5.1.1. Rigging Angle.....	76
5.1.1.1. Effect on Glide Performance	76
5.1.1.2. Effect on Thrust Capacity & Climb	79
5.1.1.3. Effect on Dynamic Response.....	83
5.1.2. Weight & Loading	85
5.1.2.1. Effect on Thrust Capacity & Climb	85
5.1.2.2. Effect on Dynamic Response.....	86
5.1.3. Center of Gravity	88
5.1.3.1. Effect on Thrust Capacity & Climb	89
5.1.3.2. Effect on Dynamic Response.....	90
5.1.4. “Apparent Mass” Effects	91
5.2. Experiments	94
5.2.1. First Flight Test.....	94
5.2.1.1. Wing Arc.....	94
5.2.1.2. Torque Induced Rotation	95
5.2.2. Second Flight Test	99
5.2.2.1. Mounting Configuration	100
5.2.2.2. Wing Anhedral.....	105
5.2.2.3. Comparison to Simulation	106
5.2.3. Third Flight Test	108

6. CONCLUSIONS & FUTURE WORK.....	109
6.1. Conclusions.....	109
6.1.1. Rigging Angle.....	109
6.1.2. Weight & Loading	110
6.1.3. Center of Gravity	110
6.1.4. Apparent Mass Effects.....	111
6.1.5. Vehicle Stability.....	111
6.1.6. Dynamic Model	111
6.2. Future Work	112
 REFERENCES	 113
 APPENDICES	 116
Appendix A: Figures.....	116
Appendix B: Simulation Guide.....	122
Appendix C: Mathcad Simulation Code	129

LIST OF TABLES

Table	Page
Table 1: Furfaro Test Wing Sections	10
Table 2: 8x6 3-Blade Propeller Powerplant Data	44
Table 3: 10x5 3-Blade Propeller Powerplant Data	44
Table 4: 12x6 3-Blade Propeller Powerplant Data	44
Table 5: 1 st Flight Port-Side Line Lengths (inches)	47
Table 6: 1 st Flight Starboard-Side Line Lengths (inches)	47
Table 7: 2 nd Flight Port-Side Line Lengths (inches)	47
Table 8: 2 nd Flight Starboard-Side Line Lengths (inches)	47
Table 9: 3 rd Flight Port-Side Line Lengths (inches).....	47
Table 10: 3 rd Flight Starboard-Side Line Lengths (inches).....	47
Table 11: Analysis of Dynamic Response 0.75 to 0 lb	85
Table 12: Sink Rate and Glide Path for Differing Weights	88
Table 13: Coefficients for Parafoil Wing [11]	119

LIST OF FIGURES

Figure	Page
Figure 1: Rigid Rogallo Wings [4]	4
Figure 2: Lift Curve from Nicolaides Experiments [8].....	9
Figure 3: Drag Curve from Nicolaides Experiments [8].....	9
Figure 4: Lift to Drag Plot from Nicolaides Experiments [8].....	10
Figure 5: Lift Curve from Furfaro Experiments [9].....	11
Figure 6: Drag Curve from Furfaro Experiments [9].....	11
Figure 7: Drag Polar from Furfaro Experiments [9]	12
Figure 8: Turbulator Effect on Drag Polar [9]	12
Figure 9: Lift to Drag Ratio vs. Alpha from Furfaro Data [9]	12
Figure 10: Inflated Parafoil at Various Angles of Attack [10].....	13
Figure 11: Parafoil Variation of Internal Pressure with Angle of Attack [10].....	14
Figure 12: Comparison of Flight Data to Calculated Coefficients [11].....	16
Figure 13: Comparison of Flight Data to Calculated Coefficients with Correction Factor [11] ...	16
Figure 14: Lift and Drag Curves from CFD Analysis [14]	17
Figure 15: Lift to Drag Ratio from CFD Analysis [14]	17
Figure 16: Lift and Drag Curves for CFD Analysis Between Differing Airfoil Shapes [14]	18
Figure 17: Lift to Drag Ratio for CFD Analysis Between Differing Airfoil Shapes [14]	18
Figure 18: Lift and Drag Curves for CFD Analysis With and Without Leading Edge Cut [14] ..	18
Figure 19: Lift to Drag Ratio for CFD Analysis With and Without Leading Edge Cut [14]	18
Figure 20: Apparent Mass Components and Related Variables [15].....	20
Figure 21: Simple Paraglider Model.....	21
Figure 22: Paraglider with Fly-bar [18]	23
Figure 23: Paraglider with Steering Line [18]	23
Figure 24: Turn Rate and Direction with Brake Deflection [17]	24
Figure 25: Simple Pendulum in Cartesian Coordinates	31
Figure 26: Simple Pendulum in Polar Coordinates.....	31
Figure 27: Paraglider Trike.....	35
Figure 28: NTM 35-36A 1400KV Performance Data	35
Figure 29: Hobby King Parafoil	36
Figure 30: Ozone Quattro Parafoil.....	37
Figure 31: Reference Point for Measuring Component Locations	39
Figure 32: Powerplant Testing Configuration	41
Figure 33: Powerplant Thrust Output with Throttle Input.....	43

Figure	Page
Figure 34: Powerplant Current Draw with Throttle Input	44
Figure 35: Ozone Quattro Parafoil Rigging Configuration.....	46
Figure 36: Ozone Quattro Parafoil with Reduced Arc Anhedral	47
Figure 37: Reference for Line Designations	48
Figure 38: Wing Represented as a 4-Bar Mechanism.....	50
Figure 39: Wing Represented with Rigid Geometry Joining at a Single Point.....	50
Figure 40: Double Pendulum	52
Figure 41: Proposed System	53
Figure 42: Fuselage Center of Gravity Definition	55
Figure 43: Forces Acting on Proposed System with Angles and Dimensions.....	56
Figure 44: Simulation Flow Chart	69
Figure 45: Sample of Some Simulation Outputs	70
Figure 46: Vertical Velocity Response Comparison.....	73
Figure 47: Horizontal Velocity Response Comparison	73
Figure 48: Steady State Climb Comparison.....	74
Figure 49: Rigging Angle Effect on Angle of Attack and Lift to Drag Ratio	78
Figure 50: Relationship between Angle of Attack, Rigging Angle, and Lift to Drag Ratio.....	78
Figure 51: Glide Angle for Nicolaides' Parafoil with Changes in Rigging Angle.....	79
Figure 52: Rigging Angle Effect on Angle of Attack with Thrust Input	80
Figure 53: Rigging Angle Effect on Total Velocity with Thrust Input.....	80
Figure 54: Rate of Climb for Thrust Input with Given Rigging Angle	81
Figure 55: Climb Rate Based on Rigging Angle and Thrust	82
Figure 56: Flight Path Angle Based on Rigging Angle and Thrust	82
Figure 57: Dynamic Response for Step Thrust Input from 0.75 to 0 lb.....	83
Figure 58: Analysis of Dynamic Response 0.75 to 0 lb.....	84
Figure 59: Vertical Velocities and Maximum Thrust Values with Various Fuselage Weights	86
Figure 60: Fuselage and Wing Pitch Angles at Maximum Thrust by Weight	86
Figure 61: Dynamic Response for 0.75 to 0 lb of Thrust with Various Fuselage Weights	87
Figure 62: Center of Gravity Natural Pitch Behavior	88
Figure 63: Glide Slope Angle and Climb Rate for Varying cg Positions at 0.75 lb of Thrust	89
Figure 64: Maximum Thrust and Climb Rate at Max Thrust for Varying cg Positions	90
Figure 65: Dynamic Response for 0.75 to 0 lb of Thrust with Varying cg Location	91
Figure 66: Dynamic Response for 0 to 0.75 lb of Thrust with Varying cg Location	91
Figure 67: Dynamic Response for a Paraglider with and without “Apparent Mass”	92
Figure 68: Parafoil Anhedral	94
Figure 69: Dihedral Effect [26].....	95
Figure 70: Bungees Under Load from Paraglider Torque	96
Figure 71: Lateral Paraglider System for Torque Analysis	97
Figure 72: Free Body Diagram for Torque Rotation Analysis	99
Figure 73: Modified Parafoil Attachment Bracket	100
Figure 74: Applied Torque to Torsional Spring.....	101
Figure 75: Separation of Rigging lines in Longitudinal Plane.....	102

Figure	Page
Figure 76: Yawing Paraglider Parafoil Attachment Bracket	103
Figure 77: 3-Dimensional View of Yawing Twist.....	103
Figure 78: Yaw Induced Sideslip.....	105
Figure 79: In Flight Rigging and Parafoil Pitch Angles	106
Figure 80: Ozone Quattro Rigging.....	107
Figure 81: Rigging Angle for Test Flight 3	108
Figure 82: Nicolaides Models 8-13 Section Coordinates [7].....	116
Figure 83: Nicolaides Model 8-13 Wing Section [7].....	117
Figure 84: Furfaro Parafoil Cross-Section [9]	117
Figure 85: Furfaro Parafoil Truncated Nose Dimensions [9]	118
Figure 86: External Pressure Distribution for Wings at Various Angles of Attack [10]	118
Figure 87: Powerplant Power Output with Throttle Input	119
Figure 88: Endurance for Throttle Input with 4000 mAh Battery	120
Figure 89: XFOIL Analysis of 1412 and 2412 Airfoils.....	121

CHAPTER 1

INTRODUCTION

1.1. MOTIVATION

Descent vehicles with conventional decelerators, such as round parachutes, provide a safe method of transferring payloads from high altitude to the ground; however, while some are steerable, they are limited in the amount of control authority available. Ram-air parachutes, or parafoils, are controllable in a manner seemingly similar to that of fixed wing aircraft. This maneuverability allows for a more flexible operational area and makes parafoils an attractive option for payload descent and recovery missions.

This research arose from an interest in improving the capabilities and effectiveness of the Atmospheric and Space Threshold Research Oklahoma (ASTRO) program at Oklahoma State University (OSU). The ASTRO program primarily functions as an inexpensive towing system to gather data from the edge of Earth's atmosphere, as well as an educational experience for new engineering students at OSU. Each mission consists of a helium-filled latex balloon lifting a payload, attached underneath by paracord, to an altitude of around 100,000 feet where the balloon bursts. A parachute then deploys and carries the payload to the ground. Previous research provided accurate predictions of the paths taken during the balloon's ascent and payload's descent, but without control many flights ended with the payload descending into remote wooded areas.

Research then focused on the possibility of a parafoil parachute descent vehicle that could steer the payload to a predetermined landing zone clear of trees or water. A program was developed to simulate an autopilot-guided system. The autopilot model was to serve as the foundation for implementation into a physical system to test and evaluate, which is where this research began. However, many issues arose when constructing and testing the powered paraglider test vehicles. One system appeared unbalanced and impossible to control. The other showed unusual responses while maneuvering with a loosely attached payload. It was determined that more study should go into the analysis and design of a paraglider vehicle before adapting it to high altitude guidance missions.

The project was set to accomplish specific goals through research, analysis, and testing. It should: establish the fundamentals of parafoil flight behavior and characteristics of their design; allow for an analysis of a system with loosely attached masses; determine configurations for longitudinal static stability; simulate the effects of design parameters on vehicle dynamics; and gather observations from physical system flight. In this way, future vehicles could be designed for use in research pertaining to the ASTRO program.

GOAL: Establish criteria and tools for designing reliable powered paraglider vehicles in terms of meaningful configuration parameters.

1.2. OBJECTIVES

1. Conduct a literature review of parafoil aerodynamic characteristics and performance, powered paraglider systems, and existing methods of modeling their dynamics.
2. Derive an analytical model of a powered paraglider system.
3. Construct a test vehicle using parameters given by the dynamic analysis.
4. Conduct test flights with the vehicle to capture flight behavior and performance data.
5. Revise the vehicle design based on post-flight analysis and observations.

6. Repeat experimental flight and design revision process until reliable, steady, and controllable flight is achieved.
7. Draw conclusions on important parameters for powered paraglider vehicles based on the analytical model and observed physical performance.

1.3. BACKGROUND

A variety of parachutes have been developed and produced throughout history with varying capabilities and performance. Among many types, parachutes are commonly classified as conventional, Rogallo, or parafoil chutes.

1.3.1. CONVENTIONAL PARACHUTES

Typical conventional parachutes include round, cruciform, annular, and ribbon and ring designs.

The key feature of conventional parachutes is their use of drag as the primary acting force, as well as the sole method of deceleration. They are primarily single-skin devices, consisting of one layer of material, which form their shape through triangular gores. Commonly round in shape, new conventional parachutes geometries and features have been designed to increase controllability, survivability during high speed descents, and decreased descent rates.

Given their long history, round parachutes tend to be the most iconic parachute geometry. Early models were susceptible to wind since they had little to no control authority to redirect themselves. Development has led to the use of asymmetrically cut slots cut in the canopy to improve glide range and controllability through the use of horizontal “drive,” or velocity [1].

According to research by Potvin et al., round parachutes can achieve glide ratios between 0.8 and 1. Two models were tested, with one achieving a glide ratio of 0.78 and the other 0.90-1.0 [2].

More popular recently are cruciform parachutes. Cruciform parachutes consist of a cross- or plus-shaped canopy, which, when folded over, forms a square parachute geometry. They are

more stable in vertical descents than round parachutes and low influence from gusts [1]. Dennis also claims an arm ratio of 4:1 is ideal for stability. Based on average descent rates for the T-10 round parachute and T-11 cruciform parachute from their manufacturers, the reduction in descent speed is about 18%, from 22 ft/s to 18 ft/s, respectively. This reduction in speed is also credited to increasing survivability of the payload due to the reduction in impact energy. Potvin's research found cruciform parachutes to have glide ratios from 0.5-0.9.

1.3.2. ROGALLO WINGS

A breakaway from the drag force decelerators is the Rogallo wing, developed by Francis and Gertrude Rogallo in 1948 [3]. Similar to the wings found on hang gliders, these fabric wings can be used as alternatives to parachutes for vehicles desiring increased glide range or moving at very high speeds. Lines are tied to a canopy to form a wing shape that typically consists of two conical portions positioned side-by-side pointing forward.

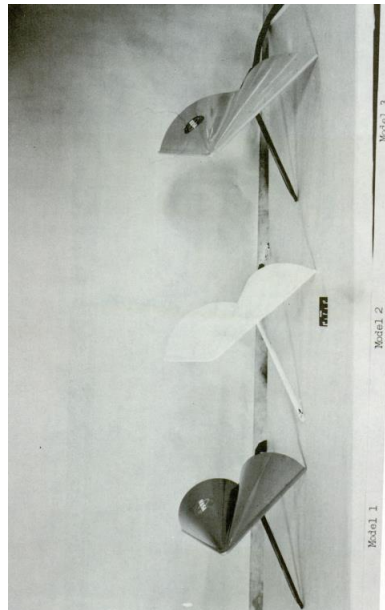


Figure 1: Rigid Rogallo Wings [4]

Beginning in 1957, Rogallo was allowed to experiment in a National Advisory Committee for Aeronautics (NACA) wind tunnel. Research has since been performed for both flexible and rigid wings at supersonic speeds [4]. A Rogallo wing design was considered for both the Apollo and Gemini space programs but was rejected in both cases. Although Rogallo wings did not develop into popular space recovery devices their research has been critical in the ultralight aviation field [3].

1.3.3. PARAFOLS

Parafoils are double skin parachutes with airfoil cross-sections, which allows them to generate lift like a conventional aircraft wing. With the primary force shifted from drag to lift, parafoils are capable of higher glide ratios than other decelerators, which can make them ideal for payload recovery missions. Parafoils are constructed by connecting two fabric skins, top and bottom, around airfoil-shaped fabric ribs that are placed chord-wise periodically along the length of the span. Each volume enclosed by the skins and ribs is known as a cell. Truncated on the leading edge, ram-air parafoils allow these cells to fill with incoming air and inflate the parachute. This, in combination with tension in the support lines maintain the desired wing shape.

Opale Paramodels is a designer and manufacturer of small radio controlled (RC) paraglider kits, including their own parafoils. They have produced classic models but recently the group has designed two novel styles. One is a single skin parafoil, which consists only of a top skin with ribbing to hold the airfoil shape. Almost resembling a kite or Rogallo wing more than a parafoil, Opale claims the single skin design provides easier inflation of the canopy and keeps the air mass contained under the top skin [5]. Despite lacking cells to inflate, the operation is similar to other ram-air parafoils. The wing catches air and pushes the skin up while support lines keep the desired airfoil shape. They also produce hybrid parafoils. These models are single skin designs with cells added underneath to further assist inflating the wing. Both designs are interesting new

approaches to inflatable wings but more research is required before they could be incorporated into any studies reliably.

1.3.4. PARAGLIDER APPLICATIONS

Acting as a hybrid between a packable decelerator and a controllable glider, paragliders have a wide array of potential applications. Typically, these involve missions too dangerous or costly for conventional manned aircraft. Proven to be capable observation platforms, as well as payload recovery and delivery vehicles, paragliders fill needs in many fields.

Although cancelled, the X-38 reentry vehicle was designed with a parafoil for slowing and guiding the vehicle to a landing site autonomously. A similar concept has been imagined for recovery of World View's Voyager program space capsule. The capsule is taken up to 100,000 ft via high-altitude balloon and then is guided back to a landing zone with a parafoil. The concept is very similar to that proposed for ASTRO program.

Generally found in military applications, paragliders are used for precise delivery of supplies and equipment. The United States Military Joint Precision Airdrop System (JPADS) utilizes parafoils with a sophisticated autopilot system for delivery of supplies to specified landing zones. STARA developed a small paraglider system for delivering blood or ammunition within 30 m of a landing point from 25,000 ft MSL [6].

Critical to the wellbeing of soldiers in the field, intelligence can make the difference between victory and defeat. The ability to survey the battlefield allows soldiers to identify and monitor enemy positions, improving survivability. Paraglider reconnaissance vehicles are able to deploy and loiter for long periods of time while feeding video and data to ground stations. Atair Aerospace has designed backpack-sized, as well as a Humvee and trailer hauled, paraglider systems capable of flight times greater than four and thirty-four hours, respectively.

Finally, paragliders, both manned and remoted controlled, are enjoyed by hobbyists for recreation. Full-scale powered paragliders, often referred to as paramotors, fill a gap between those who enjoy flying but do not want to earn a license. Under Federal Acquisition Regulation Part 103, for lightweight aircraft pilots need not have any license or medical qualification. Unpowered paragliders are often flown from high elevations such as cliffs or mountains. There are also sport kites that act as drag chutes, pulling buggies or snowboards without input from the operator.

CHAPTER 2

REVIEW OF LITERATURE

2.1. WIND TUNNEL TESTS

2.1.1. NICOLAIDES

In order to ensure the model behaves aerodynamically correct as a parafoil, experimental performance data was desired. Nicolaides conducted wind tunnel tests starting in 1964 on various parafoil configurations. Each model varied in terms of aspect ratio, planform area, and rigidity, but the airfoil shape remained generally unchanged. The camber and air intake cut differ but each section consists of a curved top surface with a flat bottom and pennants, to which the lines connect.

The following lift and drag graphs are taken from another document by Nicolaides & Tragarz during flight testing of the parafoil, but they reflect data taken during the wind tunnel tests from his first paper. The advantage of the flight test document is his inclusion of the higher angle of attack data points, as well as the tabulated data for aspect ratio wings between 1.0 and 3.0. The coordinates for the 3.0 aspect ratio wing can be found in Appendix A of this paper.

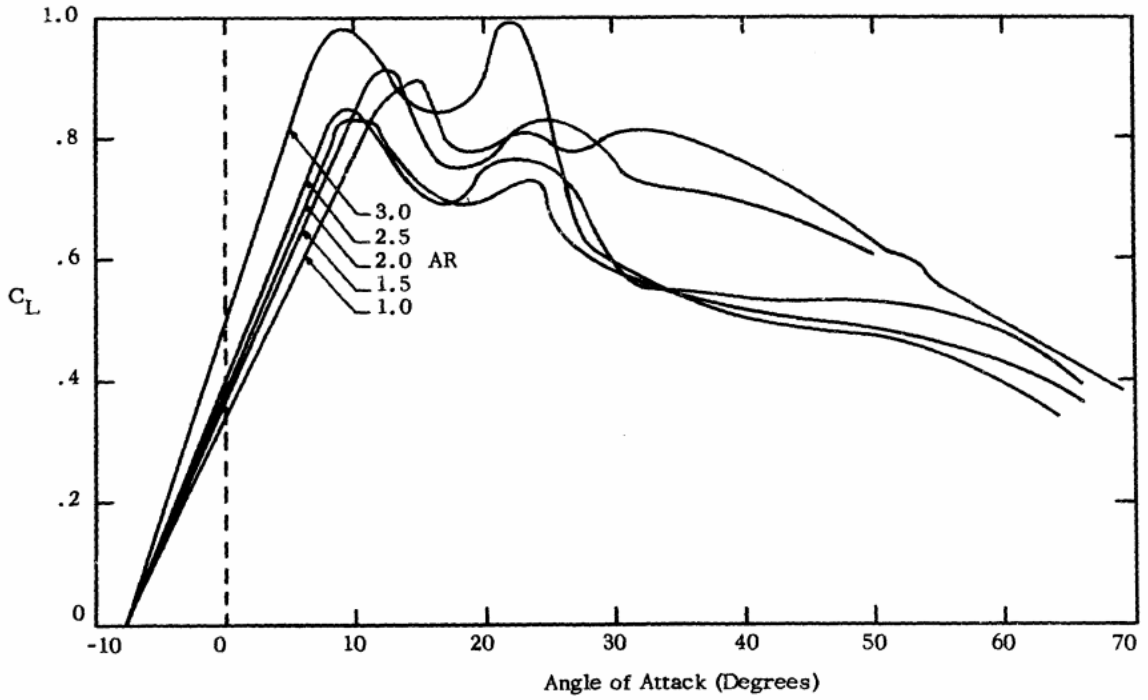


Figure 2: Lift Curve from Nicolaidis Experiments [8]

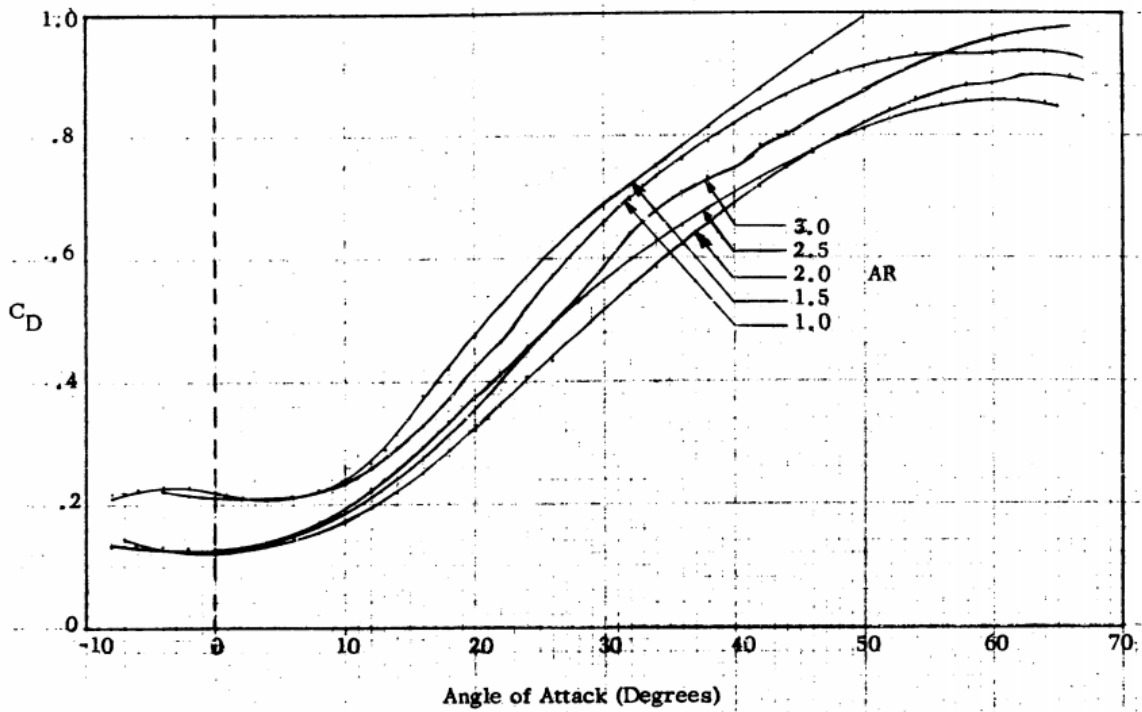


Figure 3: Drag Curve from Nicolaidis Experiments [8]

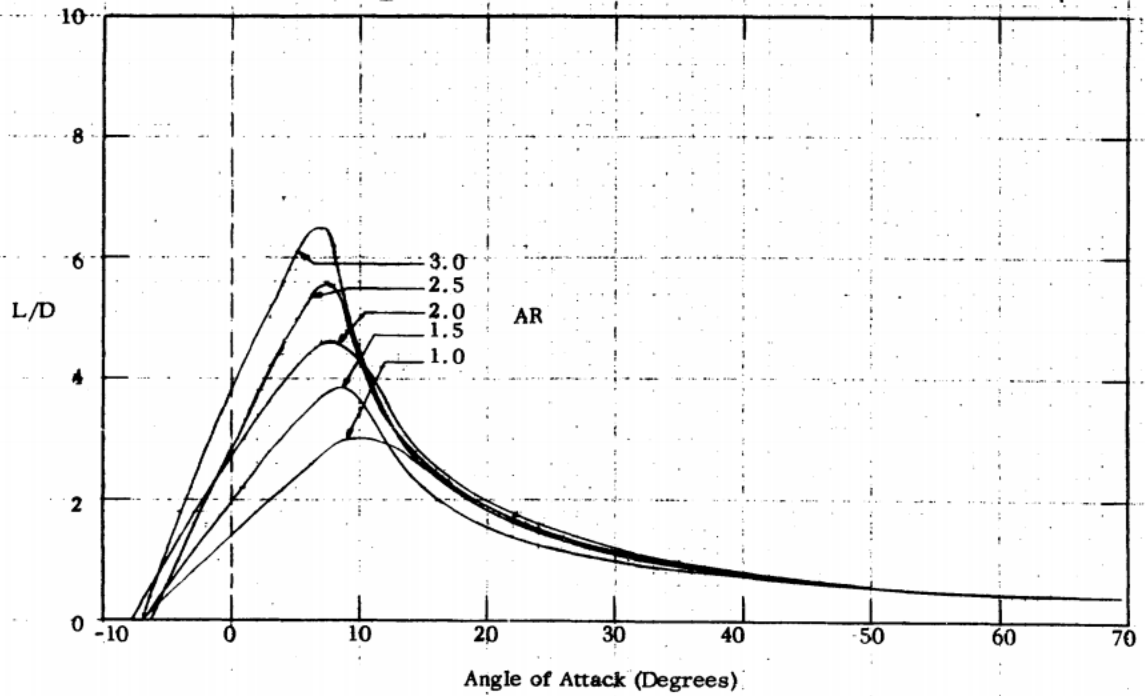


Figure 4: Lift to Drag Plot from Nicolaidis Experiments [8]

2.1.2. FURFARO ET AL.

Furfaro et al. experimented with parafoil wing sections in a wind tunnel in order to create a wider range of test data for CFD validation. Their study focused on analyzing the effects of leading edge truncation, ram-air inlets, and spanwise scalloping by measuring force and moment data. Additionally, flow visualization was performed. Each test model consisted of an airfoil section, taken from an RC parafoil, that was then altered to match a desired test condition. The geometry is similar to the flat bottomed parafoils tested by Nicolaidis and can be found in Appendix A. The table below gives the specifications of each wing according to the name given by Furfaro.

Model Name	Description
Round L.E.	Considered a baseline airfoil, with the leading edge truncation rounded
Open L.E.	Truncated leading edge with 18 ram-air cells
Open L.E.	Truncated leading edge but with closed ram-air inlets
Wavy	Truncated leading edge, closed ram-air inlets, and added spanwise scalloping

Table 1: Furfaro Test Wing Sections

The models were constructed from Styrofoam, coated in balsa wood, and reinforced with fiberglass and epoxy. As a consequence, this wind tunnel test provides an analysis of a rigid parafoil wings, which provides excellent validation data for research into CFD; however, its accuracy in modeling realistic flight performance is of some question. The characteristics of flexible parafoils will be discussed in the next section.

Figures Figure 5 and Figure 6 show the resulting lift and drag coefficients, respectively, as a function of angle of attack. The drag polar is given by Figure 7. For convenience the lift to drag ratio curve has been calculated and can be seen in Figure 9. Furfaro et al. found that about 10 degrees angle of attack the flow around the rounded leading edge model would begin to separate. With increasing the free stream velocity not an option, they chose to place a turbulator (sand paper strip) near the leading edge. The difference in performance can be seen by Figure 8. Data in Figure 7 reflects tests performed with the turbulator.

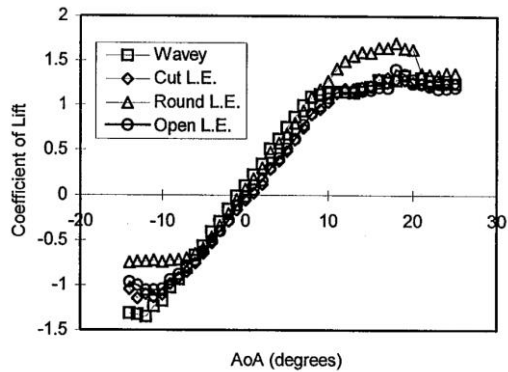


Figure 5: Lift Curve from Furfaro Experiments [9]

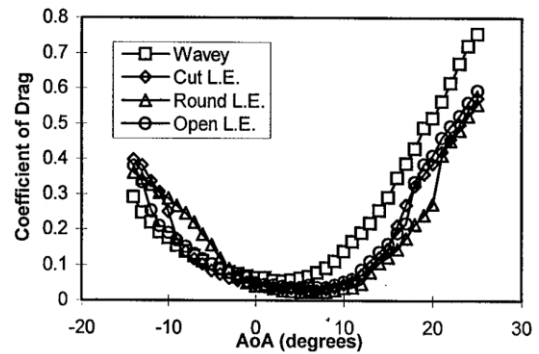


Figure 6: Drag Curve from Furfaro Experiments [9]

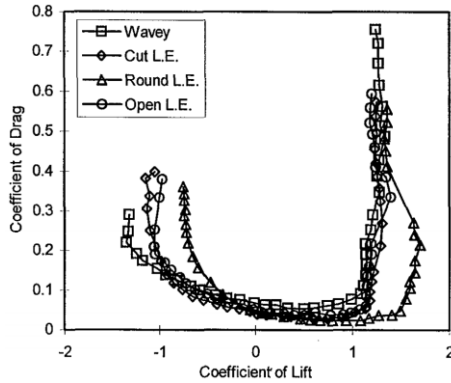


Figure 7: Drag Polar from Furfaro Experiments [9]

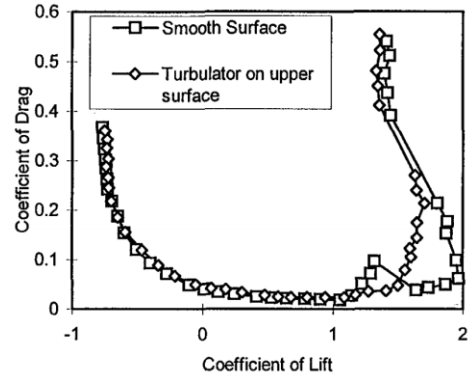


Figure 8: Turbulator Effect on Drag Polar [9]

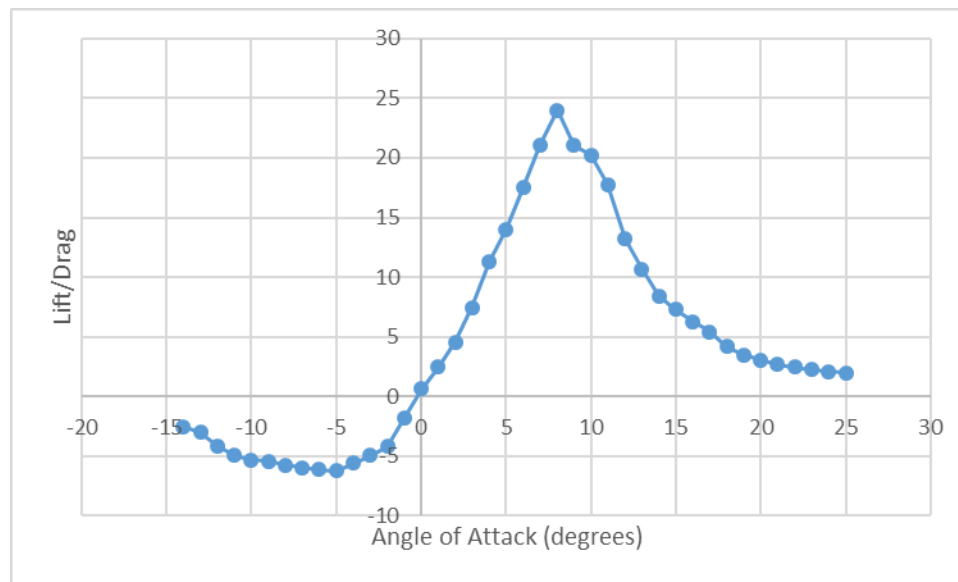


Figure 9: Lift to Drag Ratio vs. Alpha from Furfaro Data [9]

Apart from providing performance data for a rigid parafoil, this research presents a few key characteristics of airflow around parafoils. Compared to the baseline smooth airfoil, the models with truncated noses possess less section lift. Additionally, the truncated nose causes separation, at 10 degrees angle of attack in this case, which results in lift leveling out. However, the closed air intake model performs in relatively the same manner as the model with them open. Scalloping produced increased drag, but lift was relatively unchanged. The results are of limited use in realistic modeling, due to rigidity of the system; however, in terms of CFD analyses these findings provide another source of validation, since rigidity is often an assumption it must make

as well. Perhaps the results being independent of the air intake being open or closed will provide faster or simpler solutions.

2.1.3. UDDIN & MASHUD

By design, parafoils are supposed to keep a wing shape based on their airfoil-ribbed cross-section; however, after inflating, the form achieved is certainly not the exact shape intended. The lack of structure is a beneficial feature of a parafoil but it has its cost in uncertain performance. Uddin & Mashud investigated the effects of a flexible parafoil wing skin in terms of inflation, internal pressure, and external pressure distributions in their wind tunnel experiments. Each experiment consists of a flexible parafoil spanning the width of the wind tunnel, reducing three-dimensional effects, and allows for an analysis of the flow based on cross-section alone.

Figure 10 shows the developed shape of the wing based on its orientation. Under very low angle of attack conditions the parafoil was found to be unable to inflate fully, primarily at the nose of the section. The uninflated portion is focused around the leading edge, which results in a reduced air intake area. However, when the parafoil advances to a small angle of attack of 2° full inflation is seen to take place but the rear expands past its intended shape. At angles higher than 8° the shape is relatively constant. At this point the internal pressure of the parafoil is seen to converge in Figure 11 and could be considered its fully inflated state.

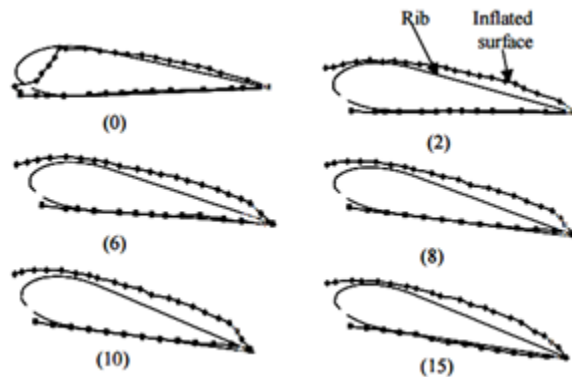


Figure 10: Inflated Parafoil at Various Angles of Attack [10]

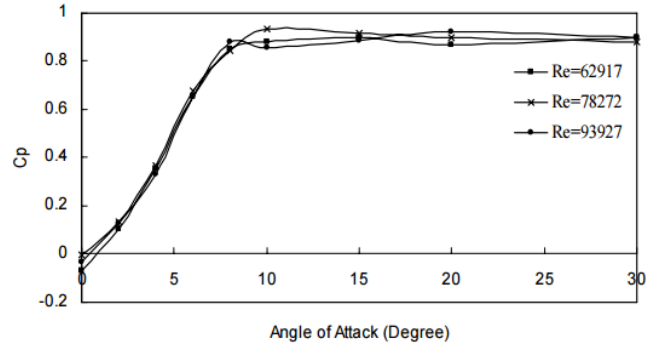


Figure 11: Parafoil Variation of Internal Pressure with Angle of Attack [10]

Perhaps the largest effect of the flexible shape is the change in external pressure distribution, which affects the aerodynamic performance of the wing section. Seen by Figure 86 in Appendix A, the pressure distribution is fairly constant throughout the various angles of attack with a few exceptions. At zero angle of attack the leading edge is under developed and adversely affects the flow over the wing. Between six and ten degrees the pressure distribution appears normal, with eight degrees appearing to produce maximum lift. At higher angles of attack of 15° and 20° the flow begins to separate around the 80% chord point, while at 30 degrees almost the entire flow has separated.

The change in actual inflated section versus the designed section stresses the need to reliable performance data estimates. Whether this be through wind tunnel testing or computer simulation, a simple airfoil analysis will not provide very accurate data for system modeling.

2.2. AERODYNAMIC COEFFICIENTS

More traditional to conventional aircraft dynamics, aerodynamic coefficients and derivatives can be determined to describe its behavior in a 6 degree of freedom (DoF) model. Jann aimed to find the same for a parafoil wing with arc anhedral through the use of extended lifting line theory. This approach is common with airplane wings and was also adapted by Gonzalez and Iosilevskii to parafoil wings [12, 13]. Jann derives his equations in terms of a rigid elliptically shaped wing with arc anhedral to provide a more robust method for calculating coefficients for a specific wing

form. However, like other similar models, his calculations neglect wing flexibility by assuming a rigid wing, and as such are advised to be understood as estimates rather than a complete solution. He reduces the complexity of his model by neglecting the influence of the fins, flow separation, and apparent mass effects.

To validate his solution, Jann compares his calculated results to coefficients derived from vortex lattice analysis and test flight data. He explains the opposite signs of the C_{np} , C_{Yr} , and C_{lr} coefficients in the vortex lattice comparison is likely the result of assumptions made for the position of the center of pressure. The relative magnitudes and signs of the coefficients proves a general plausibility in the accuracy of the equations. The coefficients calculated through the lifting line and vortex lattice methods can be found in Appendix A.

After plugging his coefficients into a 6-DoF model, he was able to compare simulated performance to flight data from the Autonomous Parafoil Landing Experiment (ALEX). Extracted values varied between flights due to the information available in the data but results were consistent enough to provide a plausible accuracy to the expected values. The simulated motion, with the calculated coefficients, can be seen overlaid onto flight data in Figure 12. The results generally match, but through the use of correction factors on $C_{Y\delta\alpha}$, C_{lp} , and C_{nr} the motion was even closer, as seen in Figure 13.

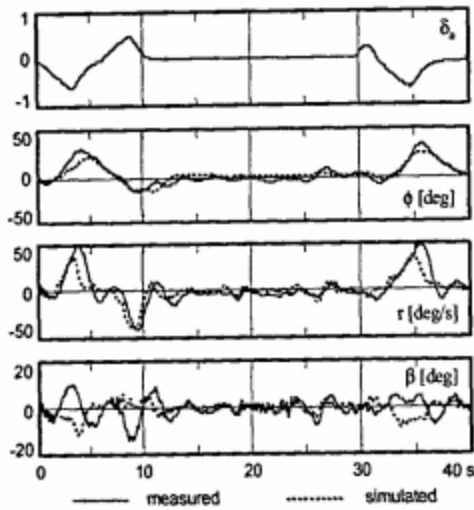


Figure 12: Comparison of Flight Data to Calculated Coefficients [11]

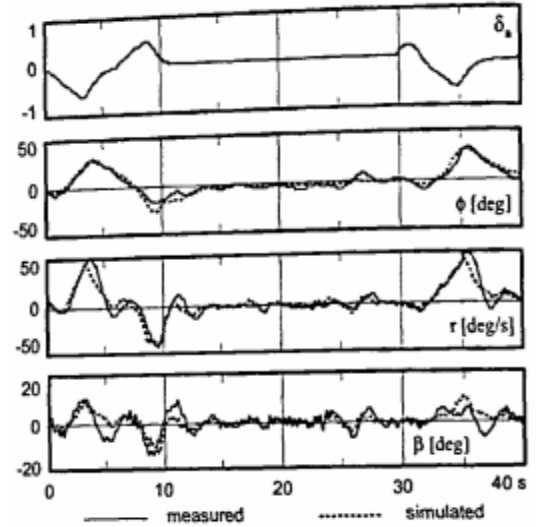


Figure 13: Comparison of Flight Data to Calculated Coefficients with Correction Factor [11]

2.3. COMPUTATIONAL FLUID DYNAMICS

In an attempt to provide an inexpensive method for extracting parafoil performance information, research has been done to accurately model parafoil parachutes in computational fluid dynamics (CFD). Using the CFD analysis of solving the Navier-Stokes equation with the finite volume method, Cao simulated various geometric models of parafoil wings and compared them to previous tests performed by Nicolaidis. There are some assumptions required due to the limitations of the CFD method:

- The simulation model will remain completely rigid and cannot allow for deformation caused by inflation or aerodynamic loading.
- All surfaces of the wing are considered impermeable.
- Lines are not considered in the simulation.

Cao states that these assumptions are necessary to reduce the complexity of the model in order to lessen the cost of computing, while maintaining accuracy in the results. The results for his tests, shown by Figure 14 and Figure 15, show very similar results when compared to Nicolaidis' wind tunnel tests. Cao notes that the difference in stall angle of attack was most likely due to the CFD model being rigid while the "NASA model" was flexible. Furthermore, his results generally match the trend of the two "ND model" wind tunnel parafoils, which were also rigid. While the numbers may not line up exactly, CFD appears to be a valid method for estimating the general trend of a parafoil wing when it is not feasible to experimentally evaluate performance.

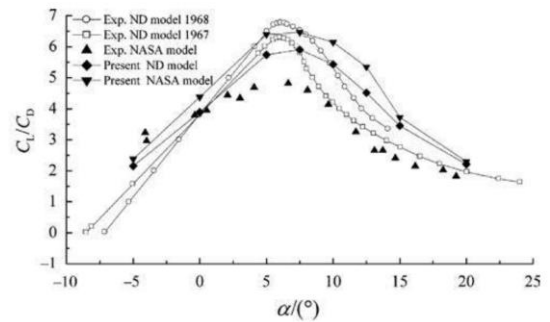
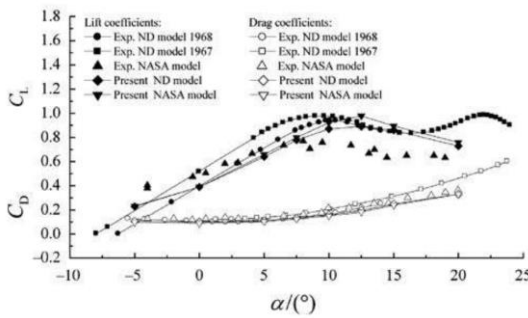


Figure 14: Lift and Drag Curves from CFD Analysis [14] Figure 15: Lift to Drag Ratio from CFD Analysis [14]

From the CFD results, Cao developed some relations and findings between parafoil geometry and flight performance. Some of the findings include:

- The leading edge cut for intake air increases drag while decreasing stall angle. Its influence on the flow is limited to the leading edge portion of the wing.
- Parafoils with less drag tend to have better gliding performance.
- Airfoil shape is the primary factor in lift to drag ratio achieved. Profile drag can be reduced by designing a wing with smaller thickness and leading edge radius.

The effect of airfoil shape can be seen in Figure 16 and Figure 17 as well as the effect of the leading edge cut in Figure 18 and Figure 19. The two airfoils used in Figure 16 and Figure 17 are the parafoil used by Nicolaidis in his NASA wind tunnel tests, labeled "NASA model," and the

LS(1)-0417 airfoil used by modern paragliders, labeled “model 7.” Cao estimates the lower lift coefficient is due to the 2% smaller thickness of the LS(1)-0417 compared to the NASA model.

Figure 18 and Figure 19 show the comparative performance between the parafoil wing with the air inlets open, model 7, and the same LS(1)-0417 wing with no air inlet cut, model 8.

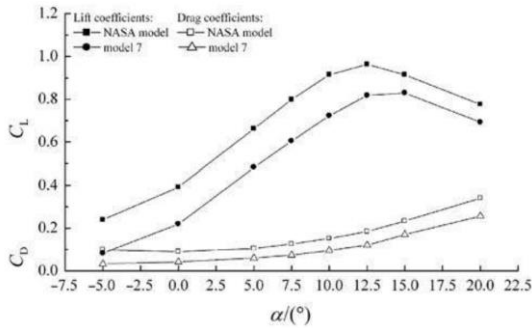


Figure 16: Lift and Drag Curves for CFD Analysis Between Differing Airfoil Shapes [14]

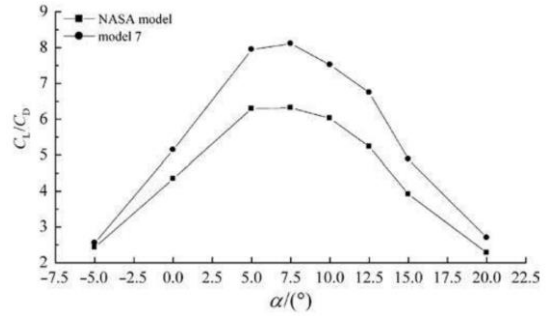


Figure 17: Lift to Drag Ratio for CFD Analysis Between Differing Airfoil Shapes [14]

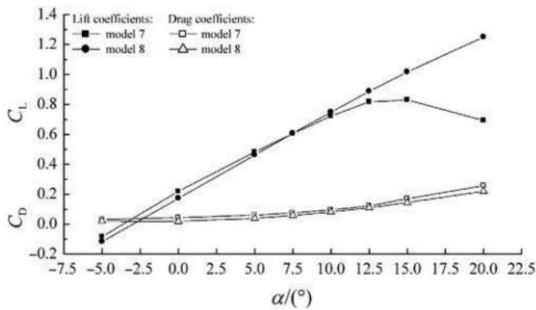


Figure 18: Lift and Drag Curves for CFD Analysis With and Without Leading Edge Cut [14]

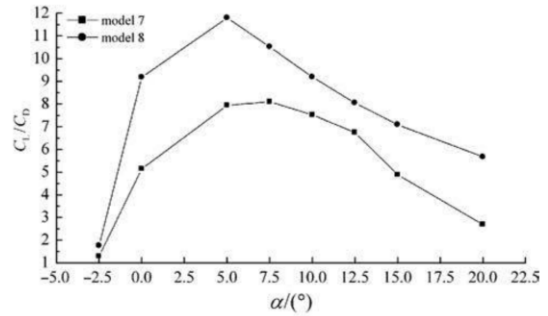


Figure 19: Lift to Drag Ratio for CFD Analysis With and Without Leading Edge Cut [14]

2.4. “APPARENT MASS”

A body travelling through a fluid induces movement of the fluid around it. This movement imparts pressure forces on the body, known as “apparent mass” pressures, and they are a result of additional fluid momentum and energy from the fluid volume influenced by the body. This theoretical fluid volume mass is called the “apparent mass” and from the work of Lissaman can be estimated for each motion axis' direction and rotation, in the form of a mass or moment,

respectively. Lissaman claims the estimates provide "useful accuracy." There are differing views on the appropriateness of this theoretical mass method.

“Apparent mass” effects are especially prevalent in lightly-loaded vehicles, such as paragliders, where a relatively large amount of air is affected by the light parafoil. In larger conventional aircraft the ratio between vehicle mass and fluid mass is typically small and the effects less significant. Lissaman suggests the effects are most prevalent in vehicles with a wing loading of less than around 1 psf. The effect is also exacerbated with a parachute configuration where the lifting surface is located a considerable distance away from the comparatively large body mass. The aerodynamic forces then act at the apparent mass centroid, which is displaced from the parachute center of mass. In order to reduce the complexity of the model, the system proposed by this research will consider the center of gravity of the wing to be at the quarter-chord position, where the aerodynamic forces will also be assumed to act. Without an accurate way of calculating the location of the apparent center of mass the effects would be equally unreliable in that case.

This research will only be interested in the translation of the parafoil in the xz-plane, following the standard aircraft axes. The terms used are surge, forward and backward movement, and plunge, climbing and sinking movement. These are the A and C components seen in Figure 20. Lissaman provides estimate for these terms in the form of the equations 2.1 and 2.2.

$$A = 0.666\rho t^2 b \quad (2.1)$$

$$C = 0.785\rho b c^2 \frac{AR}{1+AR} \quad (2.2)$$

where t is the thickness of the wing, b is the span, c is the chord, ρ is air density, and AR is the wing aspect ratio. Note, in his equations the density term is not listed and must be added to extract the mass value.

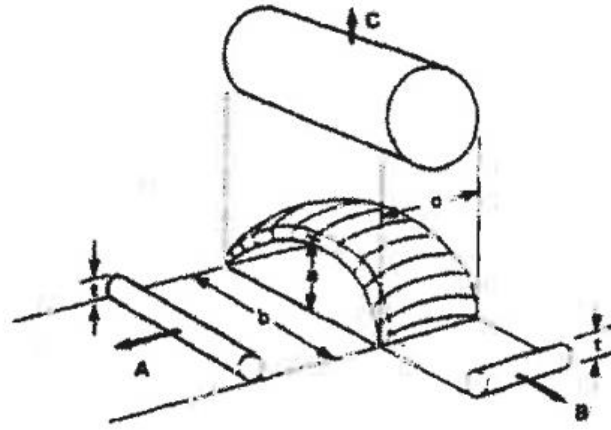


Figure 20: Apparent Mass Components and Related Variables [15]

Additionally, he offers equations that account for the arc ratio as well. The arc ratio is measured when the span reaches its effective length and is the comparison of the parafoil height to its span. Lissaman uses an approximate value of 0.15 in his calculations. The equations are as follows,

$$A = 0.666\rho \left(1 + \frac{8}{3}a^{*2}\right) t^2 b \quad (2.3)$$

$$C = 0.785\rho \sqrt{1 + 2a^{*2}(1 - t^2)} \frac{AR}{1+AR} bc^2 \quad (2.4)$$

However, with the exact arc ratio unknown, the assumed 0.15 value by Lissaman will be kept, and the analysis will use equations 2.1 and 2.2. The implementation of these equations will be covered in section 4.4.

2.5. GLIDE ANGLE

When designing a parafoil descent vehicle, important specifications for design could include descent angle and velocity. With paragliding vehicles, it can be seen that these can be controlled through the adjustment of two variables, rigging angle and wing loading; although, there is a complex relationship between rigging angle and the aerodynamic performance of the parafoil. Take the simple unpowered paraglider system shown in Figure 21. Originally proposed by

Connor, it consists of a parafoil, whose mass has been neglected, with a suspended payload, all descending at a flight path angle, γ . However, unlike Conner's model, this one will also include the payload drag. Also note, the coordinate and angle convention may not be that of traditional aircraft analysis, but will correlate to work featured in the rest of this study.

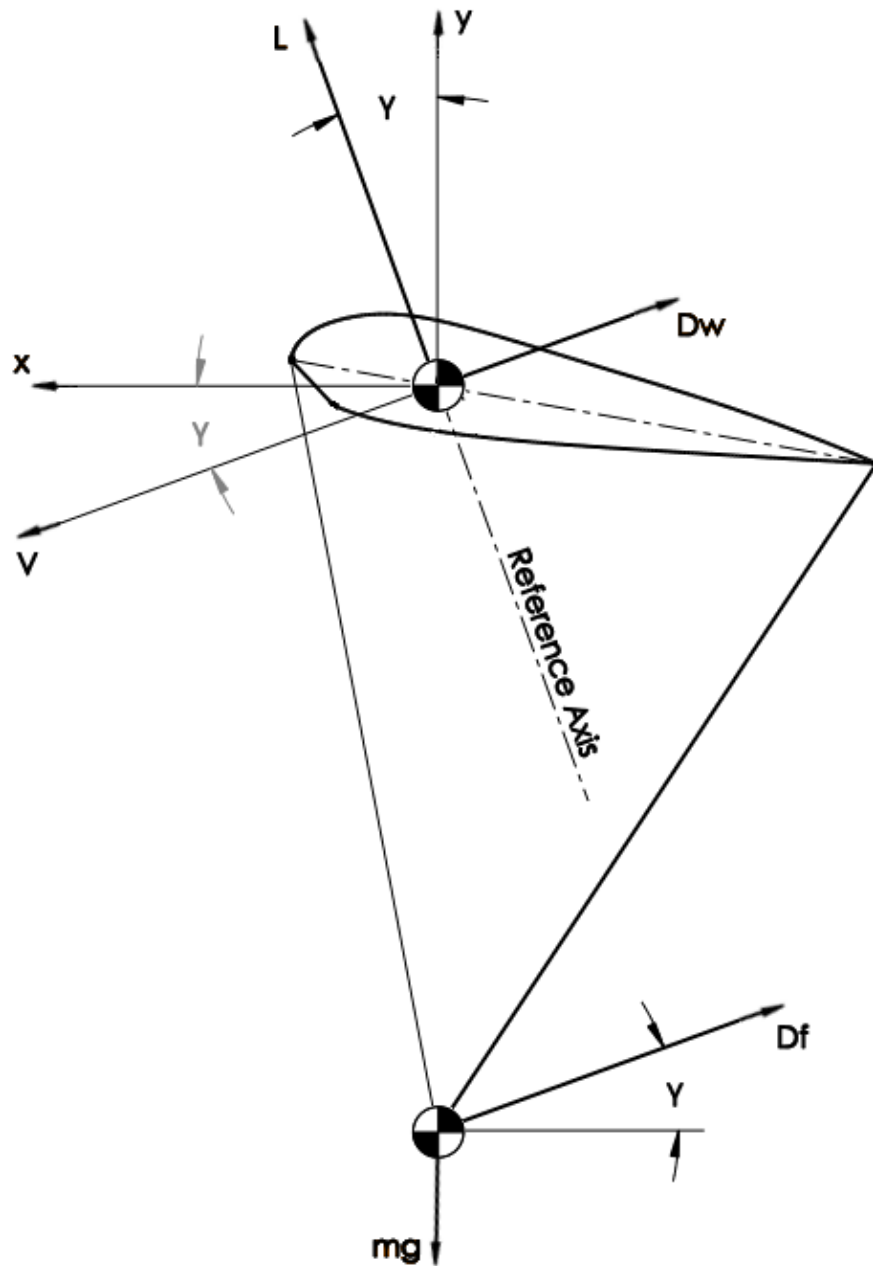


Figure 21: Simple Paraglider Model

By summing the forces along each axis the system becomes,

$$ma_x = L \sin \gamma - D_w \cos \gamma - D_f \cos \gamma \quad (2.5)$$

$$ma_y = L \cos \gamma + D_w \sin \gamma + D_f \sin \gamma - mg \quad (2.6)$$

where, m is the mass of the entire system, L is the lift, D_w is the drag produced by the wing, and D_f is the drag generated by the payload. At equilibrium the system will have zero net acceleration and is shown by setting the left side of the equations above to zero.

Using the equation for forces in the x -direction, γ can be found to be

$$\gamma = \tan^{-1} \left(\frac{D_w + D_f}{L} \right) \quad (2.7)$$

Therefore, for steady state conditions the flight path will be governed by the total lift to drag ratio for the vehicle.

Additionally, for payload recovery the velocity at impact can be crucial to mission success.

Similar to the method of finding the flight path, the descent velocity can be found by using the system's force information. Instead of using the x - or y -coordinate, the forces can be summed along the reference axis shown in Figure 21. This axis is situated along the lifting line and therefore is rotated from the vertical axis by the angle γ . Because the drag forces are perpendicular to the lifting line, the only forces included are the lift and system weight. At steady state, the equation becomes,

$$L - mg \cos \gamma = 0 \quad (2.8)$$

where the lift is equivalent to,

$$L = \frac{1}{2} \rho v^2 S C_L \quad (2.9)$$

Substituting into the force equation the descent velocity can be solved for as,

$$v = \sqrt{\frac{2 \cos \gamma mg}{\rho C_L S}} \quad (2.10)$$

It can be seen the velocity is then a function of flight path angle and wing loading. Flight path angle is controllable through the rigging angle of the parafoil, or rather the lift to drag ratio, which is a product of the rigging angle.

2.6. PARAGLIDER STEERING

Paragliders are usually constructed with one of two ways to control the direction. The first uses adjustable trailing edge support lines that can be pulled during flight. If both left and right rear support lines are shortened it will cause an increase in lift and the paraglider will flare, which can be useful during landings. When only one side is pulled it causes an increase in drag on one side, to the point of dominating lift, and results in a “skid” turn in the direction of the pulled line [17]. In this way the lowered trailing edge acts as a brake and is called skid steering. The second method ties all of the support lines to either side of a rod called a fly-bar. When the fly-bar is rotated one side of the parafoil is pulled down while the other is allowed to rise. This causes a rotation of the lift vector and turns the paraglider in a similar manner to conventional aircraft [18]. This is referred to as roll steering.

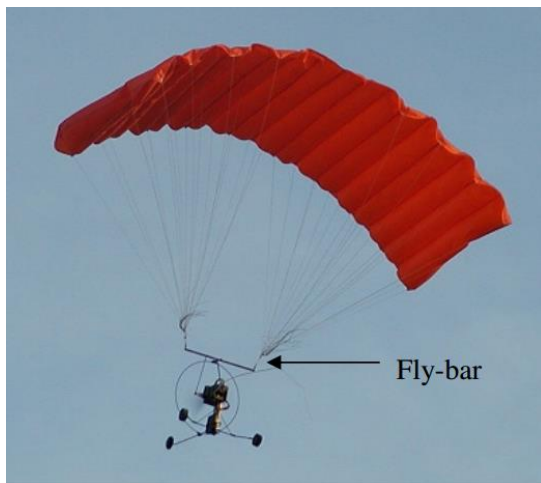


Figure 22: Paraglider with Fly-bar [18]



Figure 23: Paraglider with Steering Line [18]

Although most paragliders use skid turning for directional control, many that use brakes for steering have the potential to produce roll turns. When a brake is pulled it will first act as an aileron until drag overcomes the additional lift generated. Additionally, while the paraglider is producing a roll turn it is actually in the opposite direction than intended. In Figure 24 from Slegers and Costello, the control reversal can be seen by the parafoil generating a negative turn rate until skid steering is achieved at 15° brake angle.

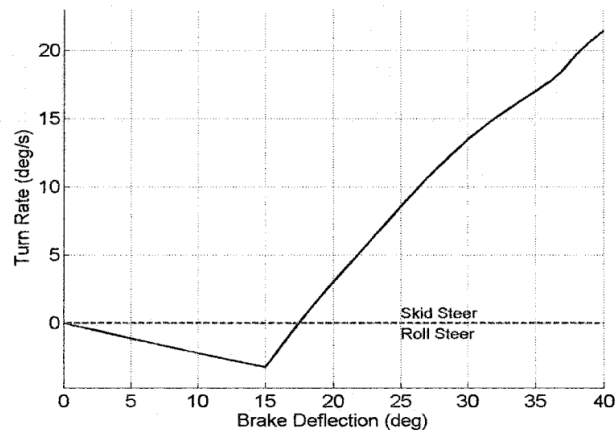


Figure 24: Turn Rate and Direction with Brake Deflection [17]

2.6. THROTTLE ONLY CONTROL

Although typically only ever used in emergency scenarios, conventional aircraft are able to maneuver solely through controlling the aircraft's thrust. By utilizing differential thrust an aircraft can generate yaw motion and provide directional control; however, this also can be employed to induce rolling motion. Through dihedral effect, if a sideslip is generated the aircraft will possess different angles of attack on each wing and produce a roll. Burcham researched throttle only control on the F-15 and described how pitch control is possible through a few methods. If thrust is applied to a speed stable aircraft it will result in a temporary increase in speed, which causes additional lift and positive climb. If the thrust line is vertically offset from the center of gravity it will inherently produce a pitching moment when active. Lastly, if the

thrust line is inclined to produce a vertical component then additional thrust creates a higher rate of climb and flightpath angle.

Lacking a conventional tail and associated control surfaces, paraglider maneuvering is limited to throttle and airbrake use only. With only a single engine, most paragliders are limited to thrust primarily producing changes in pitch, rather than directional or roll control. However, some inherent characteristics of paragliders enable greater control authority than in conventional aircraft. With the fuselage and thrust hanging a significant distance away from the wing, thrust has a large moment arm to affect the system as a whole.

Paragliders capable of differential brake line control offer another technique for controlling pitch. If both brakes are pulled simultaneously the resulting action is similar to that of a conventional aircraft flare. By reducing the trailing edge line, the rigging angle of the parafoil is increased and a higher angle of attack is generated, producing greater lift and climb.

2.8. DYNAMIC MODELS

Many attempts have been made to model parafoil-payload systems through a variety of methods. Each approach has its own assumptions, accuracy, and complexity. This section will discuss previously developed models and how they relate to this paper's research.

Early models analyzed the system in terms similar to that used for conventional aircraft, with six degrees of freedom. This describes the vehicle in three translational directions and three rotational directions. However, with conventional aircraft the single body is relatively rigid and can adequately be described as one body. To adapt that same method to the parafoil-payload system an assumption must be made, which states that the two shall act together as one rigid body with a common center of mass to act about. Primarily, this has been used for two-dimensional analyses, with debate over the accuracy of such models. Notable uses for this method are

Goodrick's longitudinal stability study, referenced by Yakimenko, and Chambers' longitudinal dynamics and control research [18, 20].

Further development was focused around allowing each body to move freely but within realistic constraints. Fallon modeled his three body parachute-riser-payload system with 6-DoF each, but reduced the total degrees of freedom to 15 due to riser constraints [20]. By neglecting axisymmetric roll, Wolf developed a 10-DoF model for a coupled axisymmetric wing and payload system [20]. More recently, the predominate methods for modeling paraglider dynamics are 9- or 8-DoF models. Watanabe and Ochi used six degrees of freedom for full parafoil motion and two to allow the payload to rotate in the pitch and yaw direction. Additionally, the yaw rotation was modeled as a spring and damper system. Slegers and Costello developed a 9-DoF system with three Euler angles to describe the orientation of the parafoil and payload and three components for the inertial position of the joint between them. Like Watanabe and Ochi, rotational stiffness was added to simulate twist resistance.

2.8.1. QUISENBERRY

Quisenberry developed a model for a cable-towed aircraft utilizing Lagrange's equation to simulate cable dynamics. By forming the cable from a connected series of small masses with small arm lengths the cable resembles an n-tuple pendulum with n masses and arms. With sufficiently small line lengths the series behaves and appears as a flexible cable. Although not all systems require as many segments, his method enables use of the Lagrange equation in applications where even a few additional masses would otherwise drastically increase the difficulty of analysis.

2.8.2. CHAMBERS

In 2007, Chambers researched longitudinal dynamic modeling and control of powered parachute aircraft. His study focused on a rigid system with a combined center of gravity for the wing and

fuselage; however, he also briefly explored the possibility of using Lagrange's method to model the system with a hinged connection point between the parafoil and fuselage. He felt the rigid system would still provide adequate steady-state results, so his work is based primarily on that system. His model also had an assumption of a constant angle of attack. Chambers explains that as parafoil wings move in the wind the line tensions will quickly equalize and return to equilibrium. As a result, lift and drag coefficients are constant and lift and drag are only a function of velocity. This causes unrealistic results when the aircraft experiences large disturbances, such as a rapid increase in thrust.

The methodology differs from that of the research performed in this paper. The paraglider was flown first while taking flight behavior measurements. Thrust and drag were then measured in a wind tunnel based on the airspeed of the test vehicle during level steady flight. With the fuselage forces, thrust and drag, measured and combined with the constant angle of attack assumption, a relation was then drawn for lift and drag factors for the wing based on force balancing in the traditional lift equation. In other words, during steady flight the paraglider's weight is countered equally by its generated lift and the resulting drag is countered by generated thrust as to result in zero total acceleration of the system. The factor for lift is formulated by the force balance equations below.

$$L = W \tag{2.11}$$

Where L is the lift of the parafoil and W is the weight of the entire system, and they are considered to be equivalent.

$$L = \frac{1}{2} \rho v^2 S C_L = K_L v^2 \tag{2.12}$$

where ρ is air density, S is the planform area, and C_L is the lift coefficient. These are all considered to be constant and combine into the lift factor, K_L , which is then multiplied by the velocity, v , squared.

$$W = K_L v^2 \quad (2.13)$$

Using the airspeed found for steady flight, the equation can then be solved for K_L and used to calculate lift when substituted back into equation 2.12, which is then only dependent on velocity.

The drag of the fuselage was determined through wind tunnel testing and applying a trend line to the data, resulting in a function for drag based on airspeed alone. Fuselage drag could be found for steady flight by applying the steady flight velocity to the equation. Since the thrust during steady flight is also known, based on wind tunnel testing as well, a force balancing technique is able to find the drag generated by the parafoil and its lines. This is similar to the lift and weight balancing process but instead relates thrust and drag, shown by the following equation.

$$T = D_f + D_w \quad (2.14)$$

where T is the produced thrust, D_f is the fuselage drag, and D_w is the parafoil wing drag.

However, an equation for parafoil drag that can be determined for any flight speed needs to be established for an effective analysis. By finding the lift to drag ratio of the parafoil, which will be constant due to the assumption that angle of attack is, and therefore lift and drag coefficients are also, constant. Using the parafoil lift that was determined in equation 2.12, the drag will then have its own factor, based off the lift factor, that can then be utilized with airspeed to determine the drag generated by flight for any given condition. Determining the drag can be seen with the following equations.

$$\frac{L}{D}(v_s) = \frac{L(v_s)}{T(v_s) - D_f(v_s)} \quad (2.15)$$

$$D_w = \frac{K_L v^2}{L/D(v_s)} = K_D v^2 \quad (2.16)$$

where v_s is the velocity for steady flight, and $L(v_s)$, $T(v_s)$, $D_f(v_s)$, and $L/D(v_s)$ are functions evaluated at the steady flight velocity. With K_L previously calculated and constant, the drag factor, K_D , is evaluated by comparing K_L to L/D , which is also constant based on assumptions. Simply, K_D is quotient of lift factor and the lift to drag ratio.

Chambers' system has several assumptions and simplifications; however, it has been shown to provide a close representation to expected motion for a paraglider. As such, it will provide a similar and useful model for comparison, especially since he proposed a 4-DoF approach as future research. The validation process with his methodology and data is shown in section 4.6.

2.9. LAGRANGE EQUATION

Previous models treat system of bodies as one collective point mass, which may accurately model the system, but for increased accuracy or more complex systems the Lagrangian Equation method works very well. This will be shown to be especially true for cases with multiple constrained masses.

In the basic form of classical mechanics, Newton's laws of motion are applied directly upon a system. Where when given the forces acting on the system or the motion of particles within the system the resulting forces or motion can be found. However, there are limitations to the practicality of this method when applied to more complicated systems. Greenwood specifically notes difficulty due to the vectorial nature of the equations of motion as well as accurately determining accelerations and forces, especially those that constrain particle motion. The Lagrangian approach presents a simpler method of deriving the equations of motion for complicated systems through the use of energy, generalized coordinates, and virtual work.

This section is mainly a brief paraphrasing of work from Greenwood's text. For a full explanation, his textbook is a very useful reference [23].

A system can be defined with any number of coordinates; however, there will generally exist a need to define constraint equations to describe the behavior of the system. The degrees of freedom of the system is then the number of coordinates, n , less the number of constraints required to relate the coordinates, m , or $(n - m)$ degrees of freedom. It is important to note that the degrees of freedom of a system is independent of the number of coordinates; rather, it is a fixed characteristic of the system.

Quisenberry demonstrates this concept with the use of a two-dimensional pendulum system, with a mass attached to a rigid bar of length R . This is shown by Figure 25. The system could be easily described using x - and y -coordinates to define the location of the mass. The mass would follow a circular path around the pivot point, which is equal to

$$x^2 + y^2 = R^2 \quad (2.17)$$

assuming the pivot point is located at the origin. This is an equation of constraint for the system. Therefore, with two coordinates used to describe the system and one constraint used to define its behavior, the degrees of freedom of the system is one.

Another way to visualize degrees of freedom is to control one coordinate. With a fixed x -location there can only exist one possible y -position, assuming no negative values, which is found through the constraint equation. With one coordinate fixed the system obtains only one state; therefore, it is only allowed one degree of freedom.

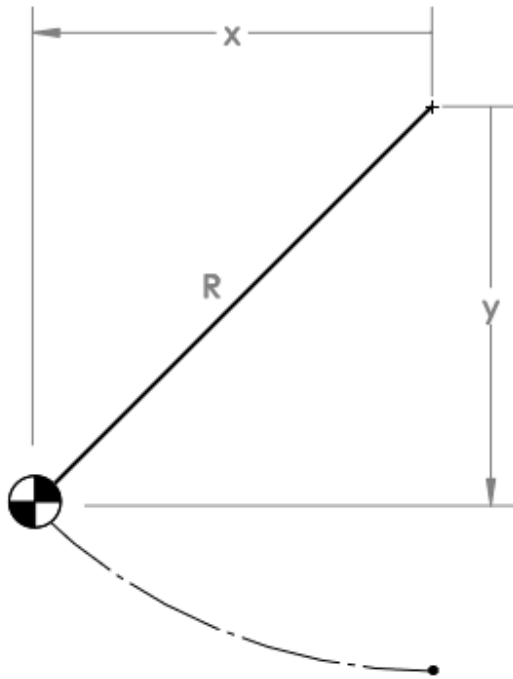


Figure 25: Simple Pendulum in Cartesian Coordinates

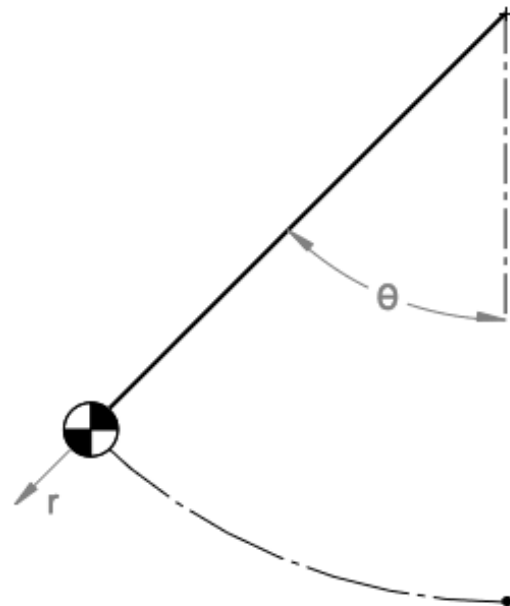


Figure 26: Simple Pendulum in Polar Coordinates

Instead of Cartesian coordinates, polar coordinates could have been used instead. The position of the mass could then be defined with r and θ . However, since r is known to be equal to the length of the bar, R , only θ is necessary to define the location of the mass. As a result, the system only has one degree of freedom, but no constraint equations. This is an advantage of choosing coordinates in the Lagrangian approach that will be discussed in section 4.2.

There can exist any amount of coordinates to fully specify a system, so long as the number of coordinates is equivalent to the degrees of freedom of the system plus the number of independent constraint equations. However, with Lagrange's equation these can not only be commonly used coordinate systems but any set of parameters which adequately define a system's configuration. The combination of coordinates and parameters is known as the generalized coordinates and symbolized as q_n .

The selection of which coordinates are used can have a tremendous effect on the difficulty of solving a problem. Although not obvious at first, choosing a set of independent generalized coordinates, where the number of coordinates is equal to the system degrees of freedom without the need for constraint equations, allows the solution to be solved in a standard procedure. In the previous example, the pendulum could be defined by x - and y -positions and constraining the motion; however, specifying it in polar form leaves only one variable to analyze.

Work done by displacements in the direction x can be defined as

$$dW = F \cdot dx \quad (2.18)$$

where F is a force acting in the ordinary positive x direction. In the Lagrangian equation method there exists the concept of virtual work, which is performed by small virtual displacements.

These displacements are assumed to occur without an actual change in time and with the forces remaining constant. They also may or may not follow the kinematic or dynamic constraints on motion; however, Greenwood states in the usual case virtual displacements will follow the kinematic restrictions at an instant and assume that moving constraints have been stopped.

Virtual work and virtual displacements are written as δW and δx , respectively, to differentiate it from real displacements and work that take place following a passage of time. The equation would then appear as

$$\delta W = F \cdot \delta x \quad (2.19)$$

Generalized forces then allow each force and displacement to be interpreted in terms of the generalized coordinates. Skipping a few steps, the virtual work equation is then expressed as

$$\delta W = \sum_{i=1}^n Q_i \cdot \delta q_i \quad (2.20)$$

where i is equal to the number of generalized coordinates in the system and the general forces, Q , are equal to

$$Q_i = \sum_{j=1}^k F_j \frac{\delta x_j}{\delta q_i} \quad (2.21)$$

The proof for the Lagrangian will be left to the reader to research, but it is equivalent to

$$L = T - V \quad (2.22)$$

where T is the kinetic energy terms of system and V is the potential energy terms. By using the Lagrangian and generalized forces, Lagrange's equation is

$$\frac{d}{dt} \left(\frac{\partial L}{\partial \dot{q}_i} \right) - \frac{\partial L}{\partial q_i} = Q_i \quad (2.23)$$

where the equation can be used for each general coordinate, i , to form a system of differential equations.

CHAPTER 3

EQUIPMENT & DESIGN

3.1. PARAGLIDER TEST VEHICLE

In order to evaluate and validate the accuracy of the model presented in this paper, a powered paraglider test vehicle has been configured to match parameters set by the model. This section outlines the specifications and components of the vehicle.

3.1.1. COMPONENTS

The fuselage is a trike styled carriage sold by Hobby King, shown in Figure 27. The loose components, or those not mounted, are housed within the main tower, which is also used for mounting the control arms and motor. The loose components include the Castle Creations Thunderbird-54 electronic speed controller (ESC) and the Futaba radio receiver. The control arms are Futaba S3004 servos with metal arms that actuate independently to pull down on either control line for turns or both together to flare. On the aft side of the tower near the top, the NTM Prop Drive 35-36A 1400KV motor is mounted with the propeller in a pusher configuration. More information on the propeller size and selection will be discussed later in section 3.2. Performance data from the manufacturer is shown by Figure 28. To power the components a Flight Power 3S 4000 mAh 25C lithium polymer (LiPo) battery is attached underneath the deck with Velcro straps.



Figure 27: Paraglider Trike

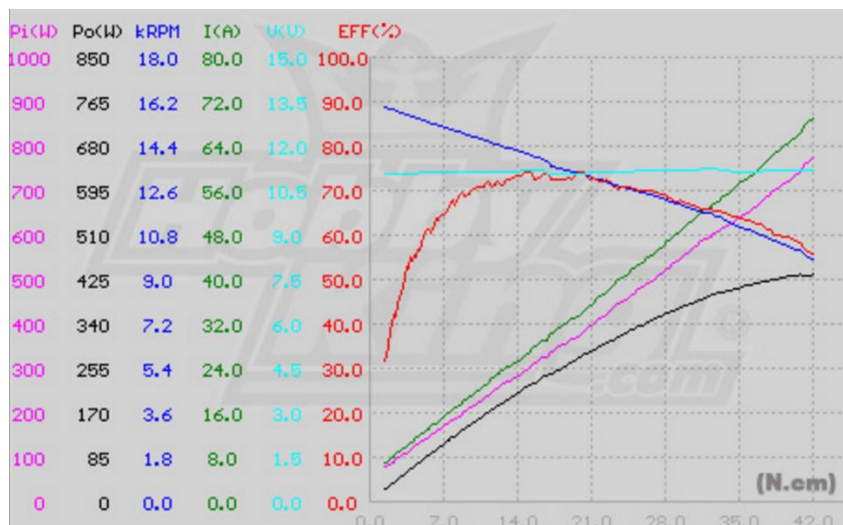


Figure 28: NTM 35-36A 1400KV Performance Data

Two parafoils were tested. The first is an elliptical 77 inch (1.95 m) span ripstop-nylon wing sold by Hobby King, shown in Figure 29. Like most parafoils it consists of a top and bottom surface, with vertical airfoil shaped fabric ribs placed periodically along its span. The leading edge

section is also truncated to allow ram-air inflation. However, unlike the parafoils used by Nicolaides and Furfaro the airfoil section has a curved bottom surface instead of flat.

Each half, port and starboard, uses four groups of lines to support the fuselage and one to control the trailing edge and brakes. Three of the four support line groups each lead to spanwise rows of attachment points. The last support line group is attached to the wing tip. These are all connected to a common harness and confluence point, which is mounted on the parafoil attachment bracket at the top of the fuselage tower. The mounting point allows for free rotating hinge movement between the wing and fuselage. The control line bypasses the harness and instead is fed through a tube on the attachment bracket on the fuselage and redirected to the servo control arms.



Figure 29: Hobby King Parafoil

The second parafoil is an Ozone Imp Quattro, with a 61 in (1.5 m) span, shown in Figure 30. Its intended use is for kiting sports where riders are pulled on snowboards, mountain boards, or

buggies by the parafoil in the wind. A similar parafoil made by the same company, the Razor, was used in development of iRobot's Griffon hybrid unmanned ground and air vehicle [24]. The kite can then be directed by pulling and pushing the lines to rotate the entire wing. This makes roll steering a natural choice when mounted on a paraglider. As with the Hobby King parafoil, the Quattro is constructed from ripstop-nylon and contains curved upper and lower skins with fabric ribs sewn vertically between them. The Quattro also features a coarse netting over the air intakes. Perhaps the most appealing feature of the Quattro is its simple rigging system. It uses three groups of lines for support and has one line connected to the trailing edge, which could be used for support or as a brake line. However, the lines only split into 15 attachment points on each side, compared to 53 per side on the Hobby King parafoil. This makes it much easier to adjust and analyze. The connection is nearly identical to that of the Hobby King parafoil, with the rigging lines attaching directly to the attachment bracket and the brake lines running through the same bracket but down to the servos instead.



Figure 30: Ozone Quattro Parafoil

3.1.2. MASS PROPERTIES

Determination of the mass properties of the fuselage was required for an accurate and reliable model of the paraglider system. In the system presented in this paper the fuselage is able to rotate around the parafoil attachment point, which affects the orientation of the thrust force. Increased weight considerably offset horizontally from the attachment point has a large effect on the fuselage's pitch angle during flight. This can be most dramatically seen during the case of a power-off glide. With no thrust to assist in rotation, the imaginary line p , shown by Figure 43, will naturally return to a vertical orientation, since weight will be applied straight down and the fuselage mass will desire the lowest potential energy state. This can also be seen to be where ϕ will be equal to $-i_p$. By altering the location of the center of gravity the parameters p and i_p change accordingly. The effect of repositioning the center of gravity can be seen in section 5.1.3.

In order to determine the center of gravity of the fuselage and its moment of inertia each component of the structure and equipment was weighed and located with respect to a fixed point. The exact references were in line with the rear edge of the base and the bottom of the rear wheels, as shown by Figure 31. Treating each component as a point mass, the common center of gravity for each coordinate, with respect to the reference point, can be found by using

$$R_j = \frac{1}{M_f} \sum m_i \cdot r_{ji} \quad (3.1)$$

where j is the desired coordinate (e.g. x , y , or z), M_f is the total mass of the fuselage and components, and m_i and r_{ji} are the mass of and distance to each component, respectively. In this way, the center of gravity is located at (R_x, R_y, R_z) .

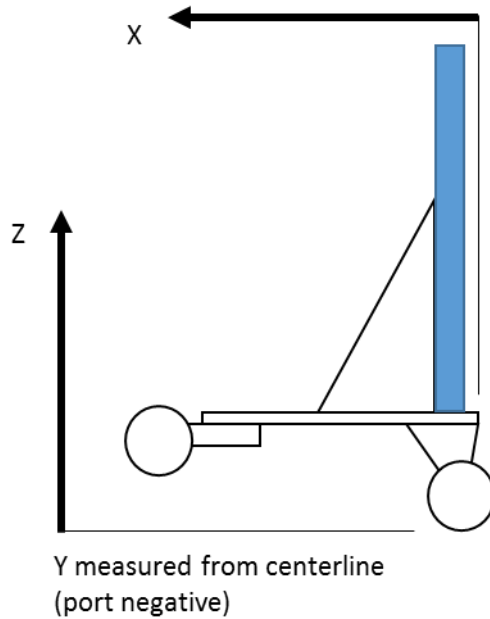


Figure 31: Reference Point for Measuring Component Locations

3.2. POWERPLANT SIZING AND TESTING

Properly planning and evaluating the performance of a paraglider requires knowledge of the system's powerplant capabilities. Due to lack of pitch control through conventional means, such as an elevator, the thrust generated is the primary source of pitch control for a powered paraglider vehicle. This is known as thrust only control and is discussed in section 2.7. Its effects are also compounded by the fact it acts far below the second body and creates a large moment arm, albeit, not directly on the second body, but rather through the confluence or connecting hinge point. This means to ensure stable flight and positive rates of climb the thrust must be balanced by proper rigging of the lines. In general, more thrust requires a reduced incidence angle of the wing.

Based on simulation results, the maximum thrust calculated was commonly around 2 lb; however, the thrust required for steady level flight was closer to 1 lb. In order to produce the thrust

required, there are multiple options in the design choice of the system's powerplant components. The primary driver is the electric motor. Its maximum amperage and KV rating, the number of revolutions per volt, determine how much power can be output and converted into thrust. However, it is the propeller that pushes the air and therefore is also chiefly important. The diameter of a propeller influences the amount of air that can be moved and pitch of the blades affects the performance as airspeed increases. Because the motor output is controlled per voltage, increasing the number of cells in series in a battery can also provide additional performance if necessary. However, all of the components must be compatible with each other, else the motor be overloaded or the battery draw more current than designed for.

With those factors in mind, the motor was chosen off recommended specifications for the fuselage. Different propellers could then be tested and analyzed at much cheaper cost than multiple motors. To accompany the motor's 1400 KV rating, a 3S, or three cells in series, LiPo battery was chosen with a discharge capability able to handle the maximum current draw from the motor. All that remained was the choice of propeller for the given rotation speed and maximum current draw. For analysis three different propellers were chosen, with diameter being the primary factor of interest. All were 3-bladed propellers with low pitch, for better performance at low speeds, produced by Master Airscrew. The sizes in consideration were 8x6, 10x5, and 12x6.

In an attempt to measure thrust output from the propellers, a fish scale was attached to the glider trike horizontally and then held to measure the pull generated. However, results were unreliable and a different method was required. In its place a test platform was constructed from thin plywood and epoxy. The platform consisted of a square base of 1 ft² with a shelf spanning the length of the base and about 3.5 inches wide raised 4 inches through the use of thin plywood walls. The motor was able to be attached underneath the shelf while the propeller sat on top without interference in a pusher configuration, as it would on the paraglider test vehicle. Two holes were cut into the shelf in an attempt to facilitate air flow to the propeller, ensuring proper

unhindered thrust values. The whole test platform was placed on a scale such that the propeller would push the platform down onto the scale, increasing the measured weight. To counteract the large rotation caused by the motor, the platform was weighted down and a block was placed in the path of rotation.

The motor and propeller measured are the same models used on the paraglider test vehicle, as well as the transmitter, receiver, and ESC to control them. An alternative battery was also used during test but should provide the same power delivering capabilities as the vehicle's regular battery. The battery used during testing was a Thunder Power RC 3S 1300 mAh LiPo rated for 45C continuous (58 A) and 90C burst (117 A). In addition to the flight required items, an Astro Flight 101D wattmeter was used to measure the current and power drawn from the battery. The scale used was an Ohaus SD75, which has a readability of 0.1 lb. The whole test configuration can be seen in Figure 32.

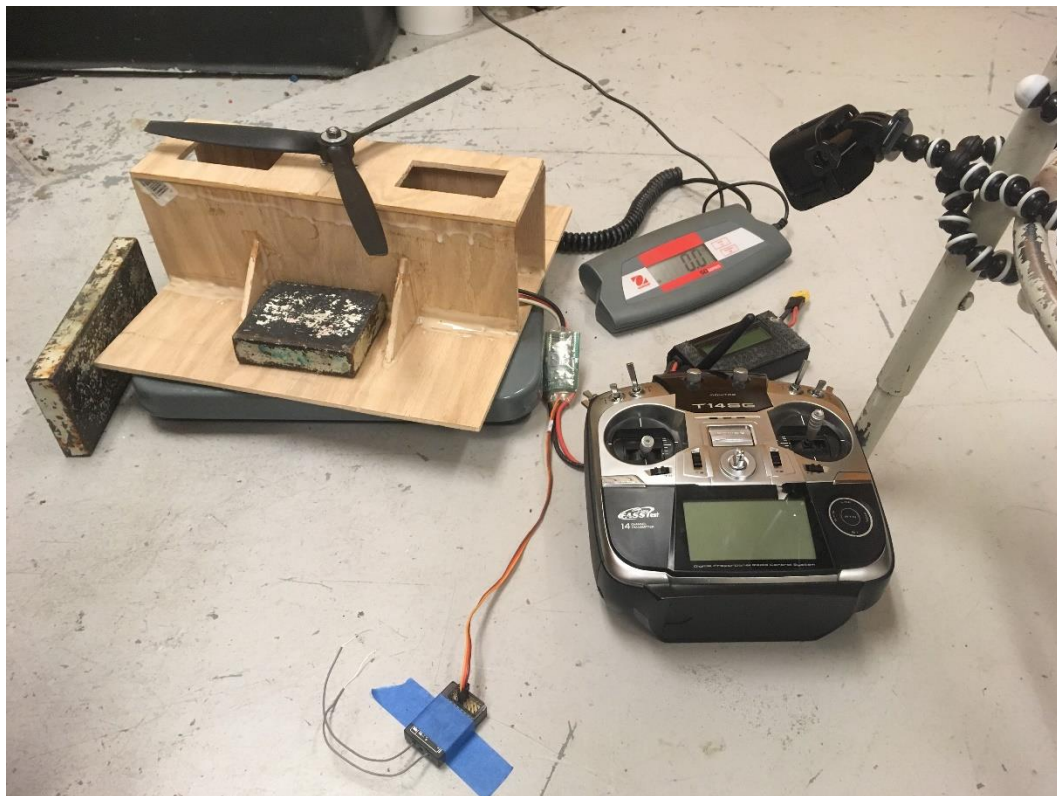


Figure 32: Powerplant Testing Configuration

Each run was captured on a GoPro camera and visually analyzed after testing for throttle position, thrust, power, and current. In this manner, testing could be performed quickly, without the need to record information in real time.

The thrust data collected for each propeller over several tests can be seen in Figure 33 with trend lines as well as the current draw in Figure 34. The data has also been distilled into Table 2, Table 3, and Table 4 outlining the average performance at easily recognizable throttle positions. Figure 87 and Figure 88 are located in the Appendix A and show the relationship between throttle position versus power and theoretical endurance, respectively. It should be noted that these are tests under static conditions, but given the low speeds during flight these numbers should be fairly accurate expected values. Additionally, the data appears linear, with R2 values between 0.96-0.98, and the zero thrust throttle position is around 15%, which matches the behavior of the system during testing.

The maximum thrust for the 8x6 is 2.1 lb. Recalling the simulated maximum thrust was generally around 2 lb as well, this propeller provides adequate thrust for the entirety of the operating range, and as such enables finer control from the pilot. Based on the current draw for 1 lb of thrust, a commonly calculated level flight value, the paraglider has a theoretical endurance of 19 minutes at 12.8 A with its regular 4000 mAh battery.

The 10x5 shows improved capability with a maximum thrust of 3.4 lb at full throttle. This is much higher than the thrust required for steady flight and even greater than the maximum allowable thrust; however, it would provide a reserve of available power, should more be needed. Drag numbers are estimated or taken from performance data that may not be representative of the parafoil in use, and therefore, could require more thrust than calculated. It is unlikely however that the full 1.5 lb over the predicted maximum possible would ever be utilized. Theoretical endurance is similar to the 8x6, despite the much larger performance.

Similar to the 10x5, the 12x6 has a maximum thrust of 3.3 lb; however, at all lower throttle positions the thrust is higher than the 10x5. It has the same benefit of providing a large amount of excess power, but tapers off at higher throttle. Looking at Table 4 and Figure 34 the current draw from the battery is 63 A, where the maximum rated current for the motor is 55 A. This propeller is not a good choice since the thrust is needlessly larger than required and at full draw overloads the motor.

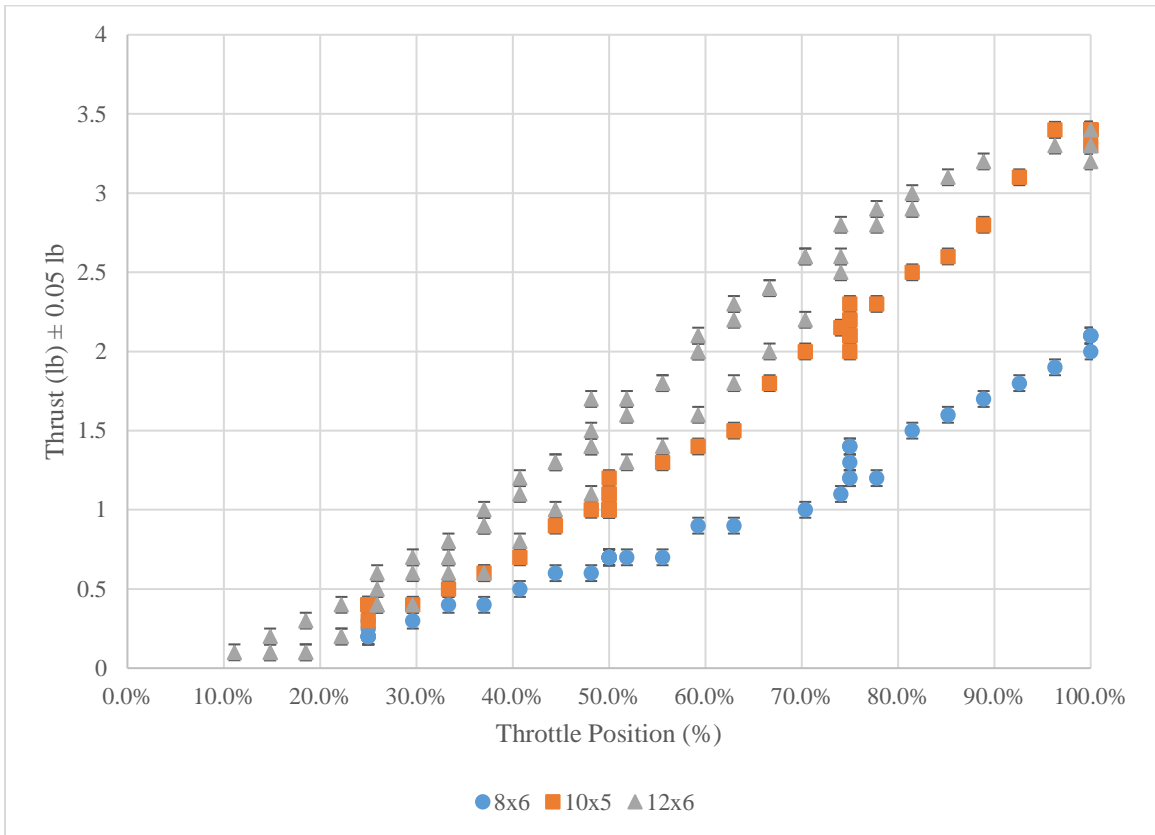


Figure 33: Powerplant Thrust Output with Throttle Input

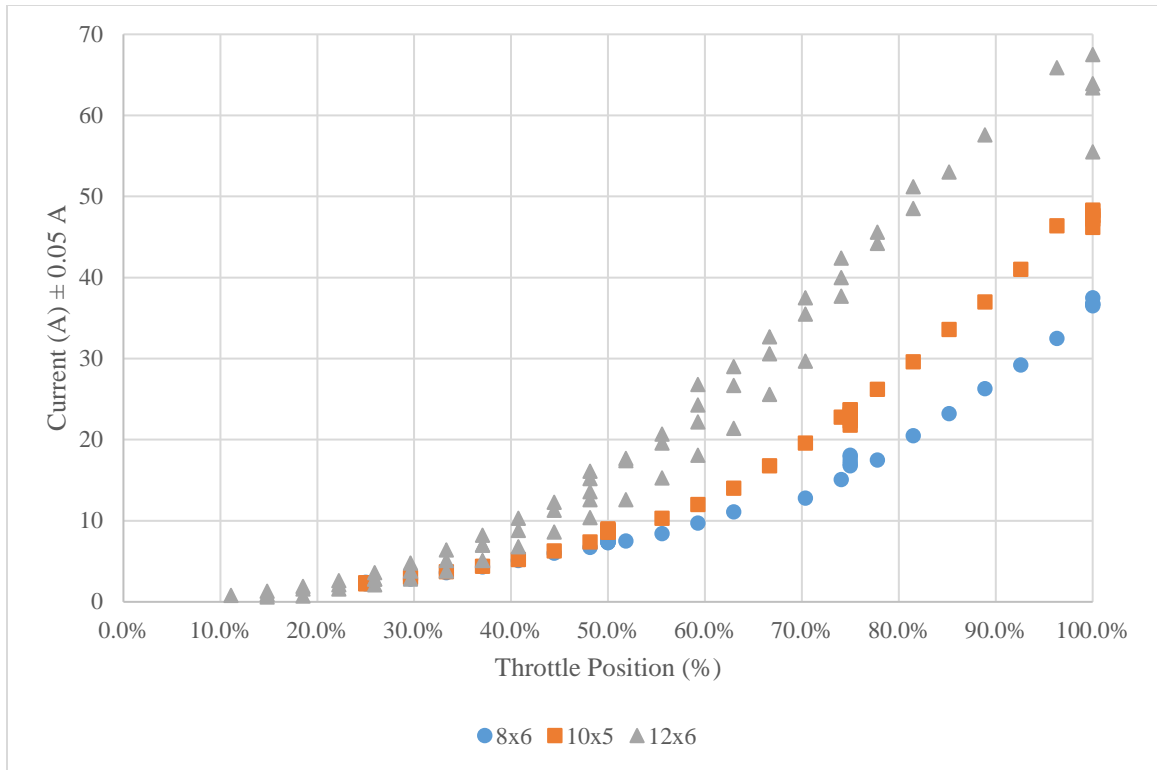


Figure 34: Powerplant Current Draw with Throttle Input

Throttle	Thrust (lb) ± 0.05 lb	Current (A) ± 0.05 A	Power (hp) ± 6.7·10 ⁻⁵ hp
25%	0.22	2.3	0.039
50%	0.70	7.4	0.12
75%	1.3	17	0.27
100%	2.1	37	0.56

Table 2: 8x6 3-Blade Propeller Powerplant Data

Throttle	Thrust (lb) ± 0.05 lb	Current (A) ± 0.05 A	Power (hp) ± 6.7·10 ⁻⁵ hp
25%	0.39	2.3	0.037
50%	1.1	8.7	0.13
75%	2.1	23	0.34
100%	3.4	48	0.67

Table 3: 10x5 3-Blade Propeller Powerplant Data

Throttle	Thrust (lb) ± 0.05 lb	Current (A) ± 0.05 A	Power (hp) ± 6.7·10 ⁻⁵ hp
25%	0.48	2.8	0.047
50%	1.5	14	0.21
75%	2.6	40	0.53
100%	3.3	63	0.78

Table 4: 12x6 3-Blade Propeller Powerplant Data

3.3. LINE RIGGING

Perhaps the most important longitudinal aspect of the paraglider system is the rigging angle, which is critical for ensuring proper and optimal performance. The angle set affects the gliding angle of attack, and therefore lift to drag ratio and glide performance. In the model defined by this paper and simulation, the rigging angle is defined by altering the distance from the leading edge of the wing to the connection, or confluence, point and the distance between the trailing edge and connection point. When these two lengths are known, along with the chord of the parafoil, the rigging angle can be found as the angle between the chordline and horizontal when the connection point is located directly under the quarter-chord position. This is also defined as the incidence angle when θ is equal to zero according to section 4.1 covering incidence angle and is shown graphically by Figure 39. However, on many parafoils the lines do not directly attach to the leading edge and the rear is primarily used for skid-steering braking, not support.

Additionally, the lines are not placed at the ends of the chordline and not even on the chordline. Instead, the lines attach to the bottom skin of the parafoil, which is shaped to the lower half of its airfoil. Without knowledge of the parafoil cross-section determining exact line lengths is difficult. These issues are only compounded by the fact that the uninflated wing structure and shape will be different than the fully deployed form. With flat-bottomed airfoils, like those used by Nicolaidis, the inflated structure will be more or less equivalent to the deflated form, so long as the flat bottom is maintained when adjusting lines.

The orientation of the Quattro is entirely maintained by the front lines. The parafoil is secured at two positions, as shown by Figure 35, through the red and blue lines. The rear line, shown to be slack, holds no weight. Instead, the rest of the wing's form is held through the inflation pressure, which provides an outward force to maintain the structure. By adjusting the length of the red and blue lines the orientation can be seen to rotate; however, as stated previously, without knowledge of the airfoil, an exact measurement is not possible.

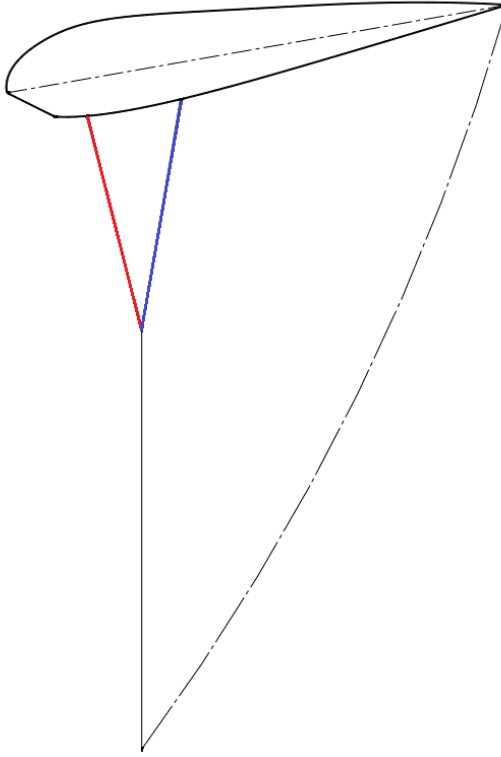


Figure 35: Ozone Quattro Parafoil Rigging Configuration

Likewise, proper lateral dimensioning is essential for proper flight behavior. This primarily refers to the arched or dihedral shape of the parafoil. Wing arc helps strengthen its structure, due to the sides being pulled outward. By pulling on the sides the parafoil is kept taut and less likely to succumb to gusts. However, too much arc reduces the total vertical force, with decreased lift and increased drag. It also creates roll instability through the dihedral effect when subjected to sideslips.



Figure 36: Ozone Quattro Parafoil with Reduced Arc Anhedral

The rigging lengths for the parafoil each flight test are listed in Table 5-Table 10 and correspond to the attachment positions indicated by Figure 37. The A and B row lines connect to a common line while the C lines on the tip of the wing converge to another. The AB common line is 16.5 inches long and the C common line is 20.75 inches long.

	1	2	3	4
A	18.5	20.5	22.5	24.75
B	19.0	20.75	22.75	24.75
C	12.25	12.75	14.5	

Table 5: 1st Flight Port-Side Line Lengths (inches)

	1	2	3	4
A	18.5	20.75	22.5	23.75
B	19.0	20.75	22.5	24.75
C	12.25	12.75	14.25	

Table 6: 1st Flight Starboard-Side Line Lengths (inches)

	1	2	3	4
A	18.0	19.5	21.25	23.0
B	19.0	20.5	22.0	23.5
C	12.25	12.75	14.5	

Table 7: 2nd Flight Port-Side Line Lengths (inches)

	1	2	3	4
A	18.0	19.5	21.25	23.0
B	19.0	20.5	22.0	23.5
C	12.25	12.75	14.25	

Table 8: 2nd Flight Starboard-Side Line Lengths (inches)

	1	2	3	4
A	18.375	20.125	21.75	24.0
B	19.0	20.75	22.5	24.75
C	12.25	12.75	14.5	

Table 9: 3rd Flight Port-Side Line Lengths (inches)

	1	2	3	4
A	18.375	20.125	21.75	24.0
B	19.0	20.75	22.5	24.75
C	12.25	12.75	14.25	

Table 10: 3rd Flight Starboard-Side Line Lengths (inches)

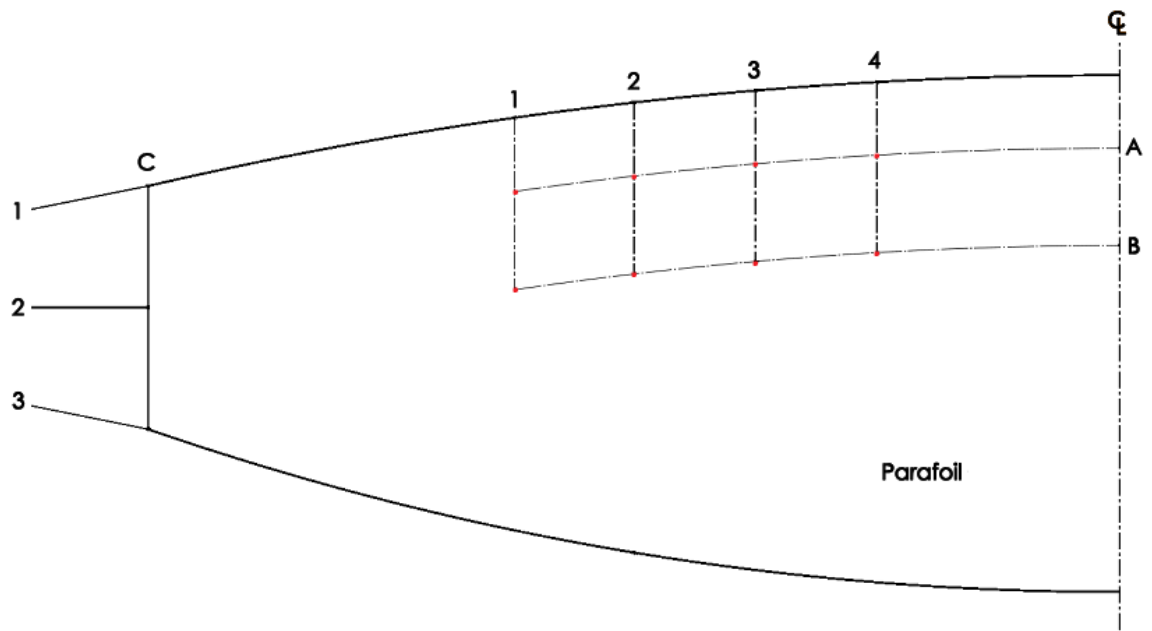


Figure 37: Reference for Line Designations

CHAPTER 4

ANALYSIS

4.1. INCIDENCE ANGLE

Unlike fixed wing conventional aircraft, a paraglider wing changes its incidence angle based on different flight conditions. Since the wing is usually attached at a hinged point it rotates as it is pulled back by increased drag or rotated by a large thrust moment. As a result, the incidence must be calculated at each point in the simulation to ensure the correct angle of attack is used.

Initially, a configuration similar to a 4-bar mechanism was utilized in order to make the program as general as possible. This allowed for a horizontal and vertical offset to be used for two separate attachment points for the leading and trailing edge lines. 4-bar mechanisms are single degree of freedom machines, which means that for the definition of one rotation angle the whole system orientation exists as a function of that angle. Using Figure 38 as an example, if any piece of the mechanism is manipulated the other components are able to move freely as well; however, if a motor were attached to a linkage joint the whole mechanism would become fixed while the motor is off but move as the motor drives the rotation of one linkage.

Applied to a paraglider system, the angle between the leading edge line and vertical, shown by θ in Figure 38, could be defined as one of the general coordinates in a Lagrangian system. In this way, the configuration of the parafoil could always be determined no matter how θ changes, because it is the driving parameter for the mechanism; resulting in a more versatile simulation that can accurately model paraglider systems without separate attachment points. However, this

approach was abandoned as a single attachment point was common for most models of paragliders and the calculation was more straightforward.

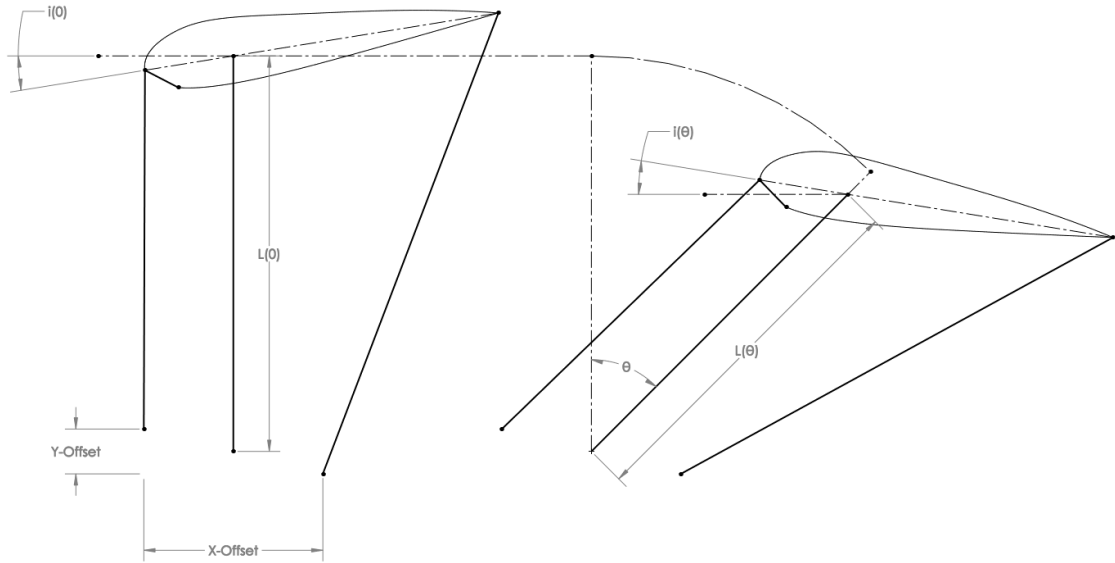


Figure 38: Wing Represented as a 4-Bar Mechanism

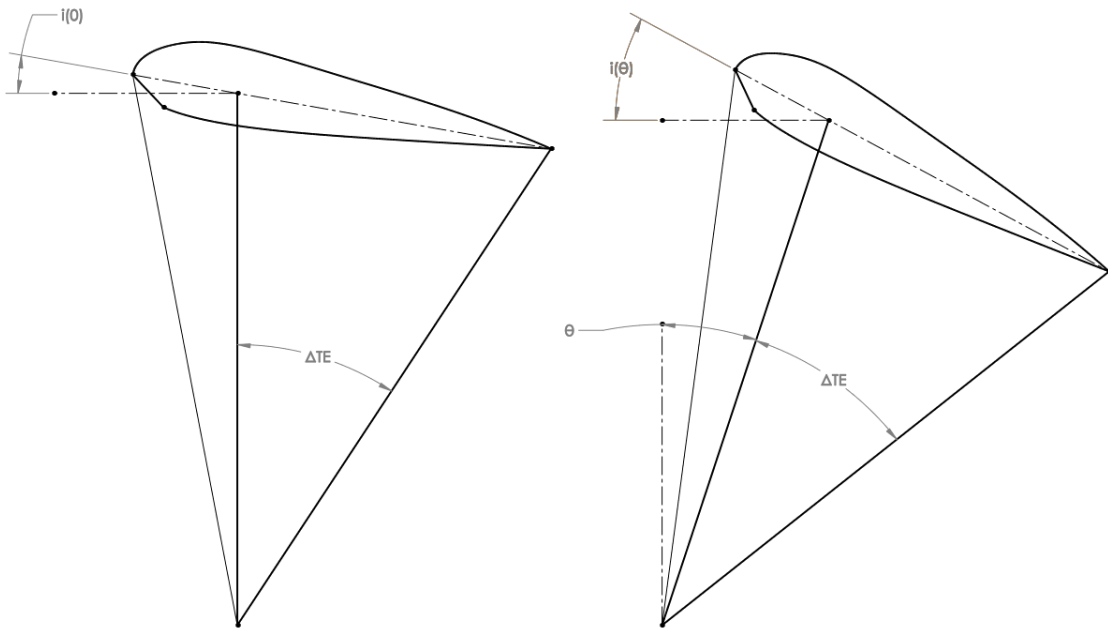


Figure 39: Wing Represented with Rigid Geometry Joining at a Single Point

An advantage of modeling the system with a single attachment point is its constant geometry. Regardless of how the parafoil pitches, the angles between the lines will be fixed as well as the distance from the attachment point to the quarter-chord of the wing, l_{ac} . This can be seen in Figure 38 where l_{ac} , represented as $L(0)$ and $L(\theta)$, changes as the pitch angle increases. Similarly, the incidence angle will also increase or decrease at a variable rate as the pitch angle changes. To find incidence angles the wing pitch angle, θ , for each time step is used to derive the geometry of the system, which is then related to the horizontal axis. This can be seen by equations 4.1 and 4.2, where Δ_{TE} is the angle between the quarter-chord line and the trailing edge line.

$$i(\theta) = \tan^{-1} \left(\frac{c/4y\text{-coordinate} - TEy\text{-coordinate}}{c/4x\text{-coordinate} - TE_x\text{-coordinate}} \right) \quad (4.1)$$

$$i(\theta) = \tan^{-1} \left(\frac{l_{ac} \cos \theta - l_{TE} \sin(\theta + \Delta_{TE})}{-l_{ac} \sin \theta + l_{TE} \sin(\theta + \Delta_{TE})} \right) \quad (4.2)$$

Alternatively, the equation can be solved for the zero-degree wing pitch angle, simplified in equation 4.3. This zero-degree wing pitch angle is referred to by this paper as the rigging angle.

$$i(0) = \tan^{-1} \left(\frac{l_{ac} - l_{TE} \sin(\Delta_{TE})}{l_{TE} \sin(\Delta_{TE})} \right) \quad (4.3)$$

Taking advantage of the rigid geometry formed by the system having a single attachment point, any subsequent incidence angle will simply be the zero-degree wing pitch incidence angle plus the pitch angle of the wing, or,

$$i(\theta) = \theta + \tan^{-1} \left(\frac{l_{ac} - l_{TE} \sin(\Delta_{TE})}{l_{TE} \sin(\Delta_{TE})} \right) \quad (4.4)$$

4.2. SYSTEM

Consider the pendulum from Figure 25 and Figure 26. If an additional mass is attached below the original and allowed to rotate about it the system becomes a double pendulum, shown by Figure 40. Describing the motion of the double pendulum is much more complex than the single case,

since there are now two masses to keep track of, with two constraint equations restricting movement. With the addition of any forces that vary direction the problem involves much more bookkeeping. While it can be described in terms of Cartesian coordinates without too much difficulty, it has already been proven that the degrees of freedom are equivalent for any set of coordinates used to describe the system. Instead, similarly to the single pendulum, polar coordinates could also be used, using (r_1, θ_1) and (r_2, θ_2) rather than (x_1, y_1) and (x_2, y_2) . However, since the arm lengths are set to the constant values of R_1 and R_2 , the constraints are built in and the system is then only a function of θ_1 and θ_2 . The Newtonian solution requires defining tension forces to connect the two masses, constraint equations, and results in four equations of motion; however, this can be reduced to two through substitution. For this system the solution is not much longer or overly complex, but adding any more complexities, such as additional forces or another mass, the solution can become needlessly burdensome. In contrast, adding an additional masses to the Lagrangian system is as simple as adding another coordinate and deriving the Lagrangian with respect to it. This is similar to the approach taken by Quisenberry, where he was able to create a chain of small masses and derive the series for a solution.

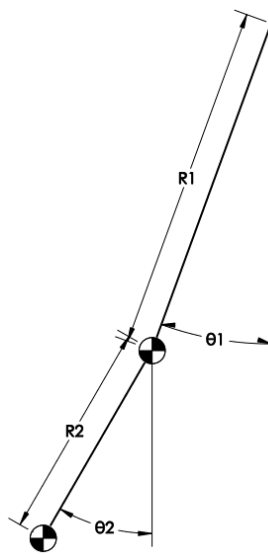


Figure 40: Double Pendulum

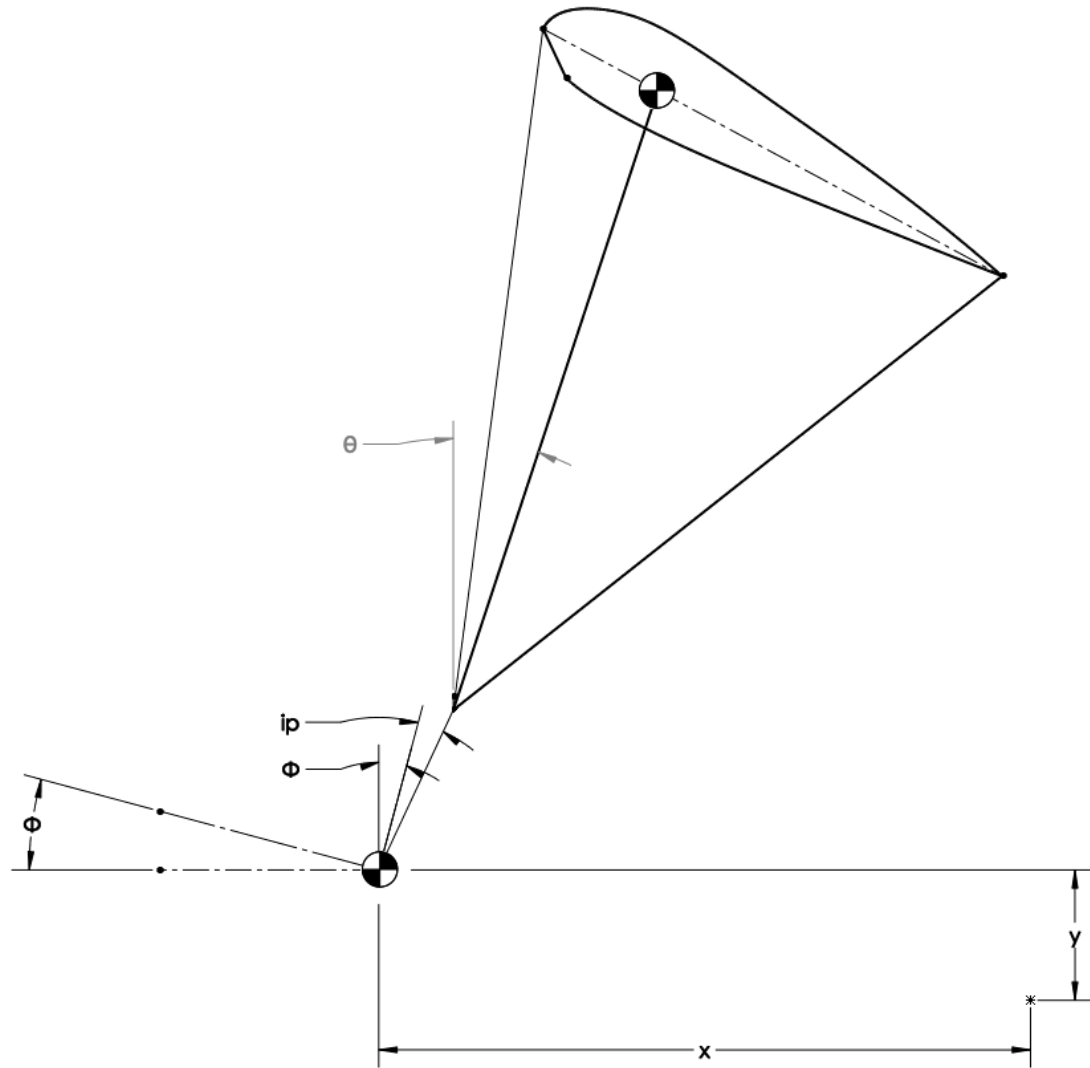


Figure 41: Proposed System

The proposed model, shown in Figure 41 resembles that of a double pendulum, with a few alterations. Representing an airborne vehicle, the pendulum is no longer fixed but is allowed to move in space. This movement is reflected by Cartesian x- and y-coordinates related from a fixed point to the lower body, which will be seen to be the paraglider fuselage. They are defined as left and up representing positive x and y travel, respectively. In this way the altitude change and ground distance can be determined in an effortless fashion. Additionally, instead of both masses being suspended from a fixed point at the top of the system, the top point is a freely moving mass supporting the bottom mass through lift and the same hinged relation as the double

pendulum. The coordinates defining their orientation still come from the polar definition method. The lengths are defined as constant values in the analysis as p and l_{ac} so, like the pendulum examples, the definition is simplified to angles only. The angles are defined in a similar manner as well. These are given as θ and ϕ , and defined as clockwise rotation representing a positive angle.

To better relate the system to the physical vehicle the coordinates and other system components will be described by their physical purpose. The top mass, marked by the center of mass symbol, describes the wing and its assumed point mass position at the quarter-chord. The bottom mass, marked with the same symbol, represents the paraglider fuselage center of mass. Both masses are connected through the hinged confluence point of the leading and trailing edge lines of the wing. This is achieved by creating the imaginary lines p and l_{ac} , shown in Figure 43. The line p represents the distance between the fuselage center of mass and the parafoil attachment point. Likewise, the line l_{ac} represents the distance between the wing center of mass, and aerodynamic center, and the parafoil attachment point. The angle of the l_{ac} line, and by extension the pitch angle of the parafoil, is given by θ . The rotation of the fuselage, which is normally directly related to or the same as pitch angle of the wing on a conventional aircraft, is represented separately by the angle ϕ . Normally, the pitching angles would both be denoted as different thetas through the use of subscripts, but for the simplicity and clarity of the analysis a completely separate variable is used instead. An important aspect in properly defining the system is allowing the center of mass of the fuselage to be varied with respect to the confluence point. This has already been seen with the line p , but the angle i_p relates the length with a direction. The definition can be seen visually through Figure 42. For this reason, most calculations in the analysis involving the wing will contain the angle formed by the sum of ϕ and i_p .

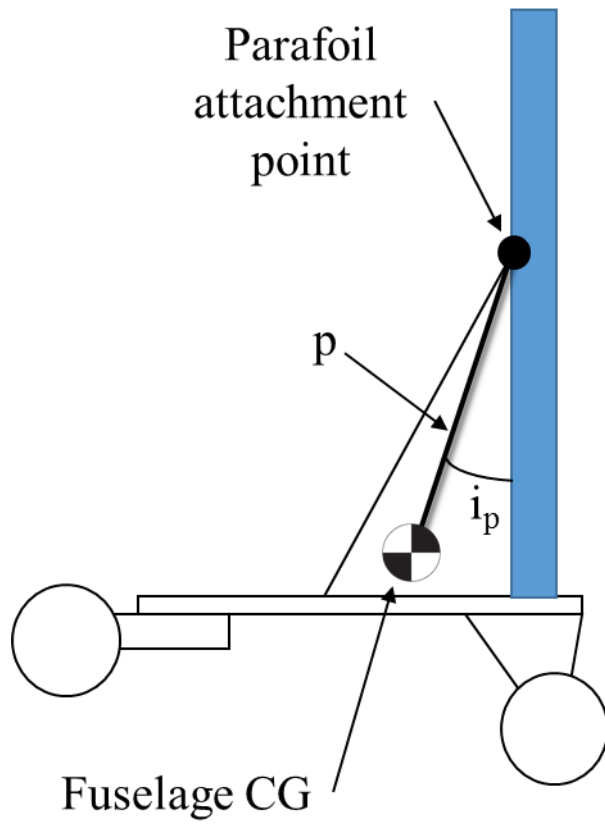


Figure 42: Fuselage Center of Gravity Definition

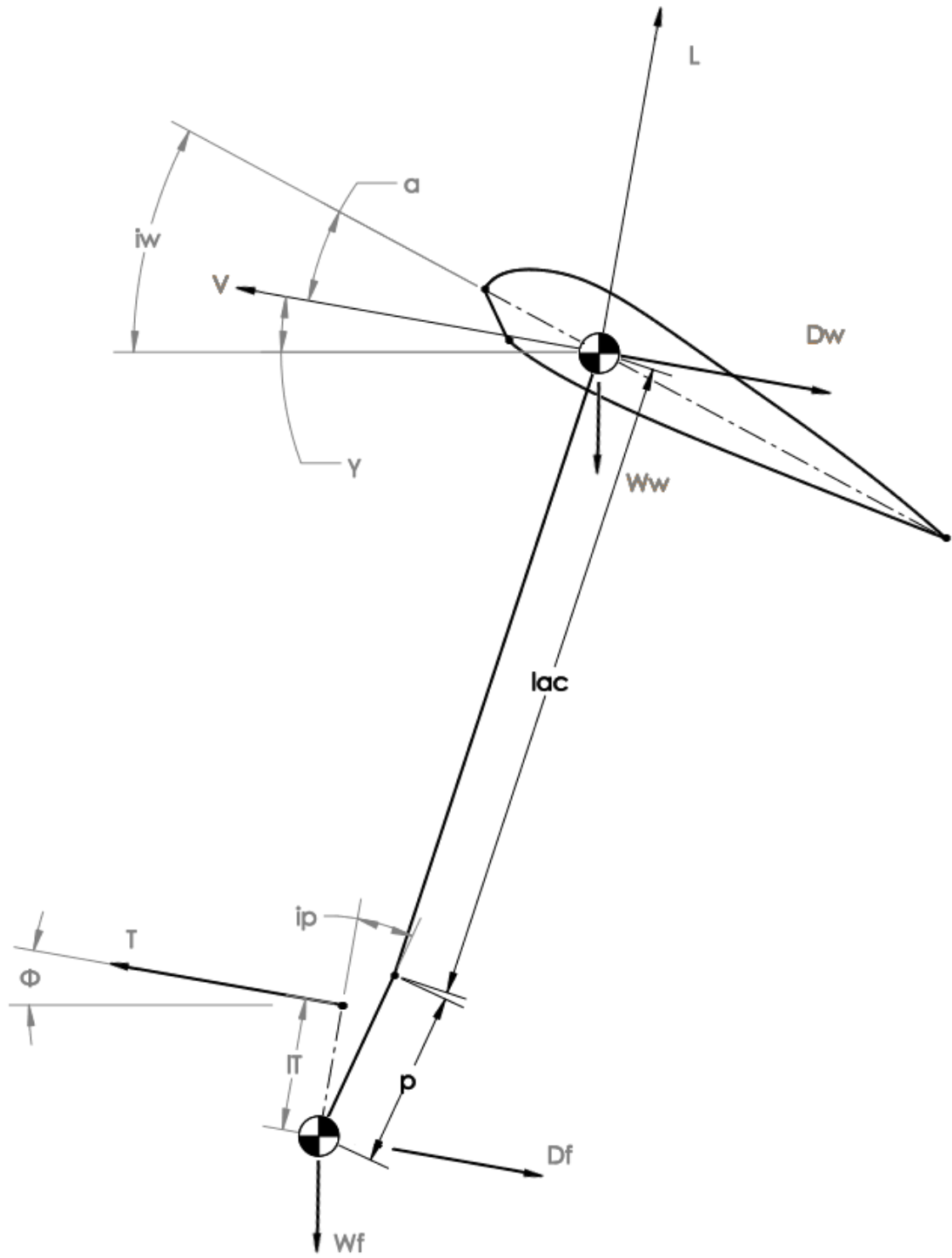


Figure 43: Forces Acting on Proposed System with Angles and Dimensions

The system contains four forces influencing the kinetic energy of the system and two weight forces affecting the potential energy. The wing generates lift and drag based on its velocity and angle compared to the incoming airflow, just like a conventional aircraft. In this system lift and drag are symbolized by L and D_w , respectively. The wing drag acts parallel to the incoming air and lift acts perpendicular to it. In Figure 43 the wing is climbing in the direction of the velocity vector, V . Since the general coordinate y is positive in the upward direction, this indicates a positive direction for the velocity and creates a positive flight path angle, γ , which is defined by the tangent of vertical component of velocity over the horizontal component of velocity. This can also be referred to as the climb or descent angle, and is shown by,

$$\gamma = \tan^{-1} \left(\frac{y}{x} \right) \quad (4.5)$$

The analysis currently lacks any wind modeling, and as a result climb angle also represents the incoming air direction. Wing incidence, i_w , is defined by the angle between the chord line and horizontal and explained further in the previous section. Therefore, the angle of attack, α , to calculate the magnitude of the lift and drag vectors becomes,

$$\alpha = i_w - \gamma \quad (4.6)$$

Lift conforms to the traditional lift equation,

$$L = \frac{1}{2} \rho v^2 S C_L \quad (4.7)$$

and drag to its traditional equation,

$$D_w = \frac{1}{2} \rho v^2 S C_D \quad (4.8)$$

where S is the wing area, and C_L and C_D are the lift and drag coefficients for the current wing angle of attack, respectively. In this model the lift and drag coefficients are found given

aerodynamic performance data, discussed further in section, and calculating intermediate values with linear interpolation based on the current angle of attack.

Drag from the fuselage, D_f , is calculated from the fuselage's velocity magnitude in the direction of its own flight path angle (not shown in Figure 43), which may differ from that of the wing.

The drag follows the traditional drag equation,

$$D_f = \frac{1}{2} \rho v^2 A C_D \quad (4.9)$$

with the frontal area, A , being measured from the physical vehicle and drag coefficient, C_D , being estimated from similar body shapes. However, the drag coefficient is considered to be constant and independent of angle of attack. The fuselage is considered not to produce any considerable amount of lift and is omitted from the analysis.

Thrust, T , is generally offset a considerable distance, relatively, from the center of gravity of the fuselage, due to the large clearance needed from by the propeller. Thrust is considered to be aligned with the fuselage and only vary with the fuselage pitch angle, ϕ . As such, only the vertical distance from the center of gravity to the thrust line, l_T , is needed for analysis. The angle i_p is shown again in Figure 43 as a reminder that the solid line p does not represent the fuselage of the glider. Rather the dashed line l_T provides a better representation of the fuselage orientation. Then it can be easily seen that the thrust will align with the fuselage body. Thrust values can be set in the simulation with functions or step inputs based on elapsed time, explained in the simulation guide in Appendix B. Realistic values for thrust were found by experimentation outlined in section 3.2.

The weight of the fuselage and wing, W_f and W_w , respectively, simply contribute to the potential energy of the system. Since the test vehicles available were powered by electric motors this analysis considers the mass to be constant. The code could be easily modified to account for a

changing mass if a combustion engine were used; however, it might be determined to have little effect based on the duration of the simulation.

4.3. AERODYNAMIC DATA

Of the utmost importance is determining an accurate and useful aerodynamic model of the paraglider. Body drag from the fuselage is relatively straightforward. The traditional drag equation, shown by equation 4.9 can be used and is explained in the previous section. There exists some error from the constant C_D assumption, but by assuming the body is a point mass and applying the equation to a system as a whole, the simple drag equation should be accurate enough for a rough estimate, without the complexities of testing its drag experimentally or otherwise.

The biggest challenge was determining an accurate lift and drag model for the parafoil. The first approach involved importing the airfoil shape of the test vehicle's parafoil into XFLR5 and running an analysis to determine the lift curve slope and drag information. CFD has been shown to provide an estimate of aerodynamic performance for rigid parafoils by Cao, but results in a 2D panel method solver have been unproven. However, an even larger issue exists with the capability of the solver to calculate high angle of attack information. This model is used to determine responses to inputs that could potentially cause large disturbances, so the angle of attack can reach higher values than the analysis can accurately provide. When combined with the simulation calculation method of linear interpolation, the lift and drag can raise quickly to large and unrealistic values at angles of attack beyond stall. As a result, data across a large range of angles of attack was a necessity. Additionally, this approach ignores the natural flexibility in a parafoil wing.

The second approach to parafoil lift and drag modeling involved using experimental data. Nicolaidis performed wind tunnel experiments in an effort to determine realistic expected performance. His study included data for a range of angles of attack from -7° to 67° . With a

large sample of lift and drag information a natural response from the paraglider can be assured, without any inflated values from extrapolation. This approach holds the largest potential for accurate data, in terms of assumptions made; however, it is only applicable to parafoils of the same geometry and size without incurring inaccuracies of its own. In comparison, the parafoils employed by the test vehicle are tapered and curved, unlike the one used by Nicolaides, which was square and flat-bottomed. The aspect ratios of the wings differ as well, with the test vehicle's around 4 for the Hobby King parafoil, 2.4 for the Ozone Quattro, and 3 for Nicolaides'. While the effect of the aspect ratio on true performance is not known, from Figure 4 a maximum lift to drag ratio could be projected around 8.25 from preceding aspect ratio data for the Hobby King parafoil; although, this is a simple extrapolation and should not be considered a conclusive answer to adapting the data. The data from Furfaro's research was also considered. However, it has the same assumptions as the CFD analyses of a 2D rigid wing without any clear benefit. Observing the data shows a maximum lift to drag ratio of almost 25, which is a clear difference from expected results. For this reason, Furfaro's test data was not applied during analysis with any considerable amount of confidence. As seen by research by Uddin the flexibility of a parafoil can have a tremendous effect on its section shape, and only furthers the decision to use a data from a flexible wing.

Theoretical versus actual performance data differs even more when considering how slight changes in camber drastically affect the resulting lift and drag. Consider two very similar airfoils, the NACA 1412 and 2412. Although the airfoils differ only in their amount of camber from 1% to 2%, respectively, the small difference in camber results in a difference of its lift to drag ratio from 83.8 to 101.4, respectively. This is according to an XFOIL analysis, which can vary based on parameters used in its control, but the trend is the same to varying degrees. The XFOIL analysis can be found in Appendix A. Considering how the wing shape affects the

behavior of the system, there is a large amount of uncertainty at the core of any theoretical analysis.

One aerodynamic aspect that was ignored was drag created by each of the support lines, or line drag. Due to the complexities of adding another force into the middle of the system, this was set aside for later work. However, there are simple ways of including this additional drag. The first is to calculate the drag created by a length of line and then multiply that value by the total length of line used in rigging the parafoil. The location by which the force acts is then presumably the center of mass of the lines, which in this case would probably be safe to estimate based on the distribution of the lines. That is to say, the lines tie together into groups the closer to the attachment point they are, so there are more lines at the top near the parafoil than are lower near the confluence point. The other method would be to use experimental data not corrected to exclude line drag. This only applies to full 3D paraglider wing testing, since an experiment spanning the length of a section would not contain rigging lines. The experiments conducted by Nicolaidis and Tragarz provide data that has been corrected to exclude line drag; however, he also included a section of unaltered data, which shows the uncorrected data. Unfortunately, this method has two downsides when applied to the full paraglider system. The lines in his case may have been much longer or shorter than those that are used in the analysis, causing an over- or under-estimate of the drag. The second disadvantage is the drag would then no longer occur at the center of mass for the lines but instead the aerodynamic center of the wing.

4.4. ANALYTICAL MODEL

Adaptation of the system described earlier for use with the Lagrangian Equation begins by defining the physical relationships between the masses and generalized coordinates. These can be seen with Figure 41. Here the x and y Cartesian coordinates for each mass are given only in

terms of the generalized coordinates x , y , ϕ , and θ . Lagrangian position and velocity definitions can be seen as

$$x_1 = x \quad (4.10)$$

$$y_1 = y \quad (4.11)$$

$$x_2 = x - p \sin(\phi + i_p) - l_{ac} \sin \theta \quad (4.12)$$

$$y_2 = y + p \cos(\phi + i_p) + l_{ac} \cos \theta \quad (4.13)$$

$$\dot{x}_1 = \dot{x} \quad (4.14)$$

$$\dot{y}_1 = \dot{y} \quad (4.15)$$

$$\dot{x}_2 = \dot{x} - p \cos(\phi + i_p) \dot{\phi} - l_{ac} \cos(\theta) \dot{\theta} \quad (4.16)$$

$$\dot{y}_2 = \dot{y} - p \sin(\phi + i_p) \dot{\phi} - l_{ac} \sin(\theta) \dot{\theta} \quad (4.17)$$

with equations 4.10-13 describing positions and equations 4.14-17 being their corresponding time derivatives, or velocities. In the equations above, p is the distance from the cg of the fuselage to the attachment point of the parafoil, i_p is the incidence angle between the attachment point and vertical, and l_{ac} is the length of the imaginary line from the attachment point to the aerodynamic center, estimated to be the quarter-chord position.

The Lagrangian is given by equation 2.22 and is a description of the energy in a given system. Specifically, kinetic and potential energy and are symbolized by T and V , respectively. Kinetic energy is given for each of the two masses and evaluates as

$$T = \frac{1}{2} m_1 \dot{x}_1^2 + \frac{1}{2} m_1 \dot{y}_1^2 + \frac{1}{2} J_1 \dot{\phi}^2 + \frac{1}{2} m_{2x} \dot{x}_2^2 + \frac{1}{2} m_{2y} \dot{y}_2^2 \quad (4.18)$$

where m_{2x} and m_{2y} are the theoretical mass of the parafoil with added “apparent mass” surge and plunge effects, respectively. In this system the only potential energy terms are those due to gravity for the two bodies and is given simply as

$$V = m_1 g y_1 + m_2 g y_2 \quad (4.19)$$

It is important to remember that m_1 and m_2 are only the physical masses of the objects, since “apparent mass” terms only apply to dynamic motion.

With T and V, the Lagrangian becomes,

$$L = \frac{1}{2}m_1\dot{x}^2 + \frac{1}{2}m_1\dot{y}^2 + \frac{1}{2}J_1\dot{\phi}^2 + \frac{1}{2}m_{2x}(\dot{x} - p \cos(\phi + i_p)\dot{\phi} - l_{ac} \cos(\theta) \dot{\theta})^2 + \frac{1}{2}m_{2y}(\dot{y} - p \sin(\phi + i_p)\dot{\phi} - l_{ac} \sin(\theta) \dot{\theta})^2 - m_1gy - m_2g(y + p \cos(\phi + i_p) + l_{ac} \cos \theta) \quad (4.20)$$

which does not simplify well.

Recalling the Lagrange’s Equation as

$$Q_i = \frac{d}{dt} \left(\frac{\partial}{\partial \dot{q}_i} L \right) - \frac{\partial}{\partial q_i} L \quad (4.21)$$

where q_i is a general coordinate and Q_i is the forces in that coordinate. Setting up this system requires the equation to be put in terms of each generalized coordinate. With four generalized coordinates, the equation evaluates to

$$Q_x = \frac{d}{dt} \left(\frac{\partial}{\partial \dot{x}} L \right) - \frac{\partial}{\partial x} L \quad (4.22)$$

$$Q_y = \frac{d}{dt} \left(\frac{\partial}{\partial \dot{y}} L \right) - \frac{\partial}{\partial y} L \quad (4.23)$$

$$Q_\phi = \frac{d}{dt} \left(\frac{\partial}{\partial \dot{\phi}} L \right) - \frac{\partial}{\partial \phi} L \quad (4.24)$$

$$Q_\theta = \frac{d}{dt} \left(\frac{\partial}{\partial \dot{\theta}} L \right) - \frac{\partial}{\partial \theta} L \quad (4.25)$$

Notice, the Lagrangian must now be derived with respect to each coordinate and the time derivative of each coordinate. Given the Lagrangian above, the right side of the equation for each generalized coordinate becomes,

$$\frac{d}{dt} \left(\frac{\partial}{\partial \dot{x}} L \right) - \frac{\partial}{\partial x} L = m_1\ddot{x} + m_{2x}[\ddot{x} - p \cos(\phi + i_p)\ddot{\phi} - l_{ac} \cos(\theta)\ddot{\theta} + p \sin(\phi + i_p)\dot{\phi}^2 + l_{ac} \sin(\theta)\dot{\theta}^2] \quad (4.26)$$

$$\frac{d}{dt} \left(\frac{\partial L}{\partial \dot{y}} \right) - \frac{\partial L}{\partial y} = m_1 [\ddot{y} + g] + m_2 g + m_{2y} [\ddot{y} - p \sin(\phi + i_p) \ddot{\phi} - l_{ac} \sin(\theta) \ddot{\theta} - p \cos(\phi + i_p) \dot{\phi}^2 - l_{ac} \cos(\theta) \dot{\theta}^2] \quad (4.27)$$

$$\begin{aligned} \frac{d}{dt} \left(\frac{\partial L}{\partial \dot{\phi}} \right) - \frac{\partial L}{\partial \phi} = & J_1 \ddot{\phi} - m_2 g p \sin(\phi + i_p) + m_{2x} [-p \cos(\phi + i_p) \ddot{x} + p^2 \cos(\phi + i_p)^2 \ddot{\phi} + \\ & l_{ac} p \cos(\phi + i_p) \cos(\theta) \ddot{\theta} - p^2 \cos(\phi + i_p) \sin(\phi + i_p) \dot{\phi}^2 - l_{ac} p \cos(\phi + i_p) \sin(\theta) \dot{\theta}^2] + \\ & m_{2y} [-p \sin(\phi + i_p) \ddot{y} + p^2 \sin(\phi + i_p)^2 \ddot{\phi} + l_{ac} p \sin(\phi + i_p) \sin(\theta) \ddot{\theta} + p^2 \cos(\phi + \\ & i_p) \sin(\phi + i_p) \dot{\phi}^2 + l_{ac} p \sin(\phi + i_p) \cos(\theta) \dot{\theta}^2] \end{aligned} \quad (4.28)$$

$$\begin{aligned} \frac{d}{dt} \left(\frac{\partial L}{\partial \dot{\theta}} \right) - \frac{\partial L}{\partial \theta} = & -m_2 g l_{ac} \sin \theta + m_{2x} [-l_{ac} \cos(\theta) \ddot{x} + l_{ac} p \cos(\phi + i_p) \cos(\theta) \ddot{\phi} + \\ & l_{ac}^2 \cos(\theta)^2 \ddot{\theta} - l_{ac} p \sin(\phi + i_p) \cos(\theta) \dot{\phi}^2 - l_{ac}^2 \cos \theta \sin \theta \dot{\theta}^2] + m_{2y} [-l_{ac} \sin(\theta) \ddot{y} + \\ & l_{ac} p \sin(\phi + i_p) \sin(\theta) \ddot{\phi} - l_{ac}^2 \cos(\theta)^2 \ddot{\theta} + l_{ac} p \cos(\phi + i_p) \sin(\theta) \dot{\phi}^2 + l_{ac}^2 \cos \theta \sin \theta \dot{\theta}^2] \end{aligned} \quad (4.29)$$

An important note on these equations is the added complexity due to the “apparent mass” effects. Without separate “apparent masses” the equations are much simpler and calculation time is reduced significantly. In section 5.1.4 the differences between the fully modeled solution derived in this section and one assuming no “apparent mass” effects, as well as its effect on the resulting simulation and dynamic response, are discussed.

To determine the virtual forces, Q, in the system, the generalized force equation

$$Q_i = F_j \frac{\partial r_j}{\partial q_i} \quad (4.30)$$

is used, where j is equal to the number of forces acting on the system. In this system they consist of wing lift, wing drag, fuselage drag, and thrust, labelled as L, D_w, D_f, and T, respectively. The variable r represents the position of the related force, and in this system each one will be labeled as 1 for the fuselage, 2 for the wing, or T for the motor. Writing it all out the system becomes

$$Q_x = F_L \frac{\partial r_2}{\partial q_x} + F_{Dw} \frac{\partial r_2}{\partial q_x} + F_{Df} \frac{\partial r_1}{\partial q_x} + F_T \frac{\partial r_T}{\partial q_x} \quad (4.31)$$

$$Q_y = F_L \frac{\partial r_2}{\partial q_y} + F_{Dw} \frac{\partial r_2}{\partial q_y} + F_{Df} \frac{\partial r_1}{\partial q_y} + F_T \frac{\partial r_T}{\partial q_y} \quad (4.32)$$

$$Q_\phi = F_L \frac{\partial r_2}{\partial q_\phi} + F_{Dw} \frac{\partial r_2}{\partial q_\phi} + F_{Df} \frac{\partial r_1}{\partial q_\phi} + F_T \frac{\partial r_T}{\partial q_\phi} \quad (4.33)$$

$$Q_\theta = F_L \frac{\partial r_2}{\partial q_\theta} + F_{Dw} \frac{\partial r_2}{\partial q_\theta} + F_{Df} \frac{\partial r_1}{\partial q_\theta} + F_T \frac{\partial r_T}{\partial q_\theta} \quad (4.34)$$

The position of each component where the forces act will be described in terms of a separate reference coordinate system, where \hat{i} represents horizontal direction and \hat{j} represents vertical direction. The three unique positions are described as follows,

$$r_1 = x \hat{i} + y \hat{j} \quad (4.35)$$

$$r_2 = (x - p \sin(\phi + i_p) - l_{ac} \sin \theta) \hat{i} + (y + p \cos(\phi + i_p) + l_{ac} \cos \theta) \hat{j} \quad (4.36)$$

$$r_T = (x - l_T \sin \phi) \hat{i} + (y + l_T \cos \phi) \hat{j} \quad (4.37)$$

Note, r_1 and r_2 are equivalent to the definitions set by equations 4.10-13. Taking the partial derivatives of r_1 , r_2 , and r_T with respect to x , y , ϕ , and θ , yields the following 12 results, which are known as variations [25].

$$\frac{\partial r_1}{\partial q_x} = 1 \hat{i} + 0 \hat{j} \quad (4.38)$$

$$\frac{\partial r_1}{\partial q_y} = 0 \hat{i} + 1 \hat{j} \quad (4.39)$$

$$\frac{\partial r_1}{\partial q_\phi} = 0 \hat{i} + 0 \hat{j} \quad (4.40)$$

$$\frac{\partial r_1}{\partial q_\theta} = 0 \hat{i} + 0 \hat{j} \quad (4.41)$$

$$\frac{\partial r_2}{\partial q_x} = 1 \hat{i} + 0 \hat{j} \quad (4.42)$$

$$\frac{\partial r_2}{\partial q_y} = 0 \hat{i} + 1 \hat{j} \quad (4.43)$$

$$\frac{\partial r_2}{\partial q_\phi} = (-p \cos(\phi + i_p)) \hat{i} + (-p \sin(\phi + i_p)) \hat{j} \quad (4.44)$$

$$\frac{\partial r_2}{\partial q_\theta} = (-l_{ac} \cos \theta) \hat{i} + (-l_{ac} \sin \theta) \hat{j} \quad (4.45)$$

$$\frac{\partial r_T}{\partial q_x} = 1 \hat{i} + 0 \hat{j} \quad (4.46)$$

$$\frac{\partial r_T}{\partial q_y} = 0 \hat{i} + 1 \hat{j} \quad (4.47)$$

$$\frac{\partial r_T}{\partial q_\phi} = (-l_T \cos \phi) \hat{i} + (-l_T \sin \phi) \hat{j} \quad (4.48)$$

$$\frac{\partial r_T}{\partial q_\theta} = 0 \hat{i} + 0 \hat{j} \quad (4.49)$$

The forces are defined with both a magnitude and direction in the same \hat{i} and \hat{j} convention. This allows the horizontal and vertical components of each force to be easily compared to their respective variations. The forces, with direction components, are given as

$$F_L = -L(\sin(\gamma_2) \hat{i} + \cos(\gamma_2) \hat{j}) \quad (4.50)$$

$$F_{Dw} = D_w(-\cos(\gamma_2) \hat{i} - \sin(\gamma_2) \hat{j}) \quad (4.51)$$

$$F_{Df} = D_f(-\cos(\gamma_1) \hat{i} - \sin(\gamma_1) \hat{j}) \quad (4.52)$$

$$F_T = T(\cos \phi \hat{i} + \sin \phi \hat{j}) \quad (4.53)$$

Plugging equations 4.38-49 and equations 4.50-53 back into equations 4.31-34 and simplifying results in the following virtual force equations

$$Q_x = -L \sin \gamma_2 - D_w \cos \gamma_2 - D_f \cos \gamma_1 + T \cos \phi \quad (4.54)$$

$$Q_y = L \cos \gamma_2 - D_w \sin \gamma_2 - D_f \sin \gamma_1 + T \sin \phi \quad (4.55)$$

$$Q_\phi = Lp \sin(\gamma_2 - \phi - i_p) + D_w p \cos(\gamma_2 - \phi - i_p) - T l_T \quad (4.56)$$

$$Q_\theta = L l_{ac} \sin(\gamma_2 - \theta) + D_w l_{ac} \cos(\gamma_2 - \theta) \quad (4.57)$$

With the virtual forces defined, equations 4.54-57 and 4.26-29 can be plugged into equations 4.22-25. The result is a system of four equations with four variables and their derivatives.

Solving the system in terms of each acceleration term, or double-derivative, allows a useful form for solving both the steady-state, or static, condition, as well as the fully dynamic model. The unsolved equation for each generalized coordinate is written below in the order from top to bottom, x, y, ϕ , and θ .

$$\begin{aligned}
& -L \sin \gamma_2 - D_w \cos \gamma_2 - D_f \cos \gamma_1 + T \cos \phi = m_1 \ddot{x} + m_{2x} [\ddot{x} - p \cos(\phi + i_p) \ddot{\phi} - \\
& l_{ac} \cos(\theta) \ddot{\theta} + p \sin(\phi + i_p) \dot{\phi}^2 + l_{ac} \sin(\theta) \dot{\theta}^2] \quad (4.58)
\end{aligned}$$

$$\begin{aligned}
& L \cos \gamma_2 - D_w \sin \gamma_2 - D_f \sin \gamma_1 + T \sin \phi = m_1 [\ddot{y} + g] + m_2 g + m_{2y} [\ddot{y} - p \sin(\phi + i_p) \ddot{\phi} - \\
& l_{ac} \sin(\theta) \ddot{\theta} - p \cos(\phi + i_p) \dot{\phi}^2 - l_{ac} \cos(\theta) \dot{\theta}^2] \quad (4.59)
\end{aligned}$$

$$\begin{aligned}
& Lp \sin(\gamma_2 - \phi - i_p) + D_w p \cos(\gamma_2 - \phi - i_p) - T l_T = J_1 \ddot{\phi} - m_2 g p \sin(\phi + i_p) + \\
& m_{2x} [-p \cos(\phi + i_p) \ddot{x} + p^2 \cos(\phi + i_p)^2 \ddot{\phi} + l_{ac} p \cos(\phi + i_p) \cos(\theta) \ddot{\theta} - p^2 \cos(\phi + \\
& i_p) \sin(\phi + i_p) \dot{\phi}^2 - l_{ac} p \cos(\phi + i_p) \sin(\theta) \dot{\theta}^2] + m_{2y} [-p \sin(\phi + i_p) \ddot{y} + p^2 \sin(\phi + \\
& i_p)^2 \ddot{\phi} + l_{ac} p \sin(\phi + i_p) \sin(\theta) \ddot{\theta} + p^2 \cos(\phi + i_p) \sin(\phi + i_p) \dot{\phi}^2 + l_{ac} p \sin(\phi + \\
& i_p) \cos(\theta) \dot{\theta}^2] \quad (4.60)
\end{aligned}$$

$$\begin{aligned}
& L l_{ac} \sin(\gamma_2 - \theta) + D_w l_{ac} \cos(\gamma_2 - \theta) = -m_2 g l_{ac} \sin \theta + m_{2x} [-l_{ac} \cos(\theta) \ddot{x} + l_{ac} p \cos(\phi + \\
& i_p) \cos(\theta) \ddot{\phi} + l_{ac}^2 \cos(\theta)^2 \ddot{\theta} - l_{ac} p \sin(\phi + i_p) \cos(\theta) \dot{\phi}^2 - l_{ac}^2 \cos \theta \sin \theta \dot{\theta}^2] + \\
& m_{2y} [-l_{ac} \sin(\theta) \ddot{y} + l_{ac} p \sin(\phi + i_p) \sin(\theta) \ddot{\phi} - l_{ac}^2 \cos(\theta)^2 \ddot{\theta} + l_{ac} p \cos(\phi + i_p) \sin(\theta) \dot{\phi}^2 + \\
& l_{ac}^2 \cos \theta \sin \theta \dot{\theta}^2] \quad (4.61)
\end{aligned}$$

To solve this system of equations, substitution can be used to reduce the number of second order terms in each equation. Ultimately, each should contain a single second order term that can then be used in a differential equation solver. However, the process is not trivial and the equations become especially sizable.

Once solved, each of the forces can then be substituted with its full equation defined previously.

4.5. SIMULATION

Using the solution derived in the previous section, the simulation attempts to solve the system of differential equations numerically based on initial conditions and paraglider model parameters.

This requires solving the four Lagrange equations symbolically, such that the second-derivative coordinate terms are isolated for input into the differential equation solver. Since each equation in the system contains multiple second-order derivative terms substitution must be used to eliminate them until each equation has only one unique second-order term. Mathcad has a built-in symbolic solver that can be used to isolate for a particular variable, which can then be substituted. The process used to solve the systems is outlined by the following, using “ ϕ'' ” to denote second-derivative variables:

1. Isolate each equation for its second-derivative term
2. Insert x'' and y'' equations into ϕ'' and θ'' equations
3. Insert ϕ'' equation into θ''
4. Insert θ'' back into ϕ''
5. Insert ϕ'' and θ'' equations back into x'' and y'' equations

The resulting system should define four second-order derivatives in terms of the four generalized coordinates and their first-derivatives. However, Mathcad’s symbolic solver can only handle solutions of a certain size before failing to display, and due to the nature of substituting in whole equations the answers can be multiple times longer than the original. The solution can still be used, but for the purposes of this analysis the solution needs to be visible. To work around this issue, sections of the equations were replaced with function calls, reducing the overall length of each equation. The product is four solved Lagrangian equations containing seven supplementary equations. Additionally, by creating functions for the force variables, as well as their supporting flight path and angle of attack variables, the equations can be kept as short and simplified as possible. The structure of the solver sections of the simulation is presented by Figure 44. This structure is difficult to see looking at the code by itself, due to its scattered appearance, but this is vastly improved over an in-line option.

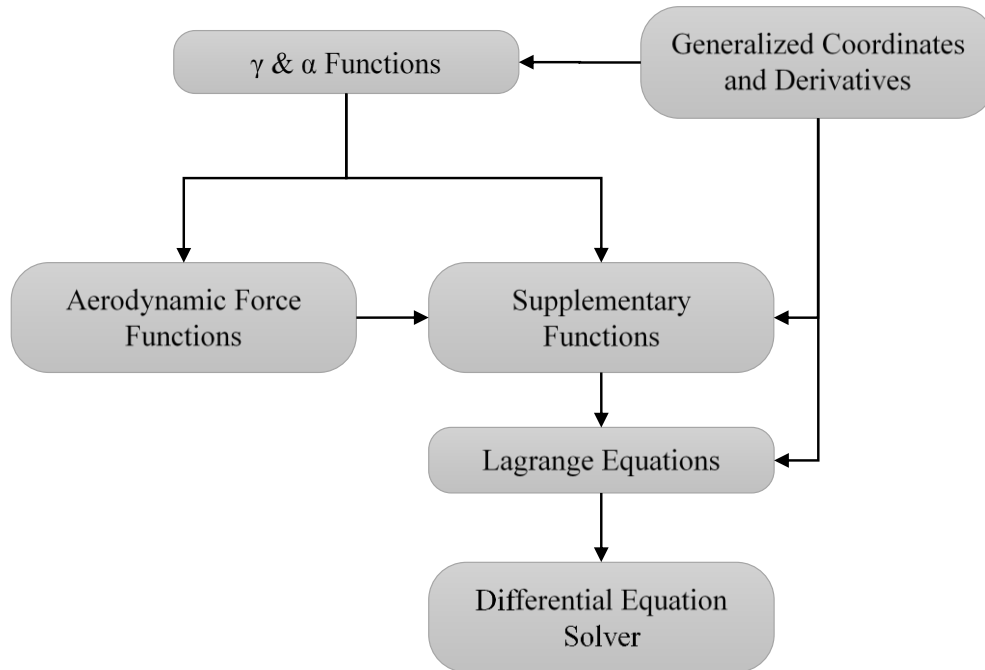


Figure 44: Simulation Flow Chart

Use of function calls to generic equations allow the same system to be used in multiple sections. In this simulation, a steady-state solution is found by setting the solved Lagrange equations equal to zero, and immediately following the same equations are used to numerically solve the system of differential equations, with the steady-state solution input as the initial conditions. The simulation uses a fixed step size Runge-Kutta numerical method. Mathcad also supports an adaptive step size solver but errors occurred for some analyses. The output of which is then used to calculate forces, angles, and velocities that are presented on graphs. It also creates an animation that follows the simulated vehicle, such that observations can be made on its behavior in motion. A preview of some outputs can be seen by Figure 45.

For a detailed breakdown of the code section-by-section and instructions on its use, refer to Appendix B.

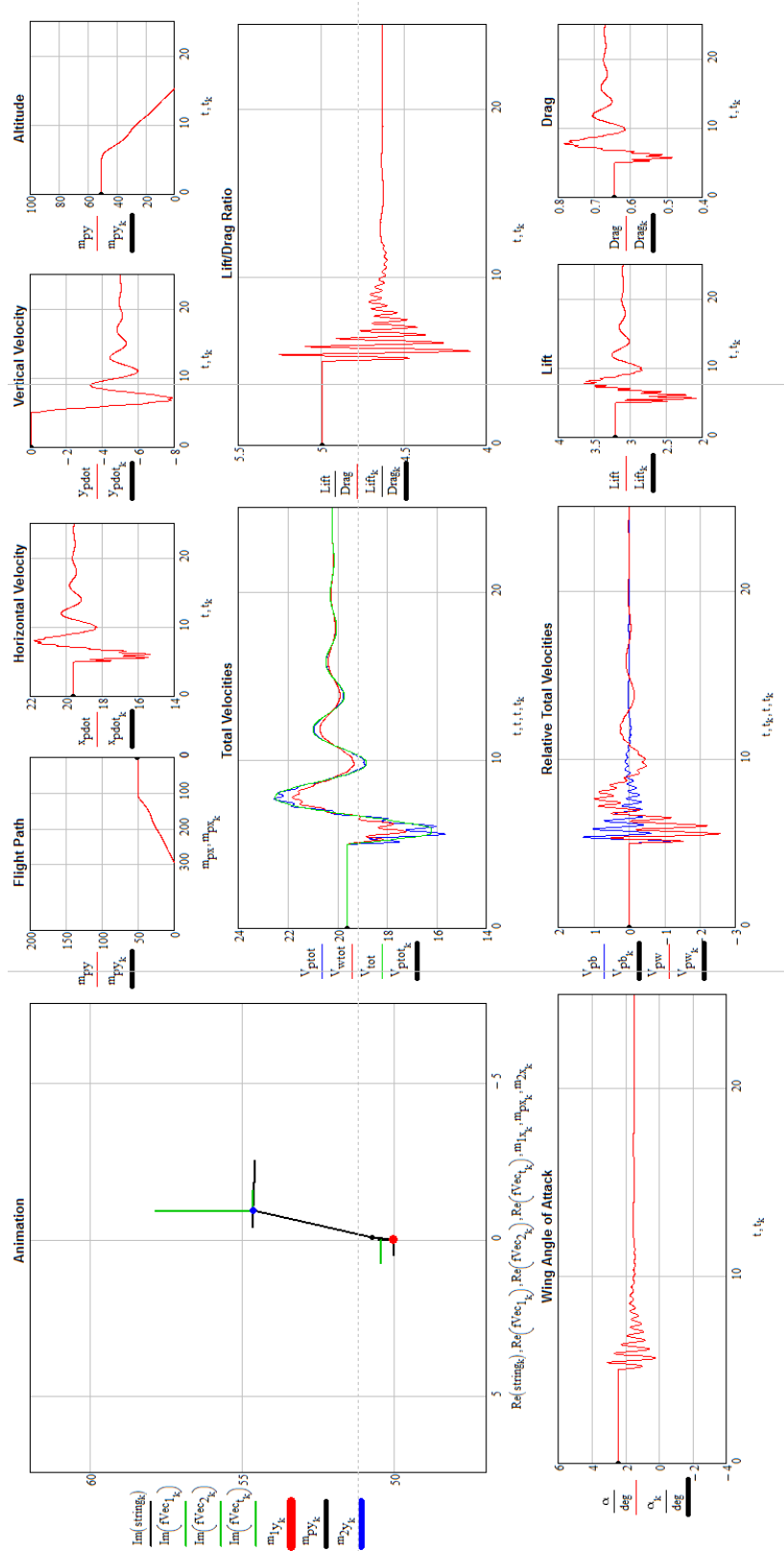


Figure 45: Sample of Some Simulation Outputs

4.6. VALIDATION

With the system defined and solved by the simulation, the validity of the model was determined through a comparison between data from Chambers and simulation results. In order to make an equivalent comparison between the two models, the assumptions from Chambers' studies had to be adapted to work with the geometry and functionality of the Lagrangian method. Without accounting for these assumptions the results would undoubtedly differ. Inevitably, the system could not be completely replicated as the rigid body presented by Chambers lacked the complexity of the Lagrangian method, which cannot be fully simplified for an equal comparison. Specifically, the freedom of both bodies to move independently of each other. Instead, the model is allowed to move with the additional degrees of freedom of the Lagrangian system but holds the same assumptions on constant angle of attack, and therefore constant lift and drag, as Chambers' model, as well as his equation for body drag.

The validation was made simpler by the fact that chambers included a detailed account of his paraglider's parameters in his research, along with ample flight data and simulation results for comparison. However, two parameters that remained vague were the line lengths between the leading and trailing edges and the connection point; although, not as important in his model where angle of attack is assumed constant, when converting to the Lagrangian setup this can make a large difference in the outcome of a case. In the strictest adaptation between Chambers' system and the Lagrangian system, the aerodynamic forces were made to evaluate based on the same functions defined by Chambers. This means regardless of rigging angle the lift and drag would be equivalent, so long as the same velocity was maintained. Likewise, the same was done for the fuselage drag. These functions could be replaced with the non-constant variable angle of attack analysis easily and those results will be shown as well.

Adapting the simulation code to match Chambers' data his constant C_L and C_D values needed to be calculated. His K_L value of 0.385 kg/m could then be input into the equation

$$\frac{1}{2}\rho v^2 S C_L = K_L v^2 \quad (4.62)$$

where air density, ρ , and wing area, S , are known and flight speed can be eliminated.

Rearranged, C_L becomes

$$C_L = \frac{2K_L}{\rho S} = 0.383 \quad (4.63)$$

C_D can be found using the drag equation, which takes the same form, using K_D of 0.107 kg/m

$$\frac{1}{2}\rho v^2 S C_D = K_D v^2 \quad (4.64)$$

$$C_D = \frac{2K_D}{\rho S} = 0.106 \quad (4.65)$$

The simulation was run against Chambers' calculated data for the case of a dynamic response to a step thrust change from 1.73 lb (7.7 N) to 0 lb. Two configurations of the simulation were run, a constant angle of attack assumption, "Lagrange-Constant AoA," and a variable angle of attack model, "Lagrange-Nicolaidis Polars." The constant angle of attack being more true to Chambers' system, but both versions used parameters given by Chambers in his research. The horizontal and vertical velocity comparisons are shown by Figure 46 and Figure 47, respectively. According to his paper, the simulation run by matched closely to experimental test results with his test vehicle.

Observing the dynamic response of Chambers' simulation and this paper's constant angle of attack equivalent, the different methods show similar behavior qualitatively, given slight differences in magnitude and offset. For vertical velocity, the two are offset by 1.3 ft/s and 1.0 ft/s with power on and off, respectively. The magnitude of the constant angle of attack method is

larger than Chambers' and slightly out of phase. The response is similar for the horizontal velocity but to a lesser degree. In the x-direction the offset is -0.47 ft/s and 0.63 ft/s power on and off, respectively.

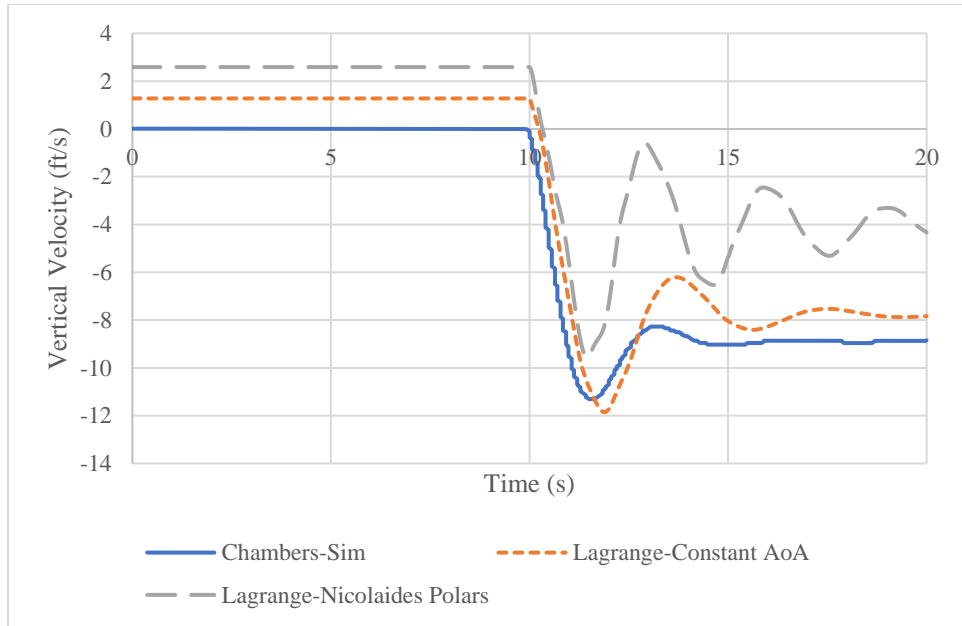


Figure 46: Vertical Velocity Response Comparison

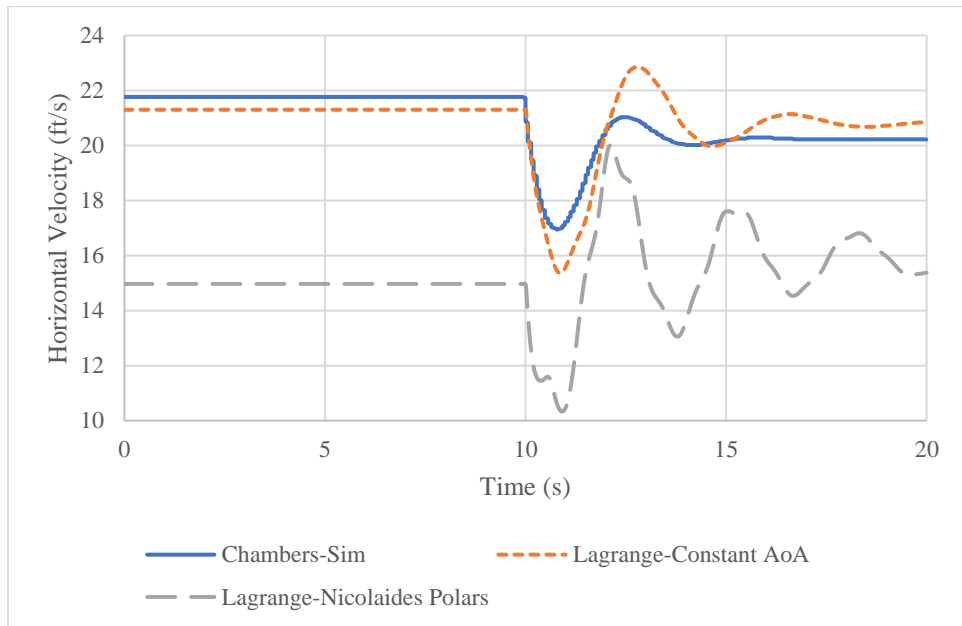


Figure 47: Horizontal Velocity Response Comparison

Simulations were also performed to obtain steady state climb rates. These were all done with the same parameters, while varying thrust for different rates. In addition to the three configurations compared previously, Chambers included experimental climb rates that will also be used for comparison. Figure 48 shows the four cases. The validation data, those directly from Chambers, only exist from 1.06 lb (4.7 N) to 2.1 lb (9.3 N). As such, the data from this research’s simulation will be compared only within this range as well.

The constant angle of attack method simulation results correspond closely to Chambers’ simulation data, with a small offset averaging 1.3 ft/s higher but similar slopes. At the lower values of thrust Chambers’ values tend to be closer to the experimental values; however, at 2.1 lb the difference between the constant angle of attack climb rate and experimental only differs by 0.23 ft/s.

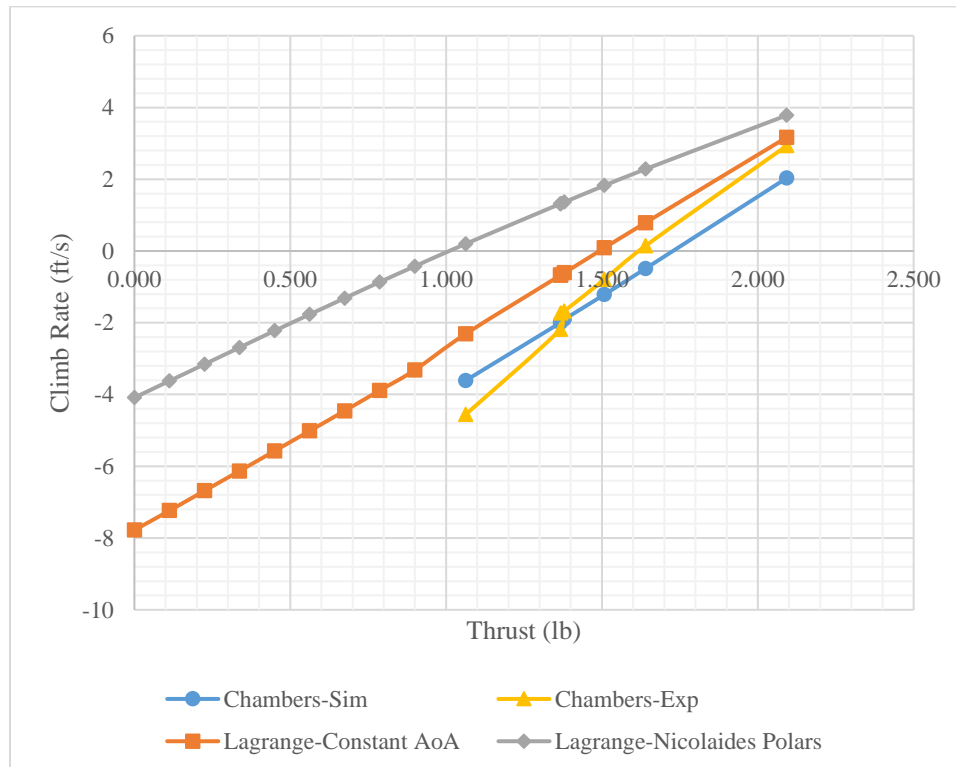


Figure 48: Steady State Climb Comparison

Given the small offsets and similar qualitative behavior, the results output from both simulations appears to model Chambers' physical system adequately. Perhaps the most likely reason for this small difference is the method by which the two systems are modeled. With the added flexibility of the Lagrangian system the thrust vector is allowed to move independently of the wing and aerodynamic forces. Chambers' simulation is allowed to rotate as well and the angle of its wing has no impact on the aerodynamic forces, with a constant angle of attack assumption. However, slight or dramatic, this would have an effect on the moment balance in his model and affect results differently than a multiple degree of freedom system.

In the variable angle of attack model the results are much farther off in terms of offset as well as oscillation magnitude and frequency; however, the general oscillatory response trend is the same. In addition to having the same inaccuracies as the constant angle of attack method, this study has additional inaccuracy of a variable angle of attack and the accompanying questionable performance polars. With a fixed angle of attack, the airfoil shape is irrelevant as it will create the same amount of lift and drag regardless of its orientation for a given velocity. Introducing a variable angle of attack requires using performance data that may not correlate to the physical model it is meant to represent. Consequently, performance will also change if the parafoil is set to a different rigging angle, which is not given by Chambers for his vehicle. Regardless, the results appear to match the other two simulations, which Chambers indicated aligned closely to his experimental results. While further validation would be ideal, this comparison between the simulation methods indicates the Lagrangian method is accurate enough for analysis and study.

A comparison with test flight data is also made in section 5.2.2.3 for the second test flight.

CHAPTER 5

RESULTS

5.1. SIMULATION ANALYSES

This section compares different parameters for paraglider design through the system simulation. Most test compare steady state climb rates or a step thrust input response, where the thrust input acts similarly to a stick-fixed response in a conventional aircraft. The steady state results are those that can be solved mathematically for initial conditions and results may vary when applying the same conditions for a dynamic response.

5.1.1. RIGGING ANGLE

Discussed in section 3.3, the rigging angle of the parafoil has a powerful effect on the performance and capabilities of the paraglider. Rigging angle being the zero-degree wing pitch incidence angle, defined in section 4.1.

5.1.1.1. EFFECT ON GLIDE PERFORMANCE

Setting the rigging angle will determine approximately where along the lift curve the parafoil will glide in a power-off condition. In section 2.5, the glide angle was shown to be dependent on the lift to drag ratio of the entire system, which requires velocity to be known. To estimate the glide angle equation 2.7 can be adjusted to only account for the drag of the parafoil and take the form

$$\gamma = \tan^{-1} \left(\frac{C_D}{C_L} \right) \quad (5.1)$$

Alternatively, the drag of the fuselage could still be included; however, the wing area and frontal area of the fuselage must be known. It would instead be

$$\gamma = \tan^{-1}\left(\frac{SC_{D_w} + AC_{D_f}}{SC_L}\right) \quad (5.2)$$

where A is the frontal area of the fuselage. The wing drag only assumption will be used to keep the analysis more general. Substituting equation 5.1, where C_D is in the negative direction for this system, into equation 4.6 and recognizing that C_L and C_D are functions of angle of attack the equation becomes

$$\alpha = i_w + \tan^{-1}\left(\frac{C_D(\alpha)}{C_L(\alpha)}\right) \quad (5.3)$$

Using a numeric solver with parafoil performance data, the power-off glide angle of attack for the paraglider can be determined for any rigging angle, i_w . For Nicolaides' parafoil the results can be seen by Figure 49, Figure 50, and Figure 51. Calculations were performed at each whole number rigging angle between -20° and -2° . In Figure 49 the resulting angle of attack and lift to drag ratio for each rigging angle can be seen. Alternatively, the results can be seen plotted against the performance data in Figure 50, where the orange dots represent the solutions from smallest, -20° , on the left to highest, -2° , on the right. The most efficient glide occurs at a rigging angle of -3° and 6.79° angle of attack, with the highest solvable solution at -1.25° . It should also be noted that multiple solutions can exist, but a proper initial guess should produce the most logical solution. Additionally, using the relation between the lift to drag ratio and flight path angle, the glide angle for Nicolaides' parafoil can be seen by Figure 51. The glide performance behaves as expected, with the shallowest angles occurring at angle of attack values corresponding to the highest lift to drag ratios and steepening as efficiency drops.

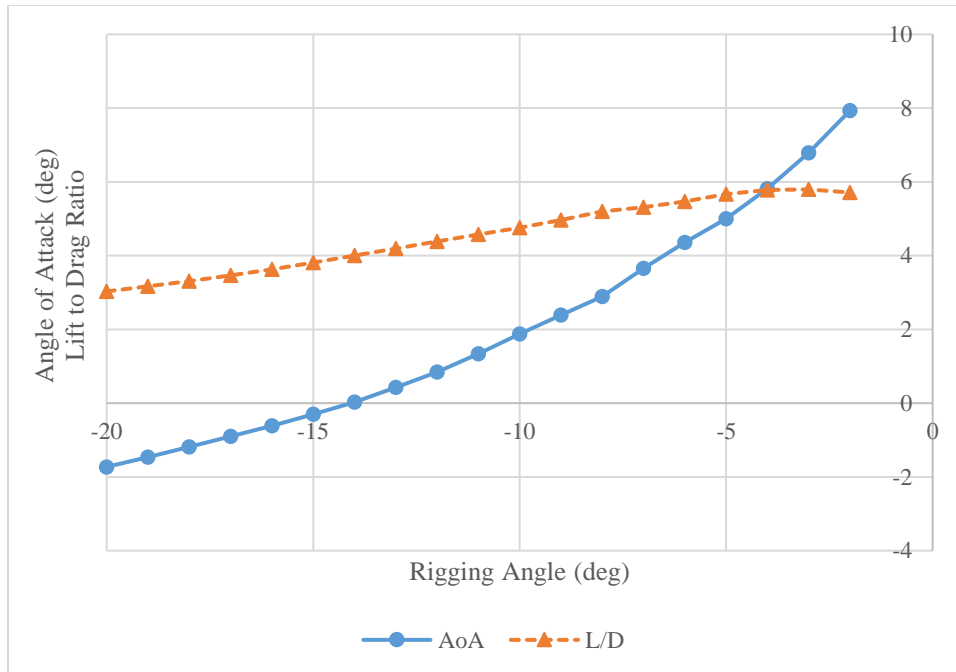


Figure 49: Rigging Angle Effect on Angle of Attack and Lift to Drag Ratio

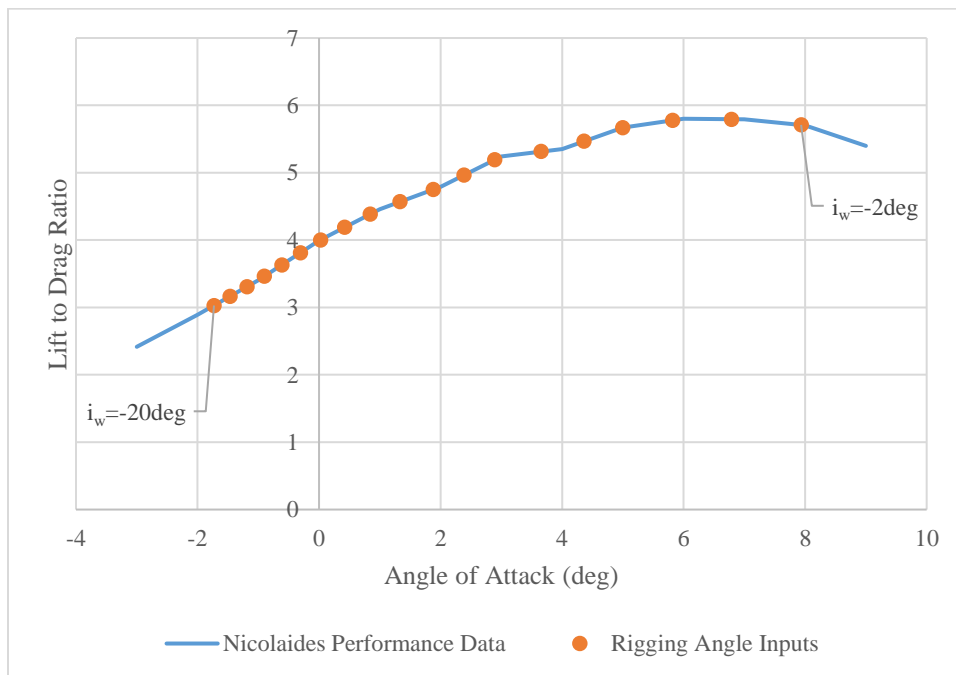


Figure 50: Relationship between Angle of Attack, Rigging Angle, and Lift to Drag Ratio

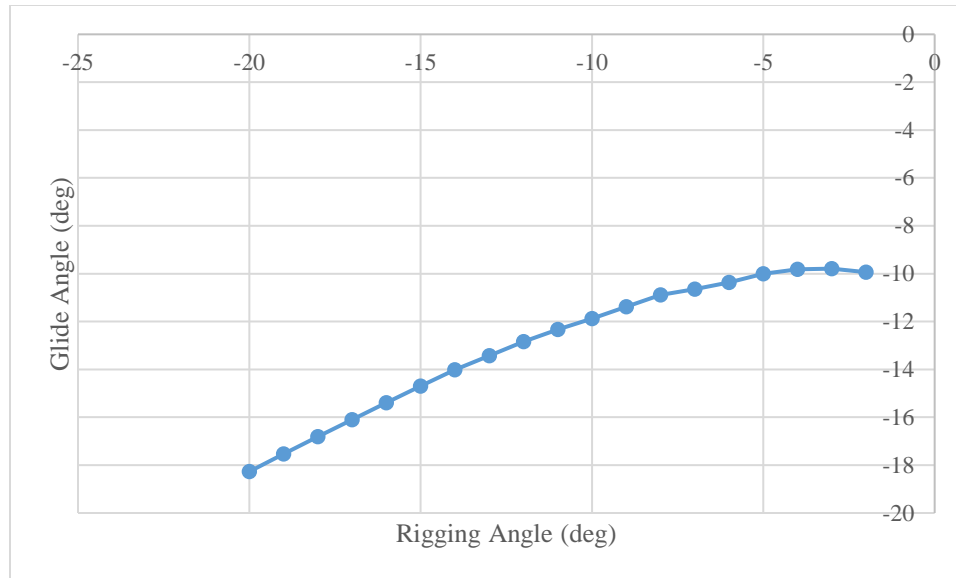


Figure 51: Glide Angle for Nicolaid's Parafoil with Changes in Rigging Angle

5.1.1.2. EFFECT ON THRUST CAPACITY & CLIMB

When thrust is applied the rigging angle plays another role in the behavior of a paraglider. As the thrust force pushes the fuselage it appears to pull the parafoil, causing it to pitch backwards. The angle of attack will grow with increased pitch based on the fixed geometry discussed in section 4.1. Setting the rigging angle lower allows the parafoil to maintain a smaller angle of attack when thrust is applied. In Figure 52 it can be seen that as rigging angle increases the resulting angle of attack for applied thrust rises greatly. Above -2.2° the parafoil is unable to handle either of the two thrust inputs. Unexpectedly, the rigging angle had little effect on the pitch angle, which remained within a one degree range at each thrust setting. The average pitch angles for 0, 0.75, and 1.5 pounds were -1.9° , 13.1° , and 27.6° , respectively. With a thrust increase one might assume an increase in velocity; however, the paraglider's total velocity is nearly equal, shown in Figure 53.

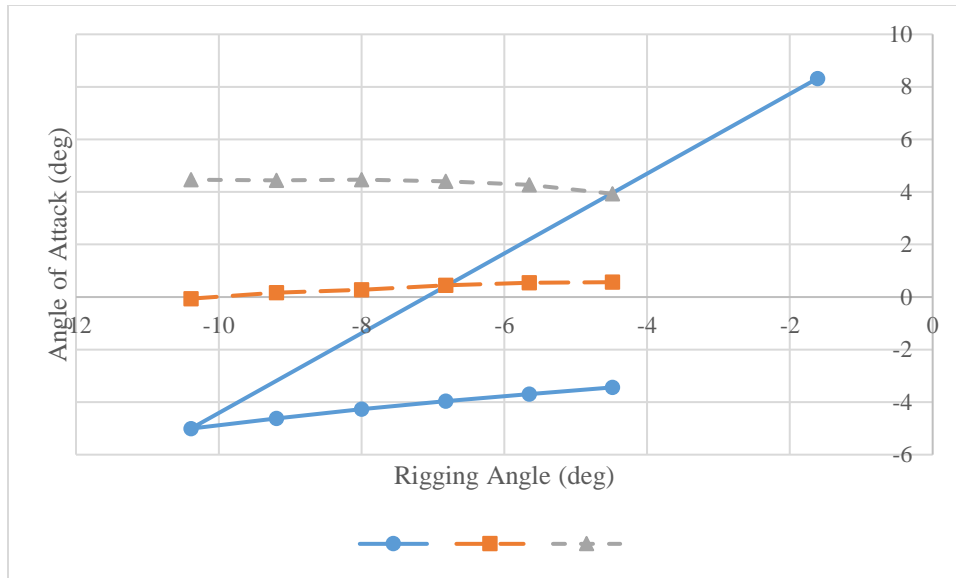


Figure 52: Rigging Angle Effect on Angle of Attack with Thrust Input

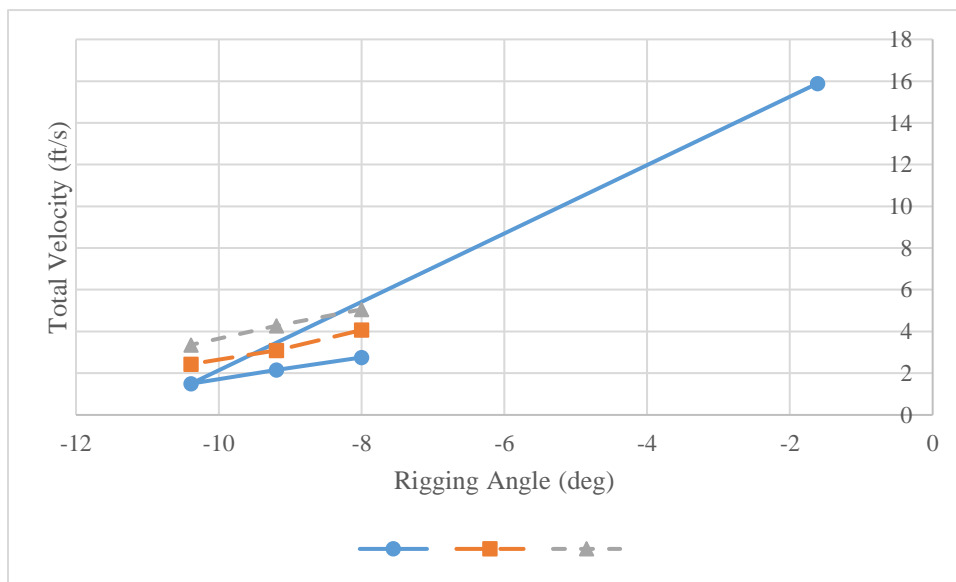


Figure 53: Rigging Angle Effect on Total Velocity with Thrust Input

With a larger operating range, a paraglider with a lower rigging angle is able to achieve greater climb rates. In Figure 54 the climb rate for three rigging angles has been calculated versus thrust input, where the end of each line indicates the maximum rate of climb and thrust. It should be noted that these values are for the steady state case and do not indicate if the dynamic system is capable of achieving the given configurations. The expanded performance of a lower angle configuration is counteracted by decreased efficiency in terms of power-off range and power-on

endurance. For a model representing the test vehicle, the thrust required for level flight changes from approximately 0.625 lb to 0.75 lb for rigging angles of -3.33° and -10.4° , respectively.

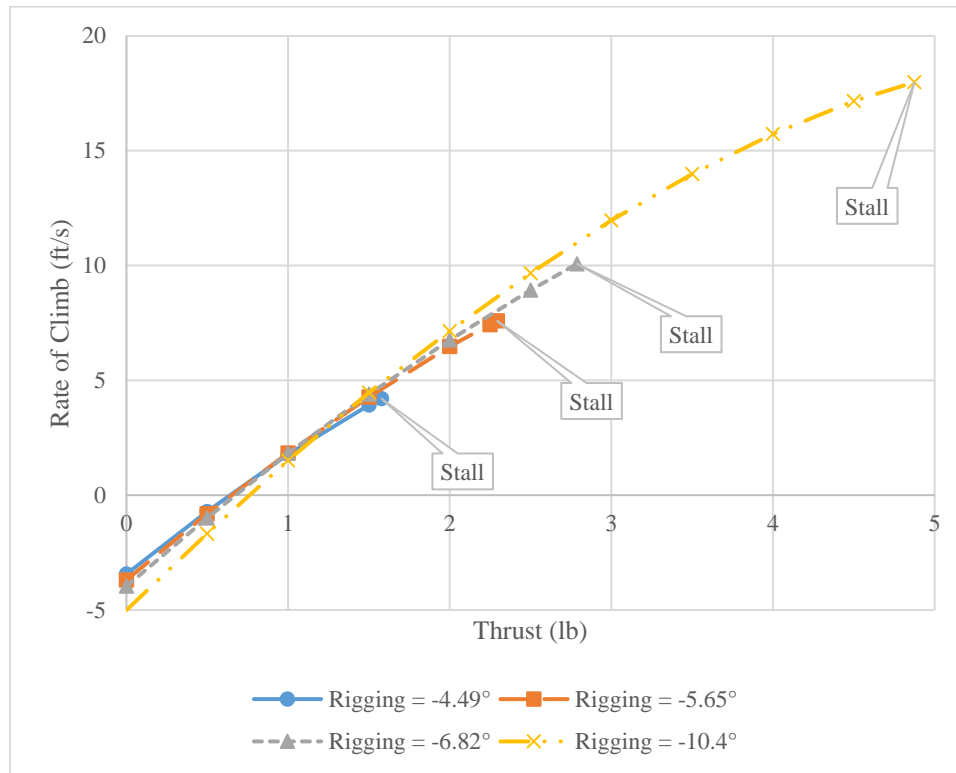


Figure 54: Rate of Climb for Thrust Input with Given Rigging Angle

It seems preferable in most cases to utilize a lower rigging angle for additional flexibility in operation but for optimal performance the rigging angle can be determined through data from Figure 55 and Figure 56. Figure 55 shows the climb rate given different rigging angles at stepped values of thrust. Similarly, Figure 56 depends on thrust and rigging angle but instead outputs flight path angle. This helps determine two design points, the optimum rigging angle for maximum level flight endurance and climb performance.

Using Figure 55 the best rigging angle for level flight can be determined by using the “Best Angle” line, which is simply the highest climb rate for that set of thrust data points, to estimate the angle that crosses the horizontal axis. With more data sets the angle can be more accurately approximated. Being the highest climb per thrust, the “Best Angle” line represents the highest

efficiency; therefore, where the “Best Angle” line crosses the axis is the most efficient level flight angle. This could be utilized in a model where high endurance is required. Alternatively, if the vehicle is designed to climb quickly the “Best Angle” line can be followed to the maximum thrust line, which is the maximum climb rate of the vehicle. Similar to conventional aircraft, paragliders will also have a best angle climb, which is the maximum amount of altitude per ground distance. To determine the best angle, Figure 56 can be used with its “Best Angle” line to determine the best climb angle for a given thrust.

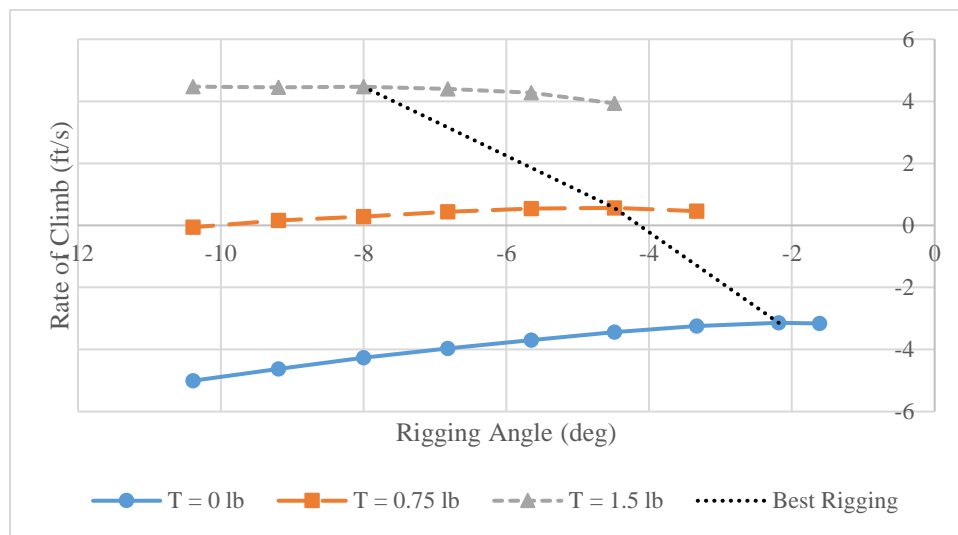


Figure 55: Climb Rate Based on Rigging Angle and Thrust

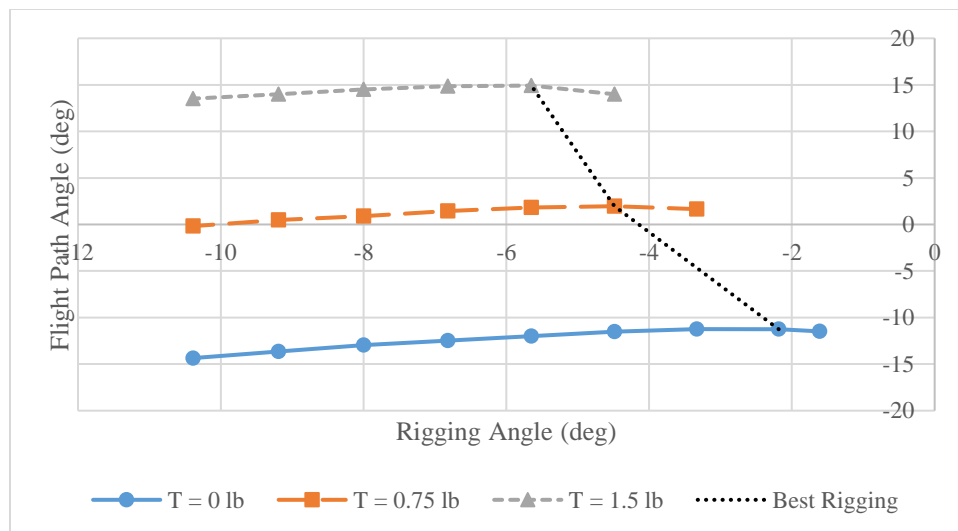


Figure 56: Flight Path Angle Based on Rigging Angle and Thrust

5.1.1.3. EFFECT ON DYNAMIC RESPONSE

Rigging angle also plays a role in dynamic stability. In response to a thrust input, a paraglider will exhibit motion similar to the phugoid mode. This is not surprising given thrust is a parafoil's primary source of pitch control, which is discussed in section 2.7. The simulation in Figure 57 shows the vehicle responding to a stepped thrust input from 0.75 lb to 0 lb at 5 seconds. The marked points indicate local minimums. The response period becomes shorter with shallower rigging angles, but the dampening is improved for steeper rigging angles.

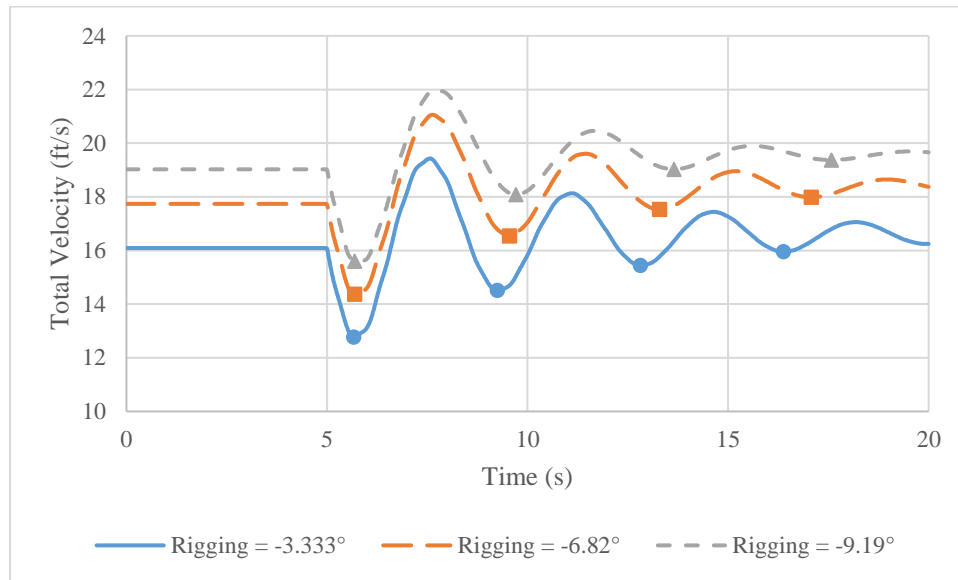


Figure 57: Dynamic Response for Step Thrust Input from 0.75 to 0 lb

Fitting an exponential trendline to the local minimums of the data allows for a quantitative description of the responses. This can be seen in Figure 58, where the total velocity of the paraglider is compared to the steady state total velocity for the new thrust input. Using equations 4.46-48 from [26], shown here as equations 5.4-6, provide the time and number of cycles for the responses to reach half of their original magnitude.

$$t_{halve} = \frac{0.693}{|\eta|} \quad (5.4)$$

$$N_{halve} = 0.110 \frac{|\omega|}{|\eta|} \quad (5.5)$$

where

$$\omega = \frac{2\pi}{\text{Period}} \quad (5.6)$$

and η comes from the exponential trendline equation

$$V = V_0 e^{\eta t} \quad (5.7)$$

Additionally, similar to equation 5.4, the time to reach 10% of the original value can be found by solving equation 5.7 for t with $V_0 = 0.10 V$, or,

$$t = \frac{\ln\left(\frac{V}{0.10V}\right)}{|\eta|} = \frac{2.30}{|\eta|} \quad (5.8)$$

The calculated values in Table 11 confirm the observations made earlier. With a rigging angle of -3.33° the paraglider will enter an oscillatory motion with a period of 3.57 seconds, dampen by 50% in 4.1 seconds, and converge to within 10% of the steady state velocity in 13.6 seconds. For the steeper angle of -9.19° the period is longer at 3.95 seconds; however, it is quicker to half its magnitude at only 2.75 seconds and approach 10% of the steady state velocity in 9.13 seconds.

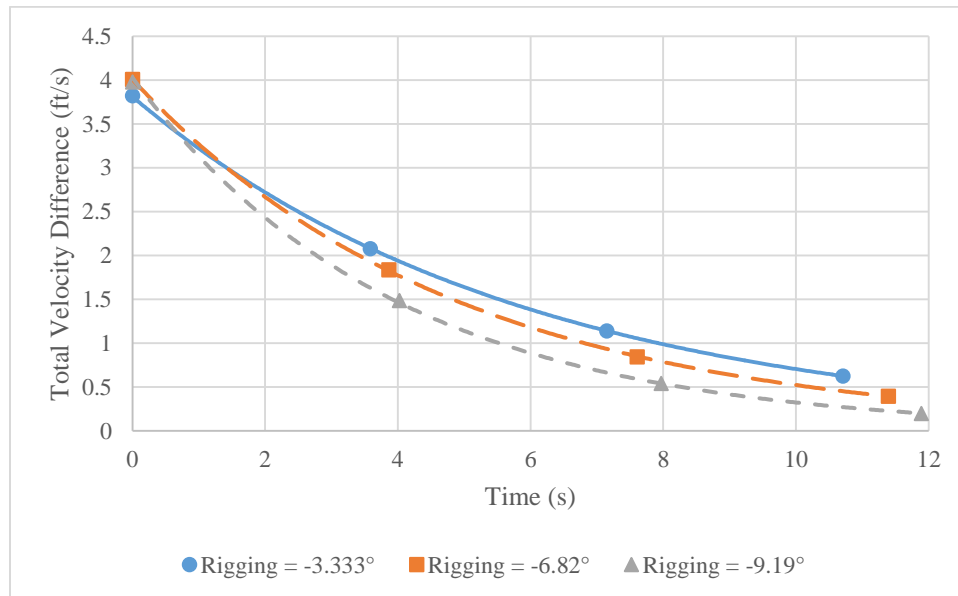


Figure 58: Analysis of Dynamic Response 0.75 to 0 lb

i_w	V_O	η	Period (s)	ω (rad/s)	$t_{1/2}$ (s)	$N_{1/2}$ (cycles)	$t_{1/10}$ (s)
-3.333°	3.81	-0.169	3.57	1.76	4.10	1.15	13.6
-6.82°	4.01	-0.204	3.80	1.65	3.40	0.89	11.3
-9.19°	4.03	-0.252	3.96	1.59	2.75	0.69	9.13

Table 11: Analysis of Dynamic Response 0.75 to 0 lb

5.1.2. WEIGHT & LOADING

This section discusses the effects of weight, and related wing loading, on paraglider performance through thrust capacity, climb rate, and dynamic response.

5.1.2.1. EFFECT ON THRUST CAPACITY & CLIMB

Based on the weight relation to glide performance discussed in section 2.5, the velocity of a paraglider in an unpowered glide is a function of weight or wing loading, with heavier fuselages descending faster than lighter fuselages. When thrust is applied to the paraglider the total velocity tends to decrease. If too much velocity is lost the wing will be unable to maintain enough lift for flight and the wing will stall; however, as the weight is increased there exists a point where the paraglider will have enough velocity to apply thrust without stalling. Then the behavior changes to a force balance as the wing and fuselage pitch further upwards, along with their associated aerodynamic and thrust forces. The additional thrust allowance allows for increased climb rates shown by Figure 59 to a point, where around 3.25 lb they begin to taper off. This is most likely due to the wing and fuselage reaching their limits on achievable pitch angles, shown in Figure 60.

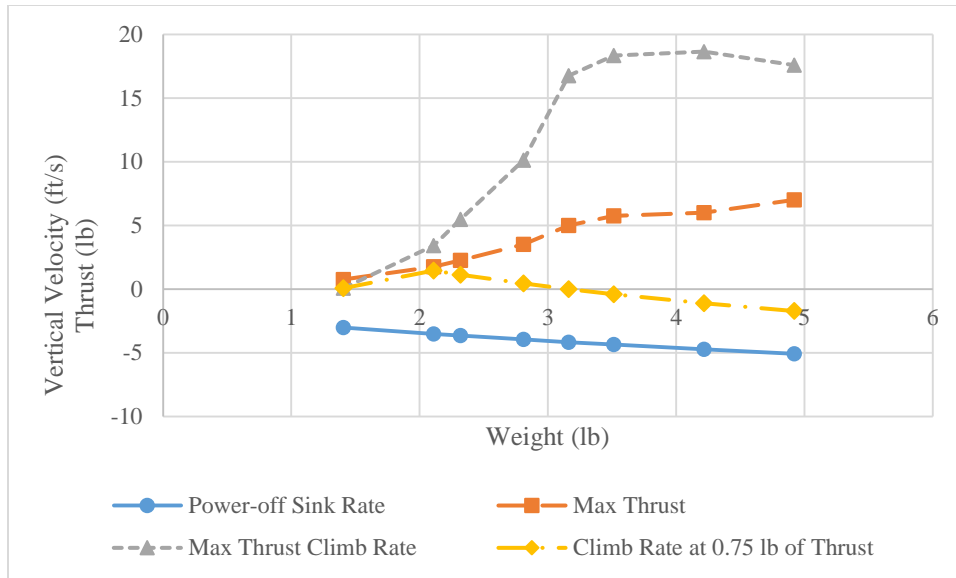


Figure 59: Vertical Velocities and Maximum Thrust Values with Various Fuselage Weights

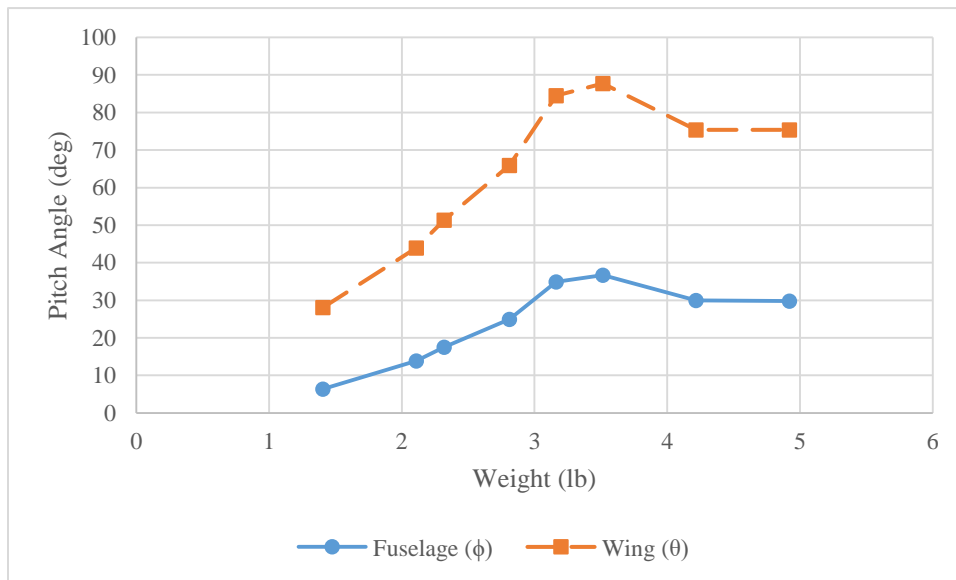


Figure 60: Fuselage and Wing Pitch Angles at Maximum Thrust by Weight

5.1.2.2. EFFECT ON DYNAMIC RESPONSE

The response behavior for changes in fuselage weight can be seen in Figure 61. Three cases for different weights were simulated: 100% of the test vehicle's fuselage weight, 75% of the fuselage weight, and 125% of the fuselage weight. Each case was started at a steady-state power-on

condition with 0.75 lb of thrust and then throttled off to 0 lb. As weight is reduced the response magnitude is greater and the period is shorter. This acts as expected since the lighter weight fuselage is rotated further forward or clockwise from its natural resting point than the heavier cases. This makes the return back to the equilibrium point more dramatic. Additionally, the total velocity difference between the power-on and power-off case is larger for the 75% weight fuselage at 1 ft/s, compared to 0.6 ft/s and 0.4 ft/s for the 100% and 125% weight fuselages, respectively.

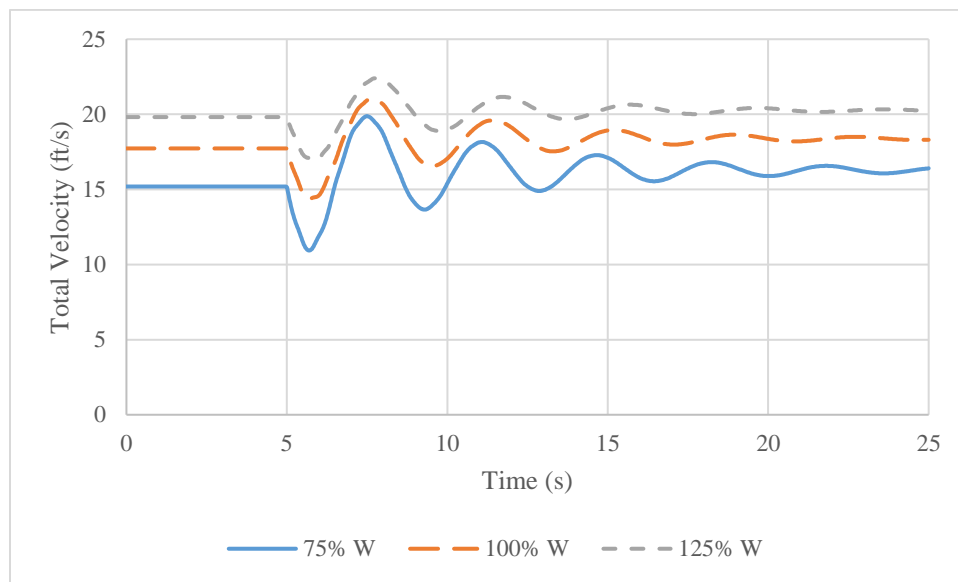


Figure 61: Dynamic Response for 0.75 to 0 lb of Thrust with Various Fuselage Weights

Discussed in section 2.5, the results of the simulation, shown in Table 12, verify that increasing weight will increase velocity and sink rate but maintain the same glide path angle. Based on the results for the weight simulations, the ideal weight would be 125% of the test vehicle, or 3.5 lb. As with any other analysis this will change from one vehicle to another; however, the trend indicates the ideal weight is just after the climb rate benefits begin to taper off. This would grant the greatest range of thrust magnitude and climb rate at minimum sink rate loss. Although, if the endurance is the main concern, a lower weight could provide adequate climb rates while using less power for level flight. The 0.75 lb thrust climb rate line in Figure 59 shows this efficiency.

	Weight (lb)	Glide Path Angle (deg)	Sink Rate (ft/s)
50%	1.41	-12.54	-3.01
75%	2.11	-12.49	-3.52
100%	2.81	-12.47	-3.97
125%	3.51	-12.45	-4.37
150%	4.22	-12.44	-4.74
175%	4.92	-12.44	-5.08

Table 12: Sink Rate and Glide Path for Differing Weights

5.1.3. CENTER OF GRAVITY

In the simulation, the center of gravity is determined by two variables, p and i_p , which are defined in section 4.2. In order to isolate changes to one variable, p will remain constant throughout this analysis as i_p is swept through several angles. As the center of gravity extends further in front of the hinged attachment point it will tend to rotate downwards as the mass naturally settles at the lowest point, shown by Figure 62. Conversely, if the center of gravity is placed behind the hinged attachment point the fuselage will rotate upwards. Consequently, the thrust line will also change orientation. This alters the paraglider's steady velocity and climb rate for a given thrust input.

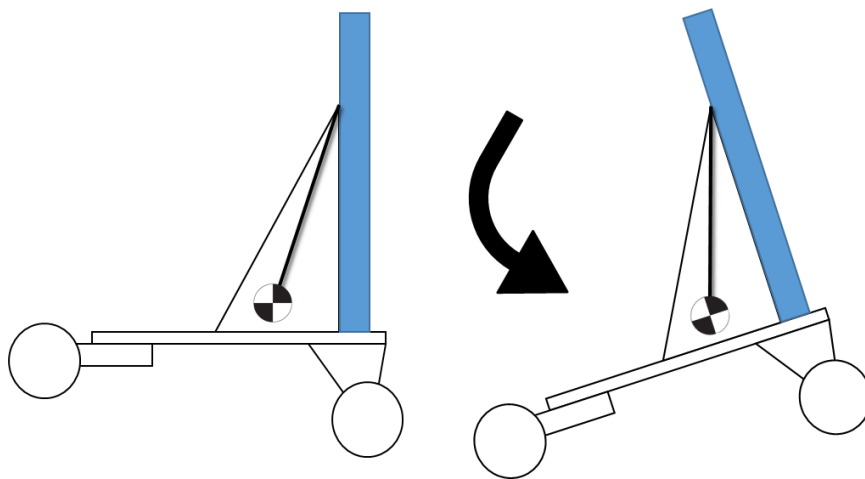


Figure 62: Center of Gravity Natural Pitch Behavior

5.1.3.1. EFFECT ON THRUST CAPACITY & CLIMB

There exists a correlation between center of gravity location and the performance capability of the paraglider. Figure 63 shows the behavior of the paraglider with a thrust input of 0.75 lb. As the center of gravity shifts aft the flight path angle and climb rate both increase, with diminishing returns. However, in Figure 64 the maximum thrust allowed and climb rate at maximum thrust are shown for changes in i_p . In terms of maximum thrust and climb it is less beneficial to shift the center of gravity far away from the attachment point. There is a maximum for thrust and climb rate slightly forward at 5° . This appears to be a balance between a positive vertical component of thrust versus pitch allowance. In other words, when the center of gravity is behind the attachment point and causes the fuselage to pitch back it increases the climb rate by using part of the thrust to supplement lift from the parafoil; however, as thrust is increased and the paraglider begins to pitch upwards the thrust is angled too high and causes the parafoil to stall earlier.

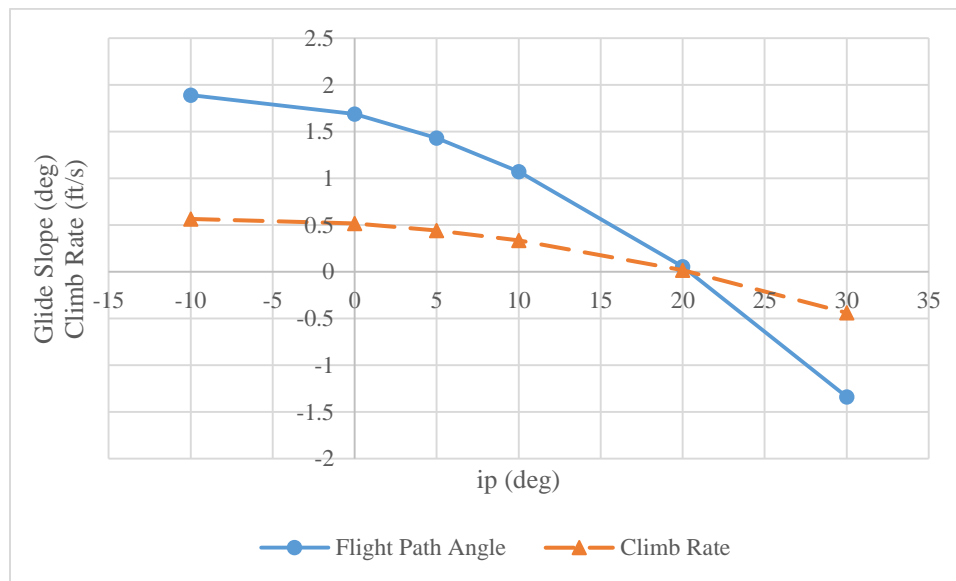


Figure 63: Glide Slope Angle and Climb Rate for Varying cg Positions at 0.75 lb of Thrust

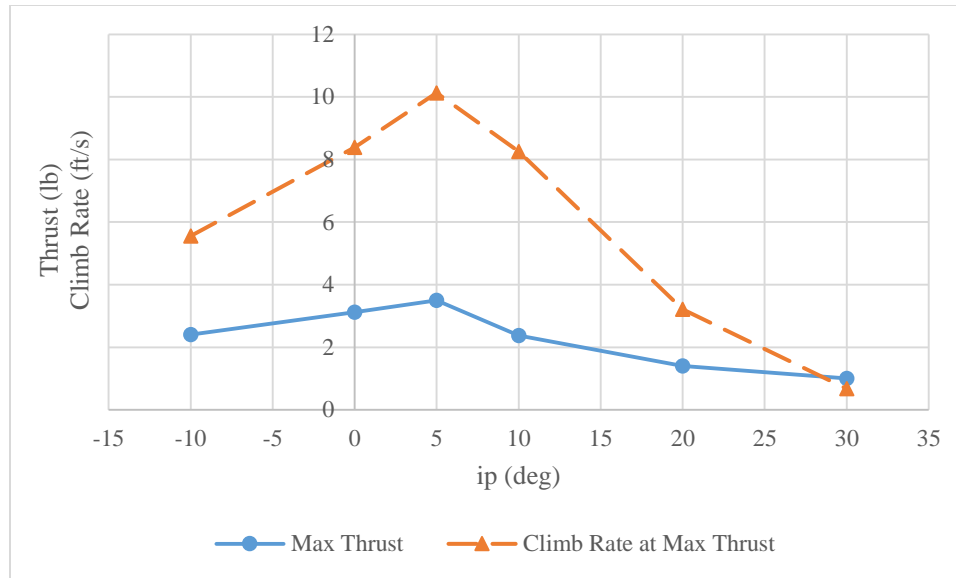


Figure 64: Maximum Thrust and Climb Rate at Max Thrust for Varying cg Positions

5.1.3.2. EFFECT ON DYNAMIC RESPONSE

To display the effect of fuselage pitch through cg location on dynamic response, two cases were analyzed for several angles. In the first case is a thrust step input from 0.75 lb to 0 lb, shown by Figure 65. The second reverses the first and starts with 0 lb and steps to 0.75 lb, shown by Figure 66. The two figures shown display three of the test angles but 0°, 5°, and 20° were also tested. The additional angles fall as expected in between the curves shown, and are not shown for clarity. In both cases, as the center of gravity was placed further ahead the response damped faster and had a slightly longer period than those behind it. This could be due to the overall change in velocity between the steady power-off and power-on states. By observing the first case, the velocity difference between the initial and final states is much smaller for the 30° angle curve than the -10° curve; however, the 20° would start closer than either of those.

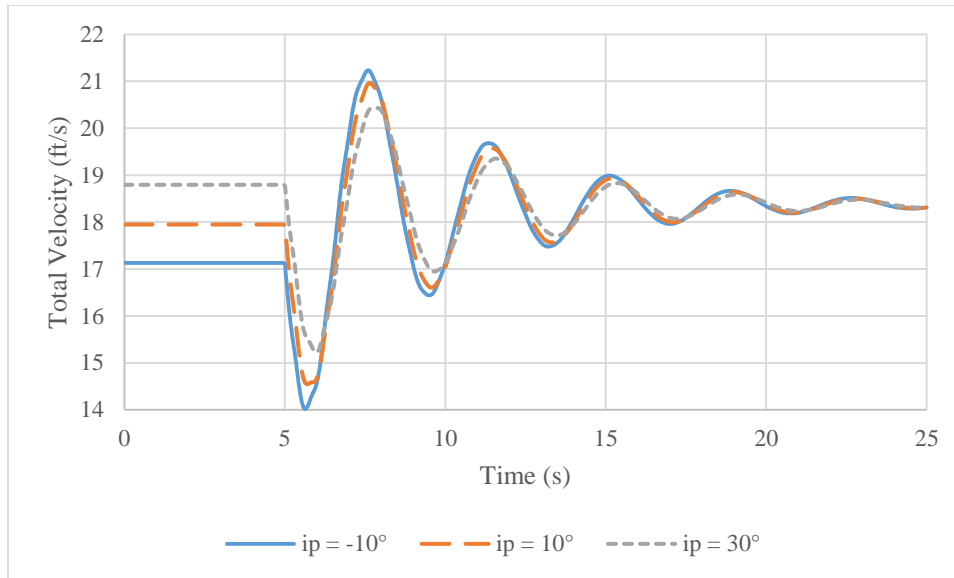


Figure 65: Dynamic Response for 0.75 to 0 lb of Thrust with Varying cg Location

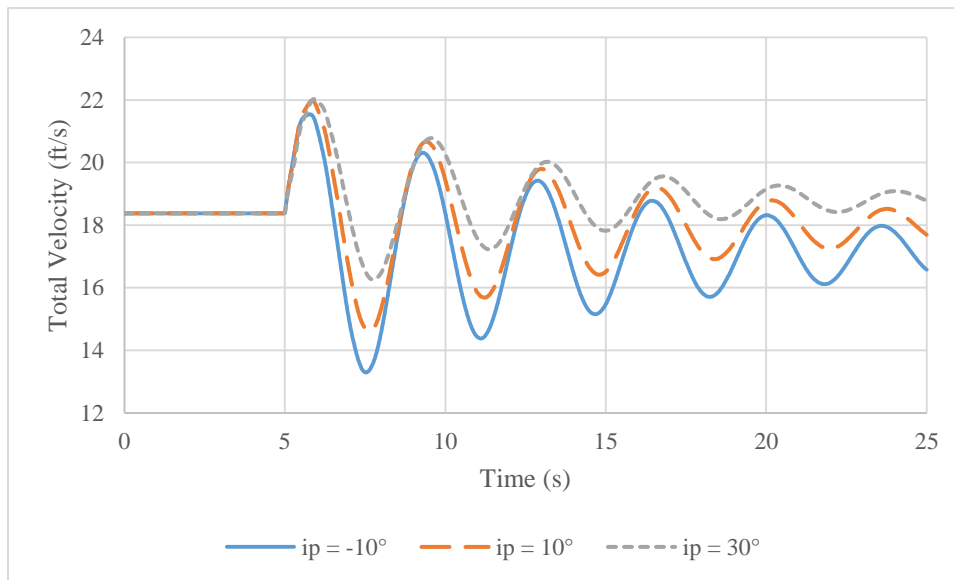


Figure 66: Dynamic Response for 0 to 0.75 lb of Thrust with Varying cg Location

5.1.1.4. “APPARENT MASS” EFFECTS

Comparing the effect of “apparent mass” approximations on the behavior of the system, two cases were run for a model representing the test vehicle. One case used the “apparent mass” calculations discussed in section 2.4 to set m_{2x} and m_{2y} to the increased theoretical mass. The

other disabled these calculations and instead set m_{2x} and m_{2y} back to the physical mass of the parafoil. Both cases show the response of the paraglider to a step thrust input of 0.75 lb to 0 lb at 5 seconds. Without the “apparent mass” terms the response damps slightly slower and oscillates faster. However, the general trend between the two is very close. Given that in an analysis of both cases the motion is represented with such similarity, omission of the “apparent mass” approximation terms is a viable and possibly appropriate option.

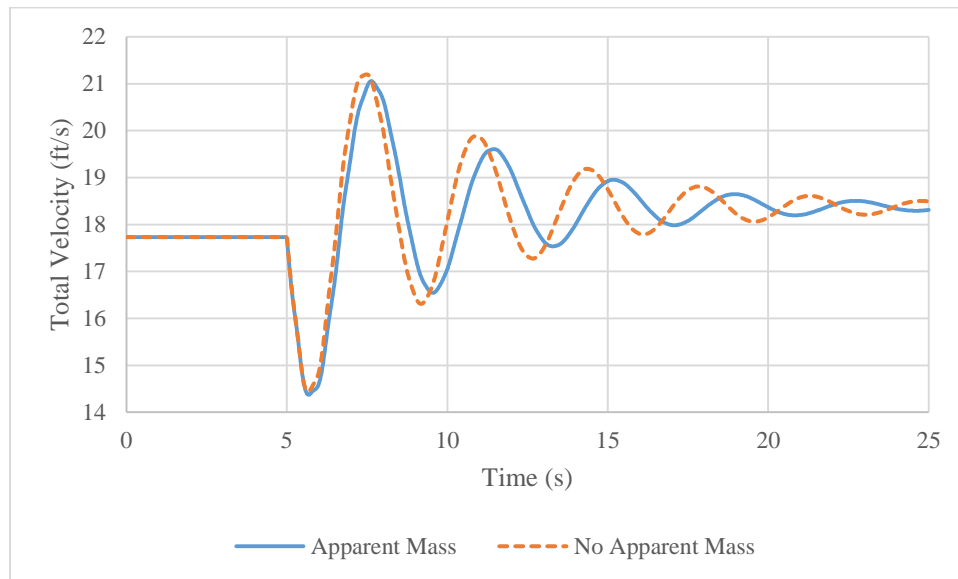


Figure 67: Dynamic Response for a Paraglider with and without “Apparent Mass”

Additionally, in contrast to the solution in section 4.4, the equations derived below are far simpler. The effect is combining the real mass and the two separate “apparent masses,” with each of their associated terms as well, into one term for the parafoil. Essentially, this does not remove any mathematical complexity in the system; however, the simplification to about half of the number of terms has a tremendous effect on reducing the computational difficulty. It should be noted that this comes from the perspective of the Mathcad 15 system and adaptations that must be made to handle large equations. Specifically, when using Mathcad’s symbolic solver to calculate derivatives or solve complex equations for a particular variable, if a result is too large the system will store its solution but it will not be displayed. This becomes an issue when trying to alter the

equations for use in a numerical solver. To circumvent this feature, equations can be simplified by extracting sections and assigning them to separate variables that can then be used functions. This workaround increases processing time with additional function calls, but also improves solution readability.

$$\frac{d}{dt} \left(\frac{\partial}{\partial \dot{x}} L \right) - \frac{\partial}{\partial x} L = m_1 \ddot{x} + m_2 [\ddot{x} - p \cos(\phi + i_p) \ddot{\phi} - l_{ac} \cos(\theta) \ddot{\theta} + p \sin(\phi + i_p) \dot{\phi}^2 + l_{ac} \sin(\theta) \dot{\theta}^2] \quad (5.9)$$

$$\frac{d}{dt} \left(\frac{\partial}{\partial \dot{y}} L \right) - \frac{\partial}{\partial y} L = m_1 [\ddot{y} + g] + m_2 [\ddot{y} - p \sin(\phi + i_p) \ddot{\phi} - l_{ac} \sin(\theta) \ddot{\theta} - p \cos(\phi + i_p) \dot{\phi}^2 - l_{ac} \cos(\theta) \dot{\theta}^2 + g] \quad (5.10)$$

$$\frac{d}{dt} \left(\frac{\partial}{\partial \dot{\phi}} L \right) - \frac{\partial}{\partial \phi} L = J_1 \ddot{\phi} + m_2 [-p \cos(\phi + i_p) \ddot{x} - p \sin(\phi + i_p) \ddot{y} + p^2 \ddot{\phi} + l_{ac} p \cos(\phi + i_p - \theta) \ddot{\theta} + l_{ac} p \sin(\phi + i_p - \theta) \dot{\theta}^2 - gp \sin(\phi + i_p)] \quad (5.11)$$

$$\frac{d}{dt} \left(\frac{\partial}{\partial \dot{\theta}} L \right) - \frac{\partial}{\partial \theta} L = m_2 [-l_{ac} \cos(\theta) \ddot{x} - l_{ac} \sin(\theta) \ddot{y} + l_{ac} p \cos(\phi + i_p - \theta) \ddot{\phi} + l_{ac}^2 \ddot{\theta} - l_{ac} p \sin(\phi + i_p - \theta) \dot{\phi}^2 - gl_{ac} \sin \theta] \quad (5.12)$$

5.2. EXPERIMENTS

5.2.1. FIRST FLIGHT TEST

The test vehicle showed a tendency to oscillate laterally in flight when presented with control input or small disturbances. This reflected pendulum-style motion, which was difficult to correct once initiated. There are two possible explanations for this behavior, wing arc and motor torque.

5.2.1.1. WING ARC

Observing the parafoil in flight reveals a highly arched structure resulting in excess anhedral, or negative dihedral, shown in Figure 68. As with conventional aircraft, this wing anhedral produces sensitive and unsteady lateral behavior. When the aircraft enters a sideslip the wings are affected differently from each other by the change in incoming air direction. With positive dihedral, the induced angle of attack on the lower wing is increased, while the higher wing's is reduced. This corrects the roll with a moment towards wing level. Figure 69 from Nelson displays dihedral effect graphically. With anhedral, the opposite is true and in sideslips the roll can cause instability by creating a roll moment diverging away from wings-level.



Figure 68: Parafoil Anhedral

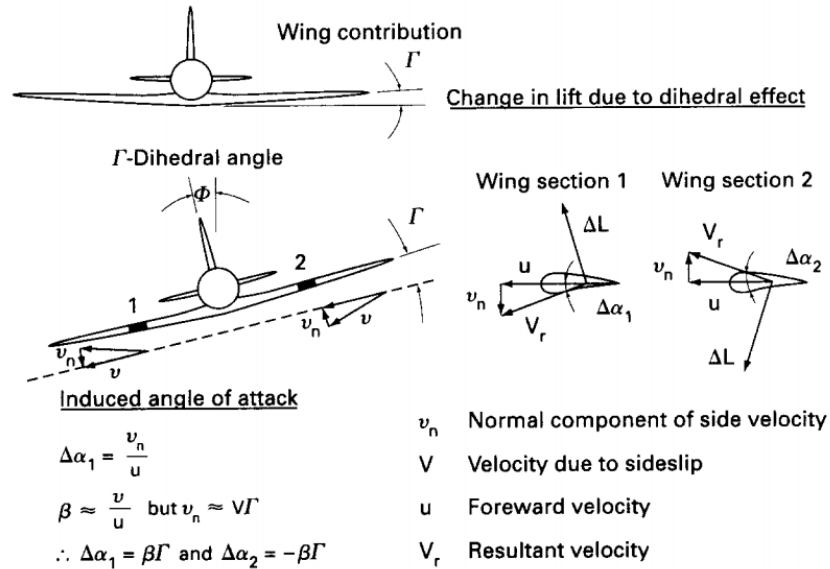


Figure 69: Dihedral Effect [26]

However, on high wing aircraft, where the center of gravity is located below the lifting surfaces, bank angles are countered by the weight of the fuselage in a pendulum-style motion, also referred to as keel effect. Anhedral is often added to heavy high wing aircraft to balance the large keel effect with reduced, or negative, dihedral effect. For paragliders, the keel effect is inherently large since the fuselage is located much farther away from the wing than in a conventional aircraft. As such, parafoils are able to contain additional anhedral without causing instability in the system.

5.2.1.2. TORQUE INDUCED ROTATION

It was observed from flight that the paraglider needed a large amount of lateral trim to fly straight when the power was applied. During ground and powerplant testing it was also seen that the motor would generate large amounts of torque. To test the possibility of torque induced rotation a simple experiment was conducted. The fuselage was hung with bungee cords and allowed to rotate when power was applied, shown in Figure 70. With the spring constant of the bungees

known, the displacement of the bungees could then be measured with the yellow ruler, translated into force, and balanced against the fuselage weight and torque.

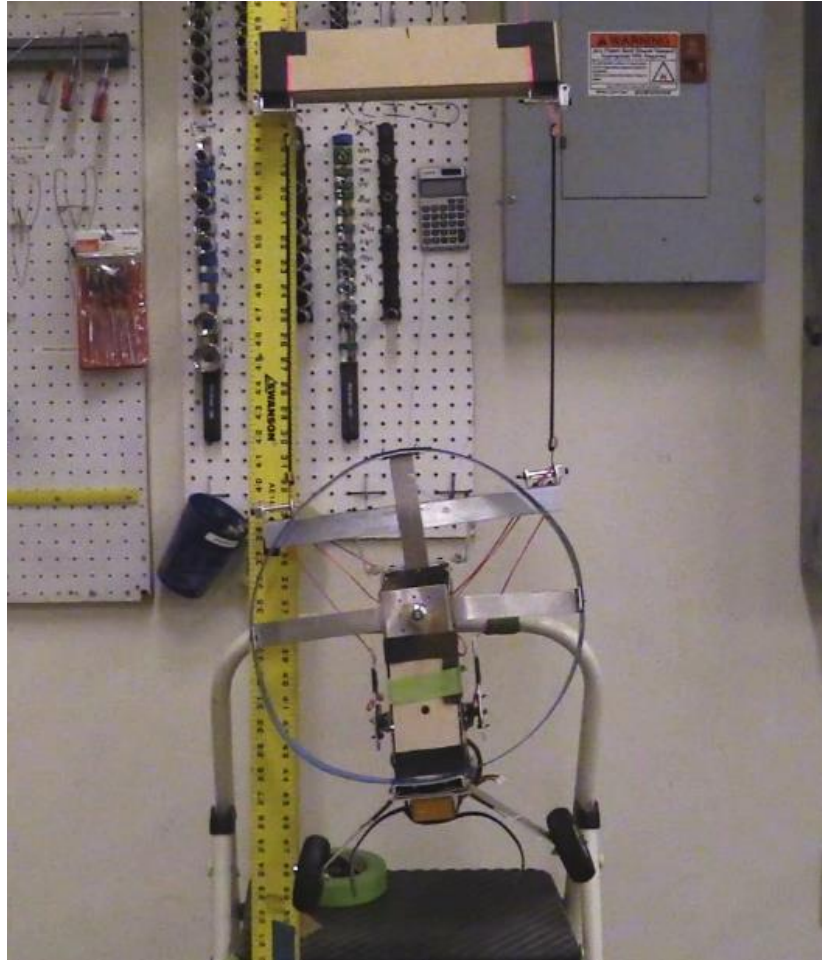


Figure 70: Bungees Under Load from Paraglider Torque

By balancing the moments in Figure 72 the torque applied to the system becomes

$$T = mgL \sin \phi + dk(\Delta x_2 - \Delta x_1) \quad (5.13)$$

where each Δx is the displacement that causes the spring force in the bungee and

$$\phi = \tan^{-1} \left(\frac{\Delta x_2 - \Delta x_1}{2d} \right) \quad (5.14)$$

This analysis also assumes the length d is constant for small rotations.

The test was run for 25%, 50%, and 75% throttle. At 25% the small displacement was difficult to distinguish from the movement of the fuselage so it was disregarded. For 50% and 75% throttle the measurement indicated about 0.125 and 0.375 inches of displacement, respectively. Plugging the displacement into the torque balance equation indicated about 0.65 and 2.0 lb-in of motor torque. Using electrical current draw data for the two throttle settings from powerplant testing and Figure 28, the predicted values for 50% and 75% throttle are 0.53 lb-in (6 N-cm) and 1.86 lb-in (21 N-cm). The experimental torque values correspond to the predicted values fairly well. Differences between the two are likely due to the coarse measurement during testing.

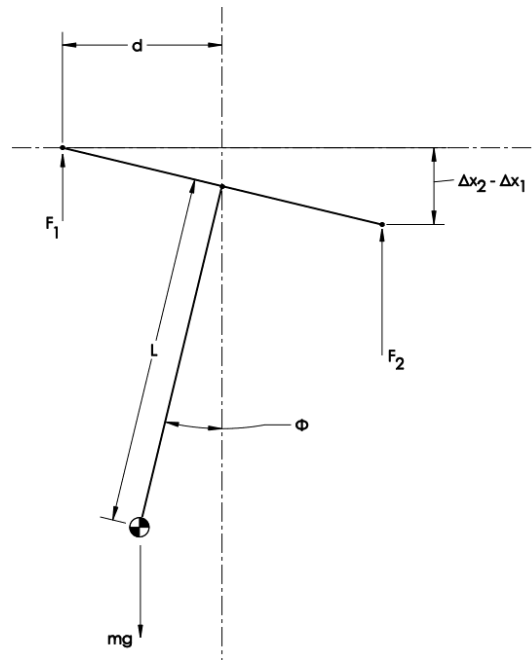


Figure 71: Lateral Paraglider System for Torque Analysis

To determine how much roll is produced by an applied torque, a balance of forces and moments can solve for the tension in each line and adjust the angle resulting angle accordingly. The system is shown by Figure 72. Unlike the previous analysis, the line tensions, T_p and T_s , act along the angles ϕ_p and ϕ_s , which are free to rotate. The balance of forces horizontally can be written

$$T_p \sin(\phi + \phi_p) + T_s \sin(\phi - \phi_s) = 0 \quad (5.15)$$

Similarly, the forces in the vertical direction can be written as

$$T_p \cos(\phi + \phi_p) + T_s \cos(\phi - \phi_s) = mg \quad (5.16)$$

Finally, balancing the moments about the center of gravity with the applied torque, τ , can be written

$$\tau + T_p \sin(\phi + \phi_p) h_p + T_s \sin(\phi - \phi_s) h_s = T_p \cos(\phi + \phi_p) x_p + T_s \cos(\phi - \phi_s) x_s \quad (5.17)$$

where

$$x_p = b \cos \phi + h \sin \phi \quad (5.18)$$

$$h_p = h \cos \phi - b \sin \phi \quad (5.19)$$

$$x_s = h \sin \phi - b \cos \phi \quad (5.20)$$

$$h_s = h \cos \phi + b \sin \phi \quad (5.21)$$

To finish describing the system an additional constraint is required. By setting line lengths and forcing the ends of those lines to be a certain distance apart, the system will act as though it were connected to the wing above; however, measurements for this are difficult to determine precisely. Test flight footage was analyzed and coarse measurements were gathered and plugged into the system. Each line was determined to be 3.2 ft long and separated by 30 inches at their ends.

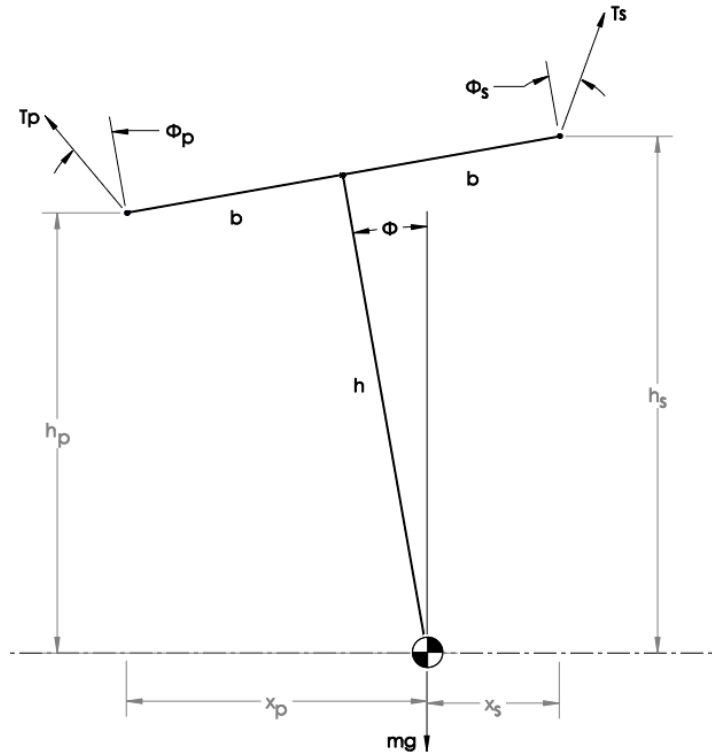


Figure 72: Free Body Diagram for Torque Rotation Analysis

Solving the system of equations places the rotation due to torque around 0.34° to 1.1° for 0.65 and 2.0 lb-in, respectively. This is a relatively small amount of rotation; however, in a system that is naturally prone to lateral instabilities through dihedral effect, it may not take a large angle to alter performance.

5.2.2. SECOND FLIGHT TEST

After the first test flight, the paraglider performance was observed and analyzed. Alterations to the vehicle focused on preventing roll oscillations, as that behavior dominated the previous attempt. The attachment bracket was widened, the tips of the parafoil were allowed to raise higher and reduce anhedral, and the rigging angle was decreased.

5.2.2.1. MOUNTING CONFIGURATION

Due to the flexible nature of a paraglider's design, there is a certain amount of twist between the wing and the fuselage that can occur during or after maneuvers and disturbances. Twist being the rotation about the yaw axis, rather than a rolling motion or the hinged longitudinal rotation.

When the fuselage rotates it also pulls the parafoil along with it; however, because the wing is the primary source of force, equilibrium is naturally restored so long as the wing is steady. Naturally twist stable, theoretically, there is a point of neutral stability when the parafoil lines attach to the same confluence point on the fuselage, instead of separate port and starboard confluence points.

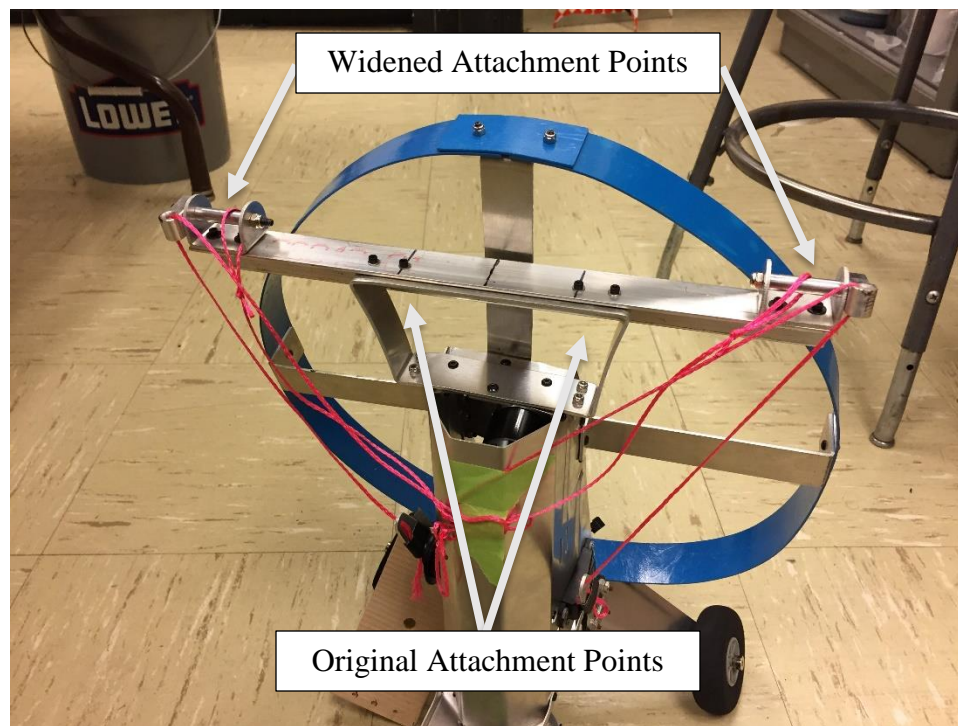


Figure 73: Modified Parafoil Attachment Bracket

Most, if not all, paragliders will be of a configuration where the lines from each side feed down separately to the fuselage. For the test vehicle, the attachment points can be seen in Figure 73. Alternatively, the connection between the parafoil and the fuselage can be viewed simply as a torsional spring, which acts about the yaw axis. Analogous of linear springs, torsional springs generate torque proportionally between a displacement and coefficient. As the name suggests, in

a linear spring the displacement is the change in linear distance, but torsional springs build torque based on angular distance. Similarly, the coefficient of the torsional spring is defined as the torque generated per radian. Specifically, the equation takes the form of,

$$\tau = -k_{\psi}\psi \quad (5.22)$$

where k_{ψ} is the torsional spring constant and ψ is the angle of rotation, used here for the yaw angle of the aircraft. However, more useful for this analysis is the traditional torque definition,

$$\tau = r \times F \quad (5.23)$$

where F is a force applied at a moment arm of r length. Taking the diagram shown by Figure 74 it can be seen that the torque generated by a torsional spring in the center will be equal to the product of the applied force, F_a , and the moment arm, b .

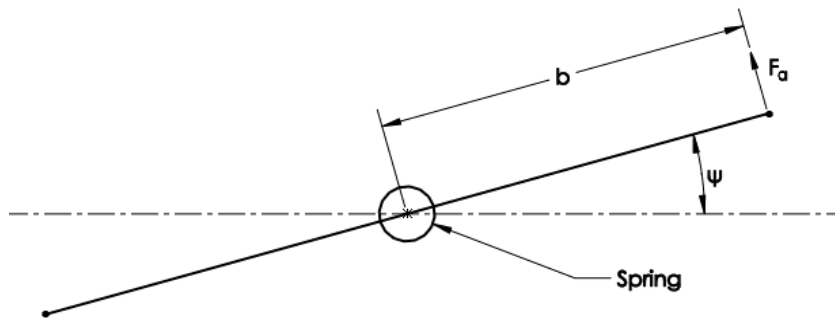


Figure 74: Applied Torque to Torsional Spring

In the longitudinal plane, the parafoil can be pictured as in Figure 75. The black lines represent the starboard lines and the blue lines represent the port lines. The sketch on the left shows the parafoil in normal flight with both lines running to the same point, on the two-dimensional plane. The right sketch shows how the parafoil would appear when the fuselage is yawed away from the centerline. The two lines shown are displayed alternatively as reference lines, which are defined by a common chordwise attachment point on the wing and each's confluence point on the fuselage. For accuracy in an analysis this would need to follow the direction of the actual rigging

line. They are separated since each confluence point moved opposite the other. The angle made by the reference line and vertical will be θ and the length of the reference line is l . F_t represents the tension force running into the rigging, and F_x is its x-component.

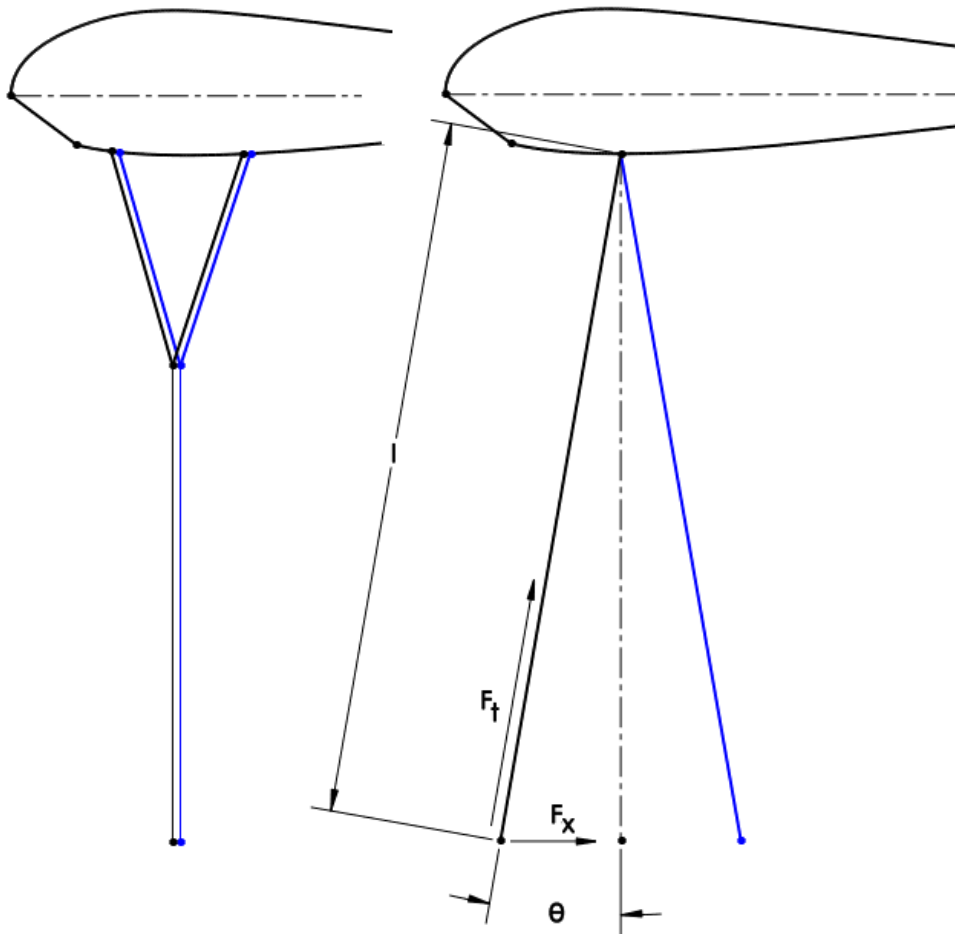


Figure 75: Separation of Rigging lines in Longitudinal Plane

Visualizing the paraglider in the yaw plane, the setup appears very similar to the torsional spring example in Figure 74. The paraglider adaptation is shown by Figure 76. Instead of a spring in the center responding to an applied torque, the figure shows the fuselage attachment bracket after a disturbance where it has yawed counterclockwise. The torsion now comes from the tension in the rigging lines pulling the fuselage back to the original dashed line equilibrium position. In this way it acts as the spring, resisting the angular displacement. It is uncertain whether the tension

force would act perpendicular to the fuselage as pictured in the diagram but it will be assumed the effects are negligible.

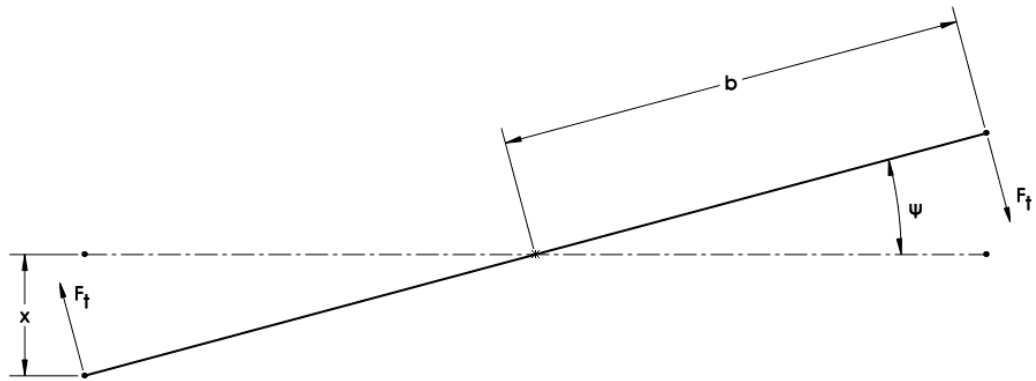


Figure 76: Yawing Paraglider Parafoil Attachment Bracket

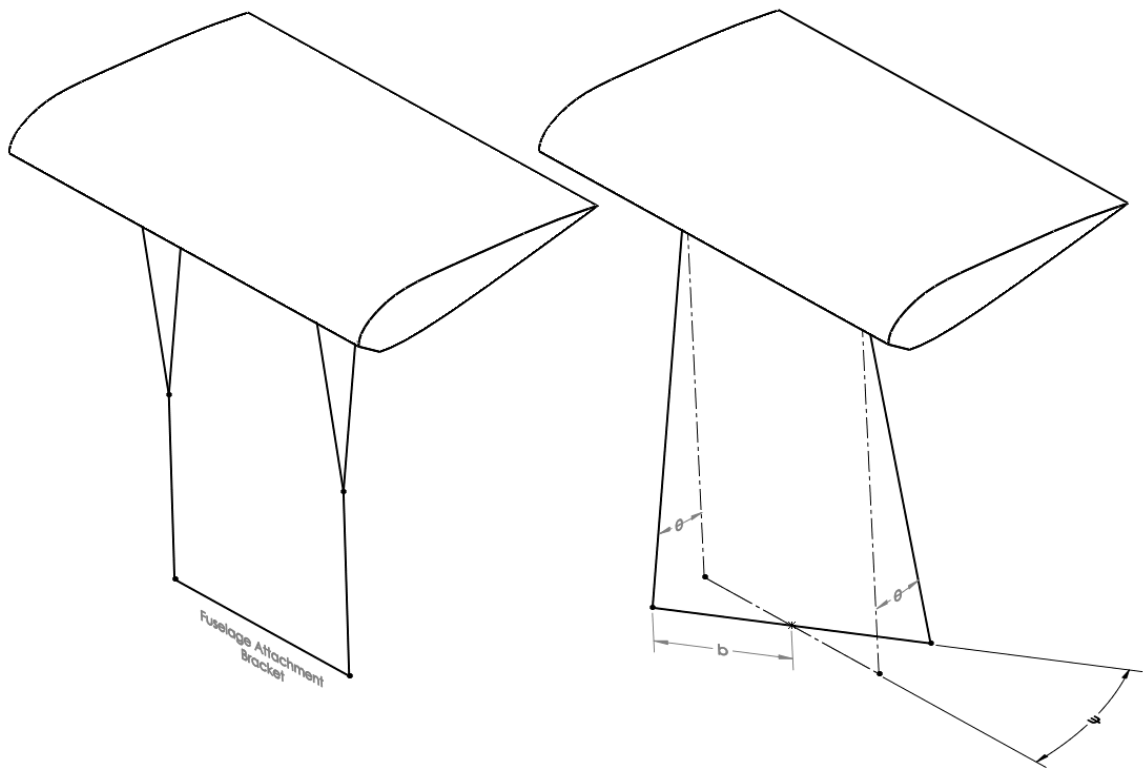


Figure 77: 3-Dimensional View of Yawing Twist

One important distinction is that even though in steady flight, where the tension would be constant, the magnitude of force applied about the fuselage yaw axis depends upon the angle θ , defined in Figure 75, which is directly related to ψ . To represent this connection between an angle in the longitudinal plane to the torque in the yaw plane, Figure 77 shows the system in three dimensions, and it can be seen that when the rigging line is angled from the twist there is a component of the tension force in the yaw plane, which will contribute to torsion.

Starting with Figure 76, the x displacement is equal to,

$$x = b \sin \psi \quad (5.24)$$

and from Figure 75,

$$x = l \sin \theta \quad (5.25)$$

Both of these can also be seen by Figure 77. The x-component of tension becomes,

$$F_x = F_t \sin \theta \quad (5.26)$$

Rearranging equation 5.25 and substituting it into equation 5.26 yields,

$$F_x = F_t \frac{x}{l} \quad (5.27)$$

By substituting in equation 5.24 the force can be related to the yaw angle with,

$$F_x = F_t \frac{b \sin \psi}{l} \quad (5.28)$$

Finally, the reaction torque produced by the rigging lines is,

$$\tau = 2F_t \frac{b^2}{l} \sin \psi \quad (5.29)$$

Therefore, it can be seen that the relation between the mounting distance, b , and the overall distance to the parafoil from the fuselage, l , play an important role in the directional stability of the fuselage. However, it also affects the lateral stability of powered vehicles. Given a disturbance that yaws the fuselage, the thrust is then vectored away from the direction of travel. As a result, a sideways component is added to the velocity of the paraglider, shown by Figure 78. As described earlier, this is negatively affected by the dihedral effect to create roll oscillations.

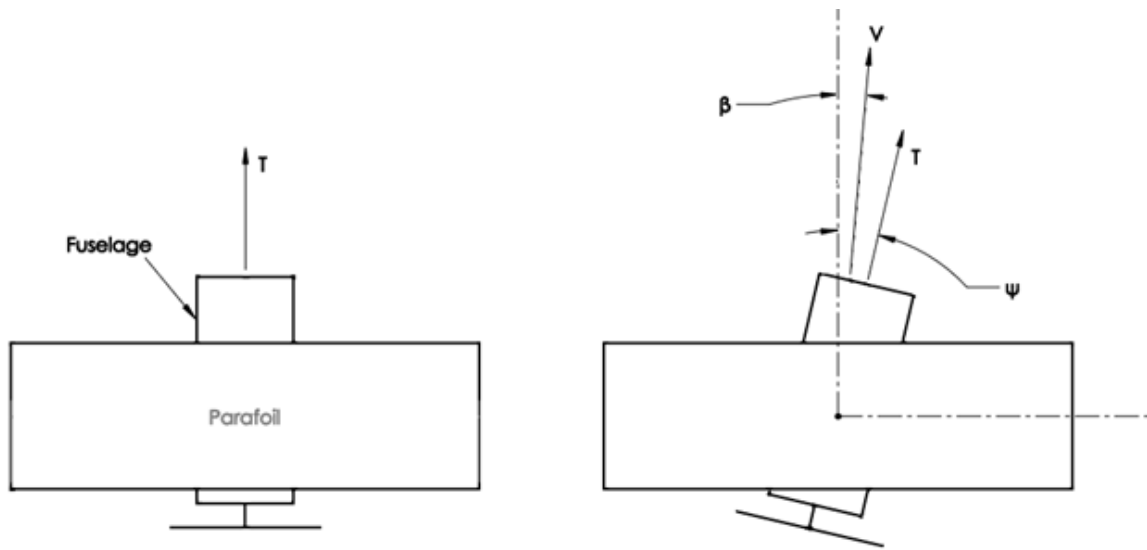


Figure 78: Yaw Induced Sideslip

Although, it is important to consider that this analysis is of simple motion and does not capture the entire behavior of a dynamic response. The movement is considered to only occur in two planes, longitudinal and directional.

5.2.2.2. WING ANHEDRAL

In the first configuration the wing formed a very steep arc with a large amount of anhedral. This was estimated to contribute greatly to the roll oscillations seen during the first flight. To solve the issue, extensions were placed in the lines running to the tips of the parafoil. This allowed them to rise higher and shallow the arc formed by the parafoil. Ultimately, the change was effective and the vehicle was much more stable and controllable during flight.

5.2.2.3. COMPARISON TO SIMULATION

With the paraglider able to maintain stable flight, video was taken during level steady flight, which was able to be compared to a simulation case with the same parameters. During flight the paraglider had all the same mass properties as set in the simulation, so variable parameters included rigging angle and thrust input. Throttle was maintained at roughly 70% for steady flight, which corresponds to about 1.2 lb of thrust from the powerplant data. Overlaying lines on the video capture, the rigging angle was able to be captured as well as the parafoil pitch angle, θ . Due to the low resolution of capturing the single frame and expanding to enlarge the paraglider, the measurements can only be considered approximate values. Additionally, the parafoil is slightly yawed so determining the exact middle location of the trailing edge is difficult. The resulting rigging angle is about -4° with the parafoil pitched backwards about 28° , seen in Figure 79.

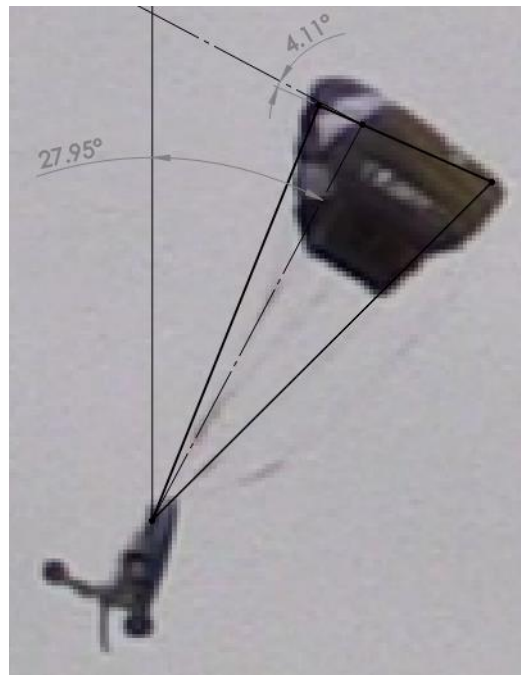


Figure 79: In Flight Rigging and Parafoil Pitch Angles

Entering these values into the simulation indicates a parafoil pitch angle of 24.0° for the given flight condition, with a climb of 2.2 ft/s. The difference in expected and experimental angles is

not unreasonable at 4°; however, the coarse measurement technique leaves some question to the accuracy of the comparison.

5.2.3. THIRD FLIGHT TEST

With the lateral oscillation issues largely resolved through the addition of the wider attachment bracket and shallowing the anhedral angle, a flight characteristic was observed during the second flight test. In flight the parafoil had a tendency to stall and lightly enter a roll. After which it recovered quickly but once the velocity returned the wing stalled again. To resolve the issue the parafoil lines were adjusted to the lengths given by Table 8 and Table 9, for an intended rigging angle of 6.5°.

The Ozone Quattro is easy to adjust with only two small lines driving the rigging angle. By measuring the distance between attachment points on the wing, a triangle can be formed between the two lines and the skin of the parafoil. With three sides the rigging angle can be determined; however, as stated previously, the attachment points will be further apart when the skin is lying flat than when it is inflated, due to the chamber of the parafoil.

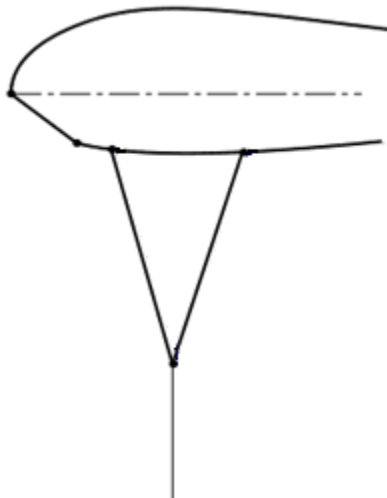


Figure 80: Ozone Quattro Rigging

Similar to the measurement technique in section 5.2.2.3, an image was taken from the video recording and overlaid with lines to obtain the rigging angle in flight. Based on photo measurements the rigging angle is about -7° , shown by Figure 81. When the distance between the attachment points is reduced the rigging angle grows in magnitude, so the more negative angle is expected.



Figure 81: Rigging Angle for Test Flight 3

With the reduced rigging angle, the paraglider was able to fly and climb steadier than in the previous 2 test flights; however, the winds were also stronger, which produced notable disturbances and ultimately caused the parafoil to collapse and twist. Additional weight would have aided in resisting disturbances but for consistency the weight was left equal to the earlier tests.

CHAPTER 6

CONCLUSIONS AND FUTURE WORK

6.1. CONCLUSIONS

A Lagrange equation based powered paraglider simulation was developed for use in modifying a paraglider vehicle and analyzing parameter effects on performance. The key parameters investigated were rigging angle, fuselage weight, center of gravity position, and “apparent mass.” With a design for stable flight based on parafoil wind tunnel tests, the paraglider test vehicle was modified as defined by the simulation and flown to observe its flight characteristics. Through flight observations, lateral and directional stability factors were also investigated. Three test flights were performed in total.

6.1.1. RIGGING ANGLE

Perhaps the most important aspect of design for a paraglider is the rigging angle of the parafoil. It defines the glide slope, which can be estimated with equations 5.1, 5.2, or 5.3. Typically, the more negative a rigging angle the steeper the glide. Additionally, more negative rigging angles are capable of handling larger thrust inputs and faster climb rates, seen by Figure 54. This increase in capability does come at the cost of less efficient level flight. Although limited in overall effect, at higher thrust inputs the best climb rate and best climb angle differ based on rigging angle. For more negative rigging angles the dynamic response to thrust inputs is damped quicker and experience a longer period.

6.1.2. WEIGHT & LOADING

The velocity of a paraglider in an unpowered glide is a function of weight or wing loading, with heavier fuselages descending faster than lighter fuselages. When thrust is applied to the paraglider the total velocity tends to decrease. If too much velocity is lost the wing will be unable to maintain enough lift for flight and the wing will stall; however, as the weight is increased there exists a point where the paraglider will have enough velocity to apply thrust without stalling. The behavior then changes to a force balance as the wing and fuselage pitch further upwards, along with their associated aerodynamic and thrust forces. As seen in Figure 59, rate of climb will taper off as weight increases, even as maximum thrust increases. Similar to rigging angle, additional weight allows a larger operating envelope but decreases efficiency, with more thrust required to maintain level flight.

Equation 2.10 was proven to hold true. As loading increases, the glide angle remains mostly constant but total velocity will increase. Seen in Table 12, the sink rate changes by 2 ft/s while over the same range glide angle remains within 0.1° .

For lighter weight paragliders the dynamic response will be greater in magnitude with a shorter period. This being due to a lighter weight mass being taken further away from its equilibrium point than a heavier weight, as well as having a greater difference in velocity between its power-on and power-off states.

6.1.3. CENTER OF GRAVITY

Whereas weight helps control the thrust line orientation, the center of gravity sets its incidence. Equating the system again to Figure 62, it was shown the center of gravity placed forward of the attachment point will cause the fuselage and thrust line to rotate downward and vice-versa for the aft position. For the test cases performed, the more forward the center of gravity position the lower the magnitude of the dynamic response but frequency is nearly equal.

Performance capacity decreases with extreme center of gravity positions, forward or aft. For this test model the best position was just in front of the attachment point by 5°.

6.1.4. “APPARENT MASS” EFFECTS

Based on research, “apparent mass” effects are very important to include in models with light wing loadings, especially when the lifting surface is far from the main body. Surprisingly, in this analysis both cases with and without “apparent mass” appeared very similar in a dynamic response. Without “apparent mass,” the response had about the same magnitude but shorter period. Given that in an analysis of both cases the motion is represented with such similarity, omission of the “apparent mass” approximation terms is a viable and possibly appropriate option.

6.1.5. VEHICLE STABILITY

Although paragliders tend to naturally be stable due to keel or pendulum effects, there are a few factors that can improve or degrade the stability of the aircraft. Wing dihedral was found to have a large impact of the lateral stability of the paraglider. Once roll oscillations began they were difficult to overcome. This was compounded by twisting between the fuselage and parafoil, which results in the thrust vector causing a sideslip component. With sideslip the negative dihedral effect from wing anhedral causes the vehicle to roll. By extending the wing tip lines and allowing them to rise, the anhedral angle and dihedral effect were reduced. In order to increase twisting resistance, equation 5.29 was derived and found by extending the mounting bracket outwards the lines would produce greater reaction torque.

6.1.6. DYNAMIC MODEL

The simulation established by the Lagrange equation method provides a nonlinear system in terms of relatable design parameters. The model benefits from the method’s ability to define generalized coordinates and simplify the system. It also holds potential for the ASTRO program

in the ability to add additional masses, as shown by Quisenberry. However, the method is cumbersome for a two body system, for which other models have been proven. For standard paragliders a different method may be best, but for several loosely attached payloads it is a good choice.

6.2. FUTURE WORK

From the beginning, this research has worked to further the capabilities of the ASTRO program through an understanding of paragliders and the most critical parameters in their design. The simulation and flight testing has established a foundation for future development; however, there are a few topics left unsolved or lacking certainty.

First and foremost, more parafoil performance data is needed. Without a clear understanding of the aerodynamics on a parafoil, any research based on that data will carry a degree of uncertainty. Nicolaidis provided plentiful and useful data, but modern parafoils have developed more complex sections and higher aspect ratios. Updating the data pool with these types of parachutes would help eliminate errors when transferring from a theoretical simulation to the physical test vehicle.

Although omitted from this model, line drag will have some effect on the performance of a paraglider and should be modeled for a truly representative analysis. With this background on approaching a powered paraglider system with the Lagrangian equation method, it is possible for others to implement the extra force into the model with relative ease.

On that same note, adding additional masses to the system is sure to produce interesting results, and it is a critical component of adapting it to the ASTRO program. However, with an unpowered decelerator, like the ASTRO payload recovery vehicle would be, it is probable that more interesting than the longitudinal motion would be the interactions between the longitudinal, lateral, and directional movement.

REFERENCES

- [1] Dennis, D. R. *Recent advances in parachute technology*. No. RAE-TM-FS (F)-514. ROYAL AIRCRAFT ESTABLISHMENT FARNBOROUGH (UNITED KINGDOM), 1983.
- [2] Potvin, Jean, et al. "Glide Performance Study of Standard and Hybrid Cruciform Parachutes." *17 th AIAA Aerodynamic Decelerator Systems Technology Conference and Seminar*. 2003.
- [3] Dillon, Sharon. "Virginia Aviation History Project Report."
- [4] Fournier, Paul G., and B. BELL. *Transonic Pressure Distributions on Three Rigid Wings Simulating Paragliders with Varied Canopy Curvature and Leading-Edge Sweep*. No. TN D 1009. NATIONAL AERONAUTICS AND SPACE ADMINISTRATION WASHINGTON DC, 1962.
- [5] "Oxy 0.5." *Opale Paramodels*. Opale Paramodels, n.d. Web. 26 Aug. 2016. <<http://www.opale-paramodels.com/index.php/en/shop-opaleparamodels/wings/oxy-0-5/oxy-0-5-detail>>.
- [6] "Mosquito Tactical Resupply System (MTRS)." *STARA Technologies, Inc.* STARA Technologies, Inc., n.d. Web. 07 Nov. 2016. <<http://www.staratechnologies.com/mosquito.html>>.
- [7] Nicolaidis, John D. *Parafoil wind tunnel tests*. Notre Dame Univ in Dept of Aerospace and Mechanical Engineering, 1971.
- [8] Nicolaidis, John D., and Michael A. Tragarz. *Parafoil flight performance*. NOTRE DAME UNIV IN DEPT OF AEROSPACE AND MECHANICAL ENGINEERING, 1971.

- [9] Furfaro, James, et al. "An experimental study of parafoil sections." *14th Aerodynamic Decelerator Systems Technology Conference and Seminar, San Francisco, USA*. 1997.
- [10] Uddin, Md Nizam, and Mohammad Mashud. "Wind tunnel test of a paraglider (flexible) wing canopy." *International Journal of Mechanical-Mechatronics Engineering* 10.3 (2010): 7-18.
- [11] Jann, Thomas. "Aerodynamic Coefficients for a Parafoil Wing with Arc Anhedral - Theoretical and Experimental Results." *17th AIAA Aerodynamic Decelerator Systems Technology Conference and Seminar*(2003): 50-59. AIAA. Web. 7 Sept. 2016. <<http://arc.aiaa.org/doi/abs/10.2514/6.2003-2106>>.
- [12] Gonzalez, M. A. "Prandtl theory applied to paraglider aerodynamics." *RAeS/AIAA Aerodynamic Decelerator Systems Technology Conference and Seminar, 12 th, London, United Kingdom*. 1993.
- [13] Iosilevskii, Genady. *A Paraglider: Performance, Aerodynamics, and Flight Mechanics*. Technion-IIT, Faculty of Aerospace Engineering, 1993.
- [14] Cao, Yihua, and Xu Zhu. "Effects of characteristic geometric parameters on parafoil lift and drag." *Aircraft Engineering and Aerospace Technology* 85.4 (2013): 280-292.
- [15] Lissaman, P. B. S., and GLEN BROWN. "Apparent mass effects on parafoil dynamics." *RAeS/AIAA Aerodynamic Decelerator Systems Technology Conference and Seminar, 12 th, London, United Kingdom*. 1993.
- [16] Conner Jr, Joseph P. "Development of a real-time performance predictor and an investigation of a return to point vehicle for high altitude ballooning." (2009).
- [17] Slegers, Nathan, and Mark Costello. "Aspects of control for a parafoil and payload system." *Journal of Guidance, Control, and Dynamics* 26.6 (2003): 898-905.
- [18] Chambers, John. "Longitudinal dynamic modeling and control of powered parachute aircraft." (2007).
- [19] Burcham Jr, Frank W., et al. "Preliminary Flight Results of a Fly-by-Throttle Emergency Flight Control System on an F-15 Airplane." (1993).
- [20] Yakimenko, Oleg A. "On the development of a scalable 8-DoF model for a generic parafoil-payload delivery system." *AIAA Paper* 1665 (2005): 2005.
- [21] Watanabe, Masahito, and Yoshimasa Ochi. "Modeling and motion analysis for a powered paraglider (PPG)." *SICE, 2007 Annual Conference*. IEEE, 2007.

- [22] Quisenberry Jr, Johnny Earl. *Dynamic Simulation of Low Altitude Aerial Tow Systems*. Diss. Oklahoma State University, 2005.
- [23] Greenwood, Donald T. *Principles of dynamics*. Englewood Cliffs, NJ: Prentice-Hall, 1988.
- [24] Yamauchi, Brian, and Pavlo Rudakevych. "Griffon: a man-portable hybrid UGV/UAV." *Industrial Robot: An International Journal* 31.5 (2004): 443-450.
- [25] "Generalized Forces with Double Pendulum Example." *MIT OpenCourseWare*(2011): n. pag. Web. 2 Sept. 2016.
- [26] Nelson, Robert C. *Flight stability and automatic control*. Vol. 2. WCB/McGraw Hill, 1998.

APPENDICES

APPENDIX A: FIGURES

AIRFOIL	
Station	Ordinates
0.	0.0886
.0200	.1206
.0400	.1392
.0500	.1518
.0800	.1616
.1000	.1688
.1056	.0000
.1200	.1730
.1400	.1756
.1600	.1750
.1800	.1784
.2000	.1790
.2200	.1790
.2400	.1768
.2600	.1752
.2800	.1730
.3000	.1705
.3200	.1676
.3400	.1646
.3600	.1605
.3800	.1562
.4000	.1524
.4200	.1476
.4400	.1426
1.0000	0.0000

Figure 82: Nicolaides Models 8-13 Section Coordinates [7]

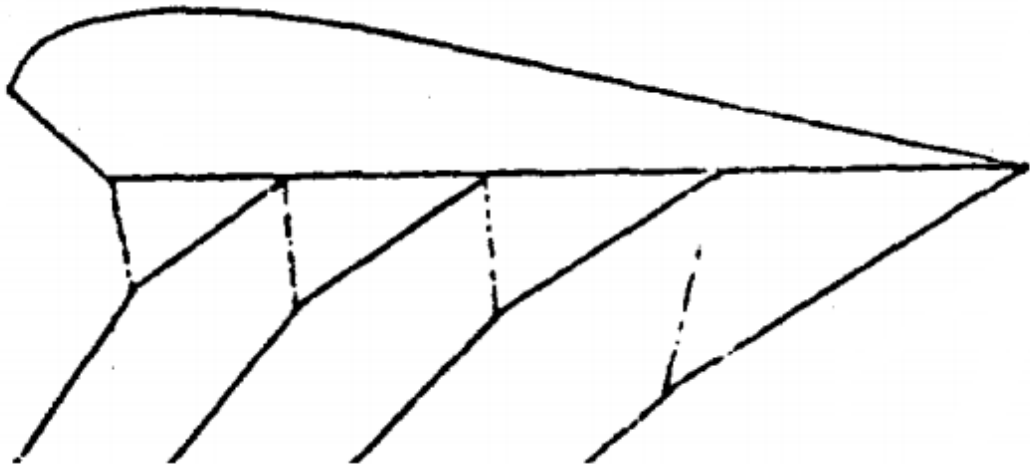


Figure 83: Nicolaides Model 8-13 Wing Section [7]

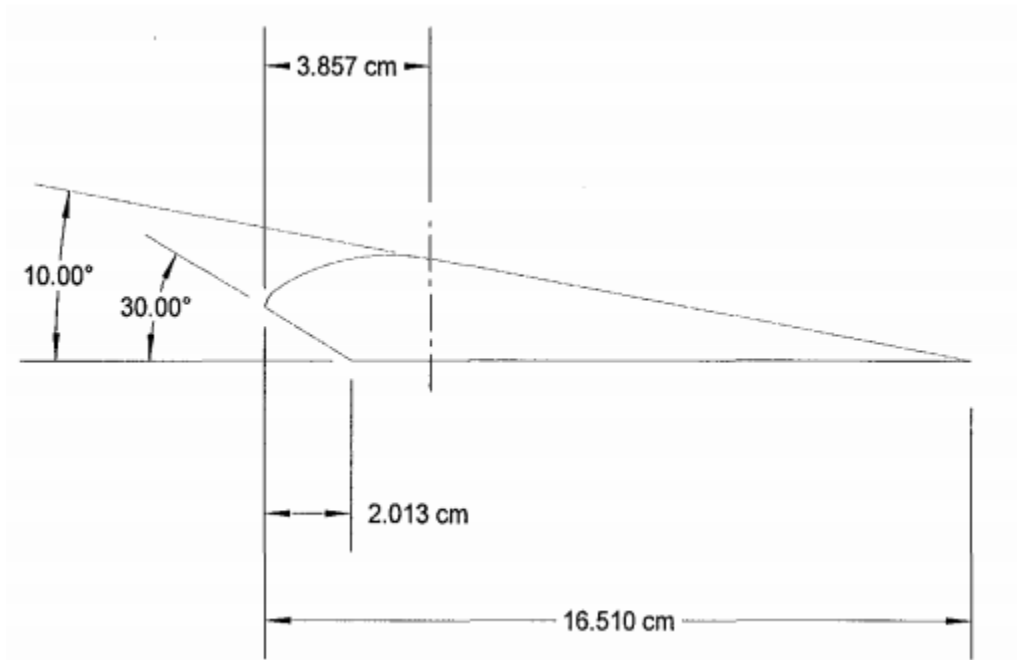


Figure 84: Furfaro Parafoil Cross-Section [9]

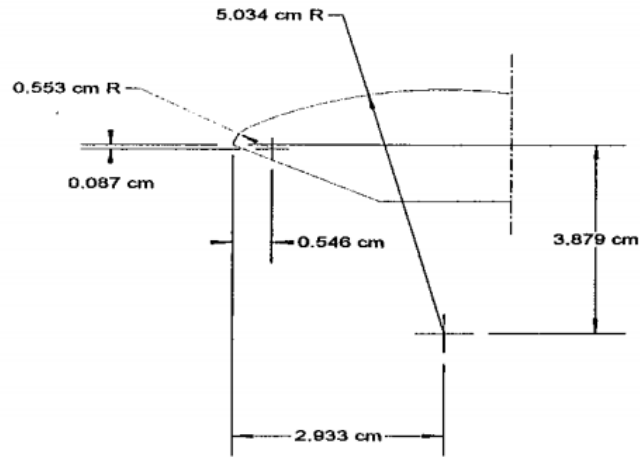


Figure 85: Furfaro Parafoil Truncated Nose Dimensions [9]

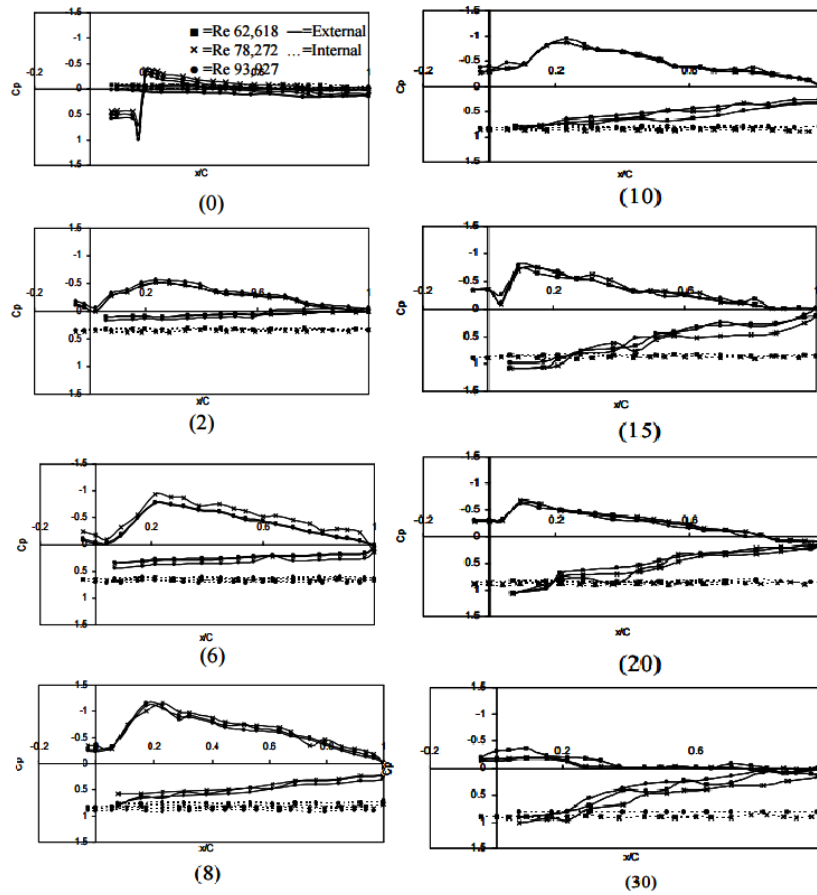


Figure 86: External Pressure Distribution for Wings at Various Angles of Attack [10]

Derivative	Lifting Line	Vortex Lattice
$C_{L\alpha}$	2.184	2.009
$C_{D\alpha}$	0.498	0.344
$C_{m\alpha}$	0	0.615
C_{mq}	-0.182	-0.113
$C_{Y\beta}$	-0.224	-0.171
$C_{l\beta}$	0.11	0.122
$C_{n\beta}$	0.02	0.014
C_{Yp}	0.22	0.243
C_{lp}	-0.157	-0.174
C_{np}	-0.028	0.02
C_{Yr}	-0.117	0.051
C_{lr}	0.116	-0.037
C_{nr}	-0.026	-0.01

Table 13: Coefficients for Parafoil Wing [11]

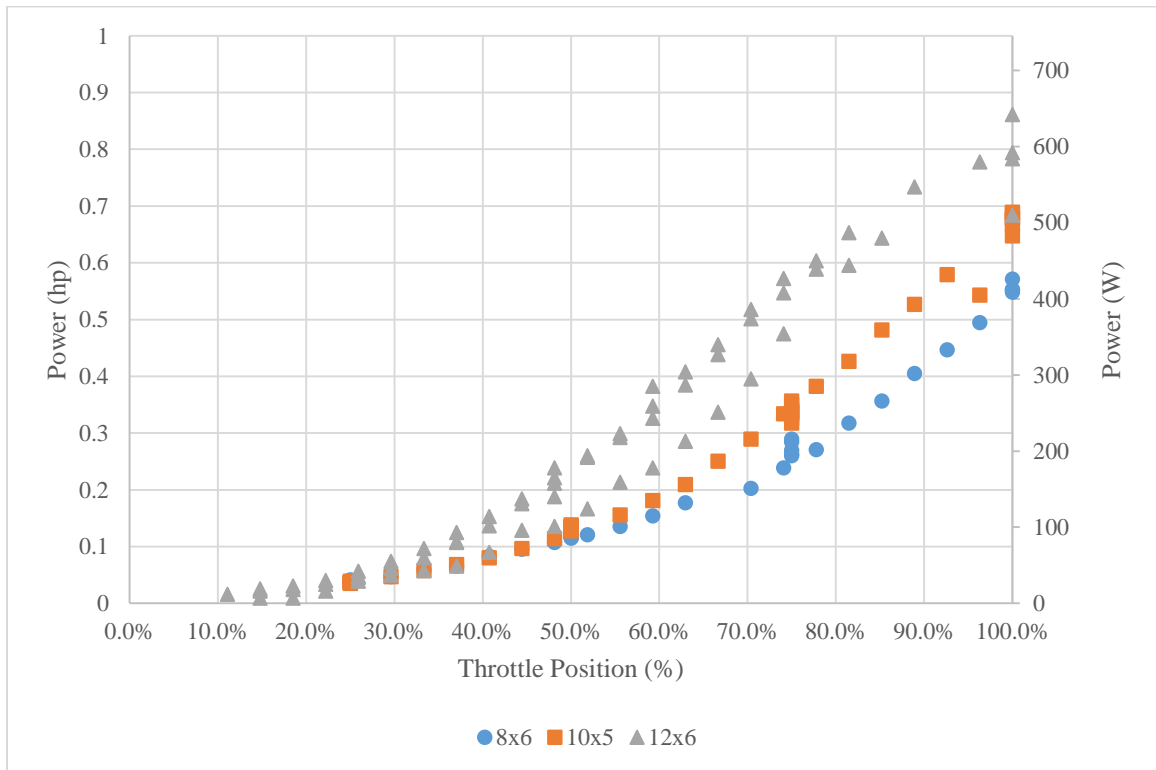


Figure 87: Powerplant Power Output with Throttle Input

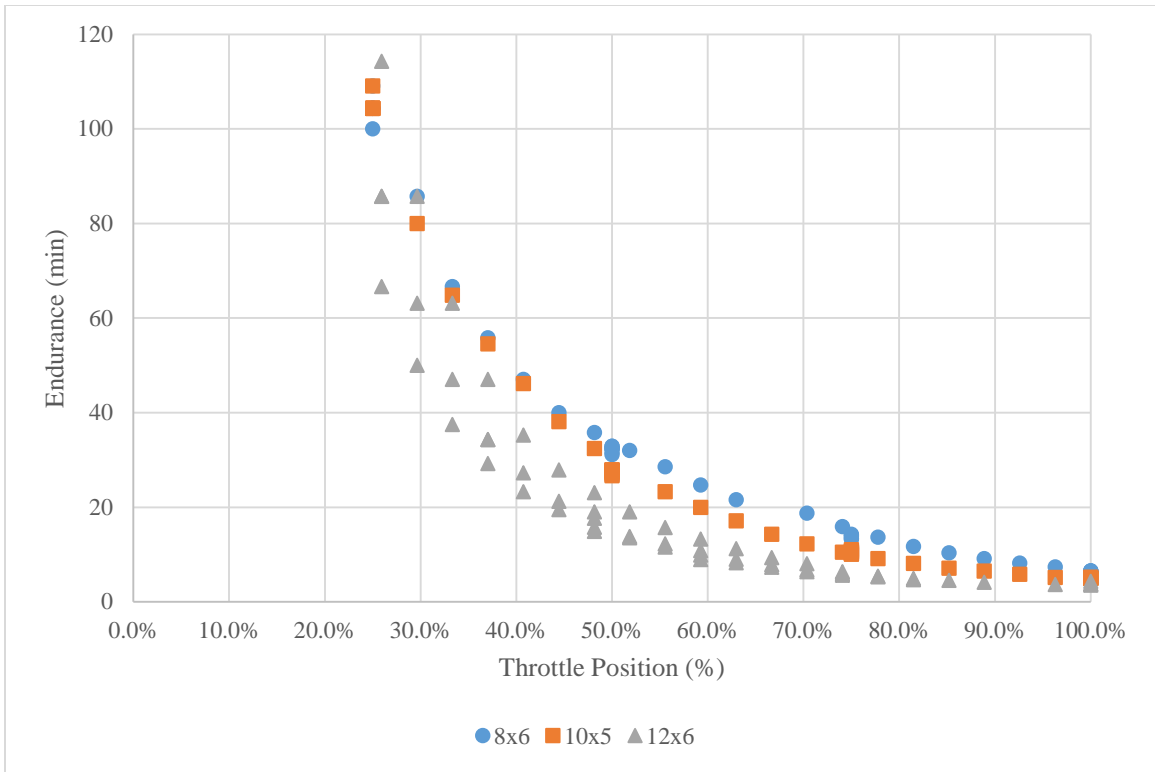


Figure 88: Endurance for Throttle Input with 4000 mAh Battery

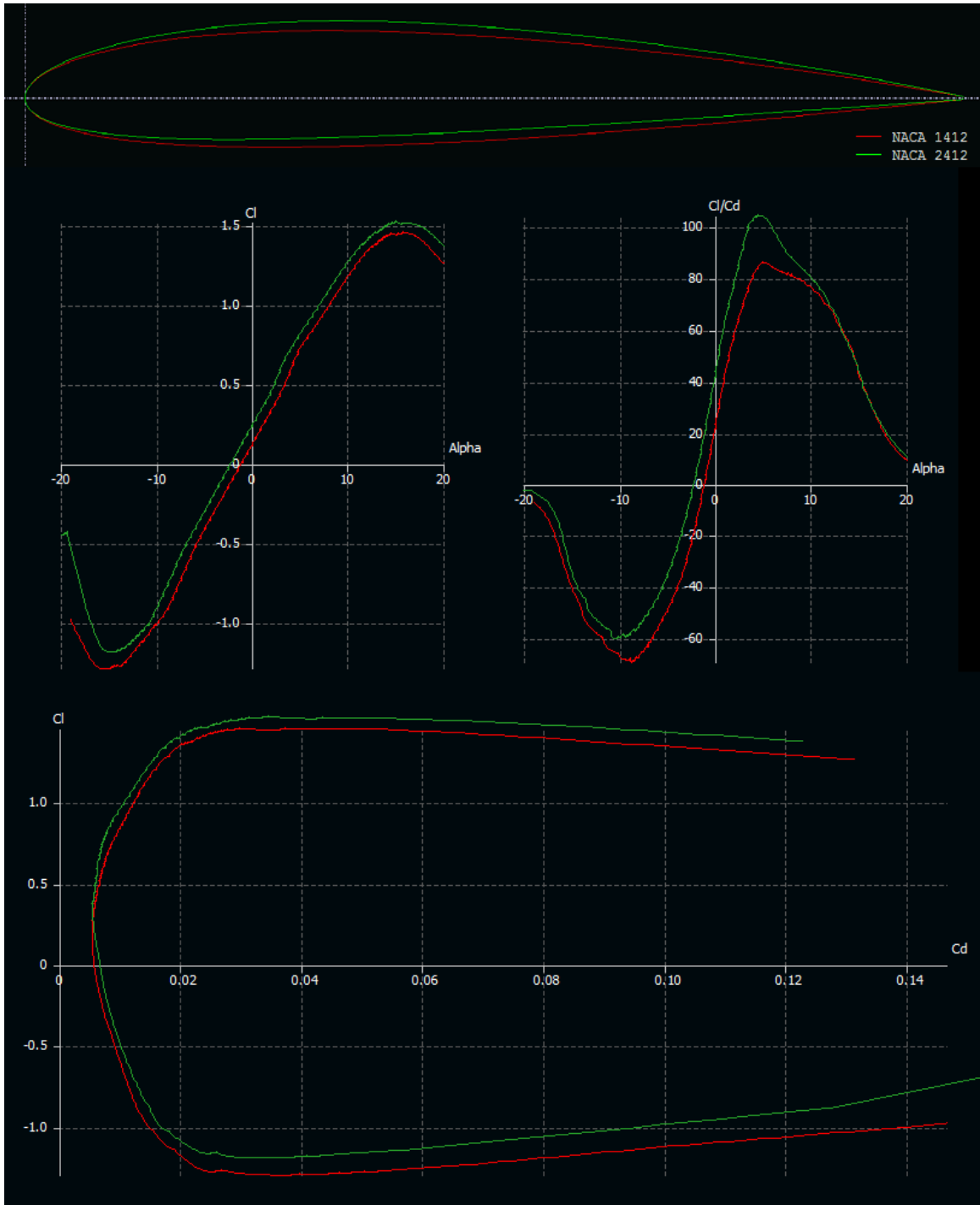


Figure 89: XFOIL Analysis of 1412 and 2412 Airfoils

APPENDIX B: SIMULATION GUIDE

The simulation is built in Mathcad 15 based on its ability to easily calculate derivatives symbolically and numerically solve systems of differential equations. It also supports easy animations for displaying responses in a way that graphs and charts do not fully express. It also presents the material similar to a word processor, which allows it to be easily organized and increases readability. There are several segments to the code that contain different aspects of the analysis. This section will cover those segments and how the simulation functions through them.

The first section, “Utility/Wing Parameters,” takes inputs for the more fixed values of the paraglider in question, as well as calculating the apparent mass value according to equations 2.1 and 2.2. Additionally, some parameters are setup here for later use. The system parameters “PRNPRECISION” affects the number of digits in prn files while “ORIGIN” sets the default starting row for matrices and vectors as 0 or 1. The vehicle variables covered in this section are:

- c – Chord
- b – Span
- S – Planform area
- t_w – Wing thickness
- C_{Df} – Fuselage drag coefficient
- A – Fuselage frontal area
- m_2 – Wing mass
- m_1 – Fuselage mass
- p – Distance from cg to attachment point
- i_p – Angle between cg, attachment point, and vertical
- l_T – Distance from cg to thrustline

The next section, “Validation Thrust,” allows the use of user input thrust data into the simulation instead of a single instantaneous step. This can also be used to validate against known experimental data. To enable, right-click and select enable evaluation on the $T(t)$ function. Then in the “Control” section, right-click on the main $T(t)$ function and select disable evaluation. This ensures there is only one function is enabled for any analysis. To change the reference thrust data file right click on the $ExpT$ variable definition and select “Properties” and browse for the file under the “File Options” tab. For best results use a delimited file type, with column 1 being time

and column 2 being the thrust at that time. Since the thrust function works off linear interpolation all time entries must be unique.

“Airfoil & Polar Data” allows the input of airfoil performance data. This is done by right-clicking on the Aero variable, selecting “Properties,” and browsing for the file under the “File Options” tab. By default, the Aero variable is set to start reading data from the 13th row, where angle of attack is in column 1, C_L is in column 2, and C_D is in column 3. This can be changed by setting the starting row in “Properties>Data Range” and changing the alpha, lift, or drag variables in “Utility/Wing Parameters” to the desired column numbers. The data can then be altered within the program by shifting C_L and C_D data left or right using the α_{shift} variable, or scale C_L or C_D by using the $C_{L\text{factor}}$ and $C_{D\text{factor}}$ multipliers, respectively. The data is then displayed on plots for C_L vs. α , C_D vs. α , and L/D vs. α . The final function of this section is to process C_L and C_D for the lift and drag functions. The lift and drag functions call the C_L and C_D function, which either linearly interpolates the coefficient for an input angle of attack or sends back a fixed C_L or C_D for validating with Chambers’ method. This is determined by a validation variable in the “Control” section and will be explained later.

The “Parachute Parameters/Calc/Preview” section calculates the various angles and geometry made by the parafoil and connecting lines. It also features a preview of the parafoil at the end. Calculations begin by finding x- and y-points for the ends of the parafoil, as well as the $c/4$ location. Then, using those points, angles can be found. This section requires an initial guess for the starting pitch angle for the leading edge line, θ_{le} . At zero the leading edge is vertical and rotates forward with positive angles. However, the program feeds the value from the $\theta_{le}-\phi$ calculation into θ_{le} and the calculations are performed again. The parafoil’s ac line will be vertical, all values of wing incidence (i_w) will be equal, and i_w will be the rigging angle for the parafoil.

“AoA Prediction” predicts the angle of attack and resulting lift to drag ratio of a parafoil based on a range of rigging angles. Simply enter the lowest considered whole angle into ang_{min} and the largest whole angle into ang_{max} . Note that there may not be a solution for every rigging angle and there could also exist multiple solutions. The default alpha guess is 0° , and should be on the more conservative side of guesses, but adjust that number if the results seem incorrect.

“Lagrangian Equation Energy and Forces Setup” follows the solution set forth by section 4.4. There are no variables or functions in this section, but it may be used for reference as to how the solution was derived.

“Force, Gamma, and Alpha Definitions” is also a reference section only, that tells how the flight paths and angle of attack are calculated, as well as velocities and forces. There is one flight path for each body, fuselage and wing, which follow equation 4.5. Angle of attack is simply the flight path angle of the wing plus its current incidence angle, shown by equation 4.6.

“Force, Gamma, Alpha Functions” takes the definitions from the previous section and writes them into functions that can be called throughout the rest of the program. The function for fuselage drag, D_f , has two possible evaluations based on whether the validation variable is flagged or not. If it is flagged, with values 1 or 2, the program returns a drag value based on velocity from Chambers, but if it is not flagged, having a value of 0, it returns drag using the traditional drag equation, shown by equation 4.9.

“Lagrange Equations” is another reference section that combines the different parts of the solution into a system of four equations. It leads into the next section “General Lagrangian Equation Solution.” Due to the complexity of the system, equations were not able to be simplified and instead broken into functions that could then be substituted back into the equations. The variables are replaced with an arbitrary variable in an attempt to make the functions appear more general, as they are used throughout the simulation. The result is four

main functions with seven supporting functions. Even with the use of support functions, the solution appears very complex.

“State Space Conversions & Initial Conditions” is used to calculate a steady-state solution for the system, by setting the main functions equal to 0, which is equivalent to setting accelerations to 0. Using a Given-Find block with initial guesses for each variable the steady-state variables can be numerically evaluated. Note that the initial guesses are vitally important for finding the correct solution, as many exist for any given system. A better system has not been devised for automatically determining proper solutions so this is left up to the user to cycle through initial guesses to determine a correct configuration versus one that is obviously incorrect. Climbing through x_2 values is a fairly reliable, albeit time consuming, for finding correct configurations. The solution will then be used in the section “Differential Equation Solver.” where instead of being set to 0 the four main functions are input into a differential equation solver, with the initial conditions being the previous section’s solution. The solver is a fixed step size Runge-Kutta numerical method. Mathcad also supports an adaptive step size solver but errors occurred for some analyses. Variables are then extracted from the solver matrix for processing in “Solver Outputs and Calculations.” Using the functions given in the previous sections, variables are solved for each time step. These include the four generalized coordinates and their derivatives, as well as total velocities, angles, lift, and drag.

“Animation Support,” as its name suggests, provides supporting calculations and positioning for creating animations of the system dynamics. Each point of the drawing is calculated including those representing the body and forces. These points can then be mapped into vectors, such that when drawn there is a line between each of the points, creating a picture. A simple way to map x- and y-coordinates is to define all x-coordinates in the real domain and all y-coordinates in the imaginary domain, so if the imaginary portion is plotted against the real portion the points come

out separately. There is a variable called dGain that can be used to scale up the drag vectors in the animation, since they can be hard to see depending on aircraft parameters.

“Data Logging” provides two ways to output the results of the simulation. The first is to an output file and the second is via copy and paste from a matrix directly into a spreadsheet. When outputting to a file the program uses a macro to delete the current output file, if it exists, then writes the solver outputs and calculated parameters to a new file. It deletes the existing file to avoid any errors with writing data on top of previous data. The location of the file is set in the “Control” section, as well as whether to enable data logging or file deletion. A matrix then displays the contents of the output file that can be used as verification of successful operation. The second option uses an output matrix, called “output,” that can be copied and pasted easily into a spreadsheet. To transfer all the data, right-click on the output table and select “Select All.” Right-click again and select “Copy Selection.” The data should then be ready to paste into a spreadsheet, but without headers. The headers can be found as the “labels” variable in the output data file section.

The next section “Control” is the primary center for changing key variables and setting certain simulation functionalities. The geometric and starting constraints set the geometry of the parafoil based on the line lengths from the trailing edge or leading edge to the connection point of the fuselage and the starting altitude for analysis. The response conditions set the thrust input to the program and specify how long each state is to last and the magnitude during those periods. By default, there are two steps but more could be added by adding lines and logic to the $T(t)$ function. The starting condition is steady-state, where the paraglider has zero accelerations for the first thrust applied, given by the initial conditions section, and the response thrust provides a sudden change in magnitude. FlagVal is a flagging variable than can be changed to alter the behavior of the analysis. With 0 the default simulation is performed with the Lagrangian method, while 1 or 2 instruct the program to use alternative methods for calculating wing lift, wing drag,

and fuselage drag based on parameters set by Chambers in his model. Validation method 1 used calculated C_L and C_D values based on direct numbers from Chambers' research, while 2 uses a constant angle of attack to achieve the same lift to drag ratio value in his paper from the Nicolaides data. LogFlag enables data logging, file sets the file to be output, and DeleteFlag indicates if the file should be deleted before beginning the analysis. In both cases 0 disables functionality and 1 enables it.

“Results and Animation” provides graphs of the important variables in the analysis as well as a line representation of the system that changes for each time step. This enables an effective tool for analysis, animation. To start an analysis, take a note of the fps variable in the top left of the section as it will be used when setting the speed of the video. Animations work by using a variable, FRAME, to count progressively, and when attached as the index of a variable each value can be stepped through. In charts this means refreshing the graphic for every time step, or index of each variable, and stitching them together to form a continuous picture of the conditions at every time step. To capture the entire analysis, FRAME will need to be set to every index value, 0 to 999 by default. Select Tools>Animation>Record... to begin. In the “From” box enter the lowest index value, normally 0, and in the “To” box enter the highest index value, normally 999. “At” determines the playback speed in frames per second. Enter the fps value from earlier in this box to set the playback to real-time speed. This can be adjusted to speed up or slow down analysis. To finish the animation, click and drag a box around the section of the Mathcad window desired and click the “Animate” button. A preview will appear in the dialog box, accompanied by the current value of FRAME. This can also be used as a progress indicator by comparing FRAME to the max index value input in the “To” box. When the animation is complete a preview window will be displayed. When finished previewing, click the close button in the top right of the window and click “Save As...” in the original dialog box to save the video to the computer. The next section, “Global Animation,” the system is displayed from an Earth-

fixed reference as the paraglider flies from right to left. This animation may not work well for some systems and may need to be adjusted based on horizontal and vertical travel.

The last section, “Variables,” is mainly for debugging but can be used to see the most important variables over time. If an analysis seems incorrect this section should provide insight on potential issues.

APPENDIX C: MATHCAD SIMULATION CODE

<p>Utility/Wing Parameters</p> <p>Utility</p> <p>$i := 0..1000$</p> <p>$\alpha_{plot} := 0.02 \text{deg}(i - 500)$</p> <p>$C_{L,2\pi} := 2 \cdot \pi \cdot \frac{\pi}{180 \text{deg}} \cdot \alpha_{plot}$</p> <p>alpha := 1 lift := 2 drag := 3</p> <p>PRNPRECISION := 5 ORIGIN := 1</p> <p>Wing Parameters</p> <p>$c_w := \frac{25.5}{12}$ $b := \frac{61}{12}$ $S_w := c \cdot b = 10.802$ $t_w := \frac{3}{12}$</p>	<p>Index</p> <p>Numbers to generate 2π lift curve</p> <p>Polar data import numbers</p> <p>System Parameters</p> <p>Chord, span, planform area (automatically calculated), and wing thickness</p>
<p>Other System Parameters</p> <p>$g_w := 32.167$</p> <p>$\rho := 0.00237688318$</p> <p>$A_w := 0.34$</p> <p>$m_1 := 0.0874 \cdot 1.75$ $W_1 := m_1 \cdot g = 4.92$</p> <p>$m_2 := .01212$ $W_2 := m_2 \cdot g = 0.39$</p> <p>$W_{tot} := W_1 + W_2 = 5.31$</p>	<p>Gravitational acceleration and aspect ratio (automatically calculated)</p> <p>Air density</p> <p>Fuselage frontal area and drag coefficient</p> <p>Mass and weight of fuselage (1) and wing (2)</p>
<p>"Apparent Mass"</p> <p>$m_{appA} := 0.666 \cdot t_w^2 \cdot b \cdot \rho = 5.029 \times 10^{-4}$</p> <p>$m_{2x} := m_2 + m_{appA} = 0.013$</p> <p>$m_{appC} := 0.785 \cdot b \cdot c^2 \cdot \frac{AR}{1 + AR} \cdot \rho = 0.03$</p> <p>$m_{2y} := m_2 + m_{appC} = 0.042$</p> <p>Calculate values together from Stability spreadsheet</p> <p>$J_1 := 0.012$ $i_p := 5 \text{deg}$</p> <p>$p := \frac{8.487}{12}$ $I_T := \frac{4.862}{12}$</p>	<p>"Apparent mass" approximations from Lissaman [15]</p> <p>Center of gravity and thrustline offset</p> <p>See definition in thesis</p>

Validation Thrust

ExpT := 

$$T(t) := \begin{cases} \text{linterp}(\text{ExpT}^{(1)}, \text{ExpT}^{(2)}, t) & \text{if } t \geq 0 \\ 0 & \text{otherwise} \end{cases}$$

$T_{\text{max}} := T(0) = 0.75$

Validation Thrust

Set file with right-click, "Properties", and browse for thrust data file

To use thrust data from Chambers' flight test set:

tss = 4.8

tres = 4.1016

and re-enable evaluation of the T(t) function in this section.

Airfoil & Polar Data

Import polar data file

.Aero := 

D:\...WindTunnel\TabularSet.dat

Scaling factor and α -shift utility

$\alpha_{\text{shift}} := 0$

$C_{L\text{factor}} := 1$

$C_{D\text{factor}} := 1$

$\text{Aero}^{\langle \text{alpha} \rangle} := \text{Aero}^{\langle \text{alpha} \rangle} + \alpha_{\text{shift}}$

$\text{Aero}^{\langle \text{lift} \rangle} := C_{L\text{factor}} \cdot \text{Aero}^{\langle \text{lift} \rangle}$

$\text{Aero}^{\langle \text{drag} \rangle} := C_{D\text{factor}} \cdot \text{Aero}^{\langle \text{drag} \rangle}$

Set file with right-click, "Properties", and browse for performance data file

Shift curve left or right by degrees of α (default: 0)

Scaling factor to modify each CL value (default: 1)

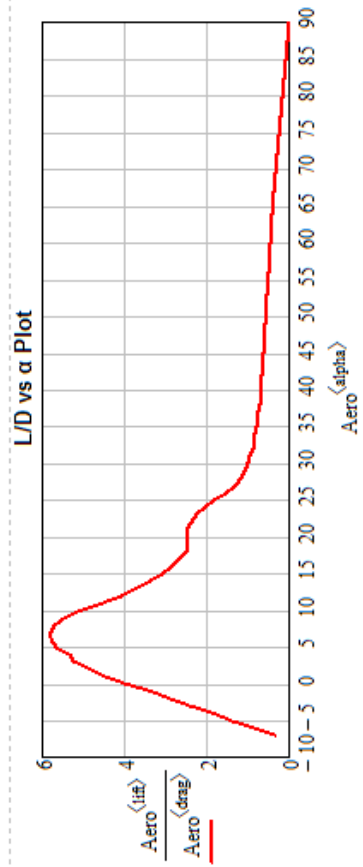
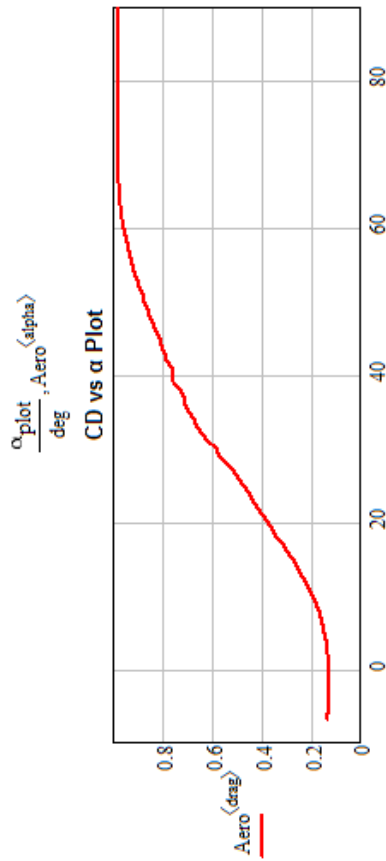
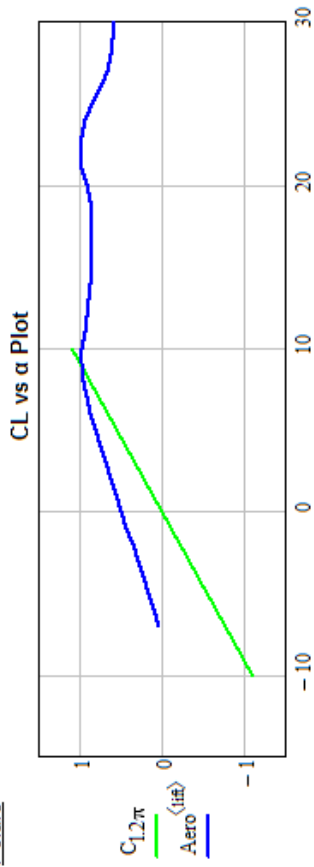
Scaling factor to modify each CD value (default: 1)

CL scale equation

CL scale equation

CD scale equation

Polars



Alpha	CL	CD	L/D
1	-7	0.043	0.131
2	-6	0.109	0.13
3	-5	0.175	0.128
4	-4	0.235	0.126
5	-3	0.302	0.125
6	-2	0.364	0.126
7	-1	0.429	0.126
8	0	0.503	0.126
9	1	0.562	0.126
10	2	0.623	0.13
11	3	0.687	0.131
12	4	0.744	0.139
13	5	0.811	0.143
14	6	0.876	0.151
15	7	0.927	0.16
16	8	0.964	0.169
17	9	0.977	0.181
18	10	0.972	0.193
19	11	0.946	0.208
20	12	0.917	0.224
21	13	0.89	0.24
22	14	0.866	0.257
23	15	0.85	...

$$\frac{Aero = \langle lift \rangle}{Aero \langle drag \rangle} =$$

Lift/ Drag coefficient functions

$$C_L(\alpha) := \begin{cases} .383 & \text{if FlagVal} = 1 \\ \text{linterp}(\text{Aero}\langle\text{alpha}\rangle, \text{Aero}\langle\text{lift}\rangle, -0.5) & \text{if FlagVal} = 2 \\ \text{linterp}(\text{Aero}\langle\text{alpha}\rangle, \text{Aero}\langle\text{lift}\rangle, \alpha \frac{180}{\pi}) & \text{otherwise} \end{cases}$$

$$C_D(\alpha) := \begin{cases} .106 & \text{if FlagVal} = 1 \\ \text{linterp}(\text{Aero}\langle\text{alpha}\rangle, \text{Aero}\langle\text{drag}\rangle, -0.5) & \text{if FlagVal} = 2 \\ \text{linterp}(\text{Aero}\langle\text{alpha}\rangle, \text{Aero}\langle\text{drag}\rangle, \alpha \frac{180}{\pi}) & \text{otherwise} \end{cases}$$

Lift and drag coefficient lookup functions

By default, runs linear interpolation on performance data from file declared by Aero variable for a given angle of attack

With FlagVal=1, the function returns a fixed value corresponding to Chambers' parafoil

With FlagVal=2, the function returns a value related to a fixed angle of attack (by default -0.5, which can be adjusted)

Airfoil & Polar Data

Parachute Parameters/Calc/Preview

Parachute Parameters & Trig

First iteration

$$\theta_{le} := 0 \text{deg}$$

$$\psi := \theta_{le} - \arccos\left(\frac{l_e^2 + l_e^2 - c^2}{2 \cdot l_e \cdot l_e}\right) = -27.62 \text{deg}$$

$$x_a := l_e \cdot \sin(\theta_{le}) = 0$$

$$x_b := l_e \cdot \sin(\psi) = -2.125$$

$$x_c := (x_a - x_b) \cdot (1 - .25) + x_b = -0.531$$

$$l_{ac} := \sqrt{x_c^2 + y_c^2} = 4.112$$

$$y_a := l_e \cdot \cos(\theta_{le}) = 4.083$$

$$y_b := l_e \cdot \cos(\psi) = 4.061$$

$$y_c := (y_a - y_b) \cdot (1 - .25) + y_b = 4.078$$

$$\phi := \arcsin\left(\frac{x_c}{l_{ac}}\right) = -7.422 \text{deg}$$

θ_{le} is the angle from the leading cable line to vertical

ψ is the angle from the ac line to vertical

ϕ is the angle from trailing edge line to vertical

x and y positions for leading edge (a), trailing edge (b), and c/4 (c)

l_{ac} line length

Second iteration

$$\theta_{\text{te}} := \theta_{\text{le}} - \phi = 7.422 \cdot \text{deg}$$

$$\psi_{\text{ac}} := \theta_{\text{le}} - \arcsin\left(\frac{l_{\text{te}}^2 + l_{\text{le}}^2 - c^2}{2 \cdot l_{\text{te}} \cdot l_{\text{le}}}\right) = -20.198 \cdot \text{deg}$$

$$x_{\text{ac}} := l_{\text{le}} \cdot \sin(\theta_{\text{le}}) = 0.527$$

$$x_{\text{ac}} := l_{\text{le}} \cdot \cos(\theta_{\text{le}}) = 4.049$$

$$y_{\text{ac}} := l_{\text{te}} \cdot \sin(\psi) = -1.582$$

$$y_{\text{ac}} := l_{\text{te}} \cdot \cos(\psi) = 4.301$$

$$x_{\text{ac}} := (x_a - x_b) \cdot (1 - .25) + x_b = 0$$

$$x_{\text{ac}} := (y_a - y_b) \cdot (1 - .25) + y_b = 4.112$$

$$l_{\text{ac}} := \sqrt{x_c^2 + y_c^2} = 4.112$$

$$\phi_{\text{ac}} := \arcsin\left(\frac{x_c}{l_{\text{ac}}}\right) = 0 \cdot \text{deg}$$

$$\Delta_{\text{te}} := \psi - \phi = -20.198 \cdot \text{deg}$$

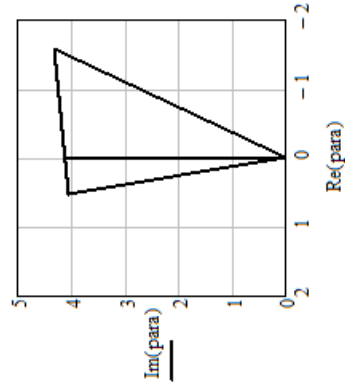
$$i_w := \arctan\left(\frac{y_c - y_b}{x_c - x_b}\right) = -6.82 \cdot \text{deg}$$

$$i_{\text{ac}} := \arctan\left(\frac{y_a - y_b}{x_a - x_b}\right) = -6.82 \cdot \text{deg}$$

$$i_{\text{ac}} := \arctan\left(\frac{l_{\text{ac}} \cdot \cos(\phi) - l_{\text{te}} \cdot \cos(\phi - \Delta_{\text{te}})}{-l_{\text{ac}} \cdot \sin(\phi) - -l_{\text{te}} \cdot \sin(\phi - \Delta_{\text{te}})}\right) = -6.82 \cdot \text{deg}$$

Parachute Preview

$$\text{para} := \left(0 \quad x_a + y_a \cdot \sqrt{-1} \quad x_b + y_b \cdot \sqrt{-1} \quad 0 \quad x_c + y_c \cdot \sqrt{-1}\right)^T$$



Reset θ_{le} definition

x and y positions for leading edge (a), trailing edge (b), and c/4 (c)

Rigging angle (all should be equal)

▢ AoA Prediction

$$\text{ang}_{\text{min}} := -20$$

$$\text{ang}_{\text{max}} := -2$$

$$\text{ind} := 1.. \text{ang}_{\text{max}} - \text{ang}_{\text{min}} + 1$$

$$\text{ang}_{\text{ind}} := (\text{ang}_{\text{min}} - 1) + \text{ind}$$

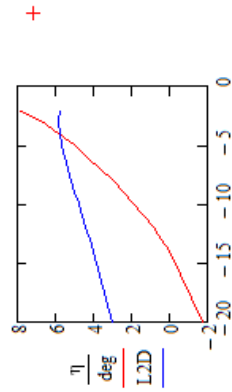
$$\eta_{\text{ind}} := 0 \text{deg}$$

Given

$$\eta = \text{ang-deg} + \text{atan} \left(\frac{1}{\frac{C_L(\eta)}{C_D(\eta)}} \right)$$

$$\eta := \text{Find}(\eta)$$

$$\text{L2D} := \frac{C_L(\eta)}{C_D(\eta)}$$



1	2	3	4	5	6	7	8	...
1	-20	-19	-18	-17	-16	-15	-14	...

ang =

1	2	3	4	5	6	7	8	...
1	-1.729	-1.465	-1.185	-0.899	-0.611	-0.305	0.024	...

η =

·deg

L2D =

1	2	3	4	5	6	7	8	...
1	3.029	3.165	3.309	3.464	3.633	3.813	4.004	...

Minimum analysis angle

Maximum analysis angle

Index for angle variable

Rigging angles to be tested

Eta η represents α in this section to keep the variable unique
Gamma is added since it is positive upwards in this system

▢ AoA Prediction

☑ Lagrangian Equation Energy and Forces Setup

Lagrangian Equation Solution

$$x_1 := x(t) \quad x_2 := x(t) - p \cdot \sin(\phi(t) + i_p) - l_{ac} \cdot \sin(\theta(t))$$

$$y_1 := y(t) \quad y_2 := y(t) + p \cdot \cos(\phi(t) + i_p) + l_{ac} \cdot \cos(\theta(t))$$

$$\dot{x}_{1d} := \frac{d}{dt} x(t) \quad \dot{x}_{2d} := \frac{d}{dt} x(t) - p \cdot \cos(i_p + \phi(t)) \cdot \frac{d}{dt} \phi(t) - l_{ac} \cdot \frac{d}{dt} \theta(t) \cdot \cos(\theta(t))$$

$$\dot{y}_{1d} := \frac{d}{dt} y(t) \quad \dot{y}_{2d} := \frac{d}{dt} y(t) - p \cdot \sin(i_p + \phi(t)) \cdot \frac{d}{dt} \phi(t) - l_{ac} \cdot \frac{d}{dt} \theta(t) \cdot \sin(\theta(t))$$

Kinetic Energy

Includes linear energy from two masses, plus the rotational energy from mass 1.

$$T := \frac{1}{2} m_1 \left(\frac{d}{dt} x_1 \right)^2 + \frac{1}{2} m_1 \left(\frac{d}{dt} y_1 \right)^2 + \frac{1}{2} J_1 \left(\frac{d}{dt} \phi(t) \right)^2 + \frac{1}{2} m_{2x} \left(\frac{d}{dt} x_2 \right)^2 + \frac{1}{2} m_{2y} \left(\frac{d}{dt} y_2 \right)^2$$

$$T := \frac{1}{2} m_1 \left(\frac{d}{dt} x(t) \right)^2 + \frac{1}{2} m_1 \left(\frac{d}{dt} y(t) \right)^2 + \frac{1}{2} J_1 \left(\frac{d}{dt} \phi(t) \right)^2 \dots$$

$$+ \frac{1}{2} m_{2x} \left(\frac{d}{dt} x(t) - p \cdot \cos(i_p + \phi(t)) \cdot \frac{d}{dt} \phi(t) - l_{ac} \cdot \frac{d}{dt} \theta(t) \cdot \cos(\theta(t)) \right)^2 \dots$$

$$+ \frac{1}{2} m_{2y} \left(\frac{d}{dt} y(t) - p \cdot \sin(i_p + \phi(t)) \cdot \frac{d}{dt} \phi(t) - l_{ac} \cdot \frac{d}{dt} \theta(t) \cdot \sin(\theta(t)) \right)^2$$

Potential Energy

Gravitational potential of both mass with their respective heights.

$$V := m_1 \cdot g \cdot y_1 + m_2 \cdot g \cdot y_2$$

$$V := m_1 \cdot g \cdot y(t) + m_2 \cdot g \cdot (y(t) + p \cdot \cos(\phi(t) + i_p) + l_{ac} \cdot \cos(\theta(t)))$$

Lagrangian

This will be used to derive with respect to q, qdot, and qdot/dt.

$$L := T - V$$

$$L := \frac{1}{2} m_1 \left(\frac{d}{dt} x(t) \right)^2 + \frac{1}{2} m_1 \left(\frac{d}{dt} y(t) \right)^2 + \frac{1}{2} J_1 \left(\frac{d}{dt} \phi(t) \right)^2 \dots$$

$$+ \frac{1}{2} m_{2x} \left(\frac{d}{dt} x(t) - p \cdot \cos(i_p + \phi(t)) \cdot \frac{d}{dt} \phi(t) - l_{ac} \cdot \frac{d}{dt} \theta(t) \cdot \cos(\theta(t)) \right)^2 \dots$$

$$+ \frac{1}{2} m_{2y} \left(\frac{d}{dt} y(t) - p \cdot \sin(i_p + \phi(t)) \cdot \frac{d}{dt} \phi(t) - l_{ac} \cdot \frac{d}{dt} \theta(t) \cdot \sin(\theta(t)) \right)^2 - [m_1 \cdot g \cdot y(t) + m_2 \cdot g \cdot (y(t) + p \cdot \cos(\phi(t) + i_p) + l_{ac} \cdot \cos(\theta(t)))]$$

x Equations

$$\frac{\partial}{\partial \frac{d}{dt} \dot{x}(t)} L := \frac{d}{dt} x(t) \cdot m_1 + \frac{d}{dt} x(t) \cdot m_{2x} - m_{2x} p \cdot \cos(\dot{i}_p + \phi(t)) \cdot \frac{d}{dt} \phi(t) - I_{ac} m_{2x} \frac{d}{dt} \theta(t) \cdot \cos(\theta(t))$$

$$\frac{d}{dt} \left(\frac{\partial}{\partial \frac{d}{dt} \dot{x}(t)} L \right) := m_1 \frac{d^2}{dt^2} x(t) + m_{2x} \frac{d^2}{dt^2} x(t) - m_{2x} p \cdot \cos(\dot{i}_p + \phi(t)) \cdot \frac{d^2}{dt^2} \phi(t) - I_{ac} m_{2x} \frac{d^2}{dt^2} \theta(t) \cdot \cos(\theta(t)) + m_{2x} p \cdot \sin(\dot{i}_p + \phi(t)) \cdot \frac{d}{dt} \phi(t) + I_{ac} m_{2x} \frac{d}{dt} \theta(t) \cdot \sin(\theta(t))$$

$$\frac{\partial}{\partial x(t)} L := 0$$

$$\frac{d}{dt} \left(\frac{\partial}{\partial \frac{d}{dt} \dot{x}(t)} L \right) - \frac{\partial}{\partial x(t)} L := m_1 \frac{d^2}{dt^2} x(t) + m_{2x} \frac{d^2}{dt^2} x(t) - m_{2x} p \cdot \cos(\dot{i}_p + \phi(t)) \cdot \frac{d^2}{dt^2} \phi(t) - I_{ac} m_{2x} \frac{d^2}{dt^2} \theta(t) \cdot \cos(\theta(t)) + m_{2x} p \cdot \sin(\dot{i}_p + \phi(t)) \cdot \frac{d}{dt} \phi(t) + I_{ac} m_{2x} \frac{d}{dt} \theta(t) \cdot \sin(\theta(t))$$

y Equations

$$\frac{\partial}{\partial \frac{d}{dt} \dot{y}(t)} L := m_1 \frac{d}{dt} y(t) + m_{2y} \frac{d}{dt} y(t) - m_{2y} p \cdot \sin(\dot{i}_p + \phi(t)) \cdot \frac{d}{dt} \phi(t) - I_{ac} m_{2y} \frac{d}{dt} \theta(t) \cdot \sin(\theta(t))$$

$$\frac{d}{dt} \left(\frac{\partial}{\partial \frac{d}{dt} \dot{y}(t)} L \right) := m_1 \frac{d^2}{dt^2} y(t) + m_{2y} \frac{d^2}{dt^2} y(t) - m_{2y} p \cdot \sin(\dot{i}_p + \phi(t)) \cdot \frac{d^2}{dt^2} \phi(t) - I_{ac} m_{2y} \frac{d^2}{dt^2} \theta(t) \cdot \sin(\theta(t)) - m_{2y} p \cdot \cos(\dot{i}_p + \phi(t)) \cdot \frac{d}{dt} \phi(t) - I_{ac} m_{2y} \frac{d}{dt} \theta(t) \cdot \cos(\theta(t))$$

$$\frac{\partial}{\partial y(t)} L := -g \cdot m_1 - g \cdot m_2$$

$$\frac{d}{dt} \left(\frac{\partial}{\partial \frac{d}{dt} \dot{y}(t)} L \right) - \frac{\partial}{\partial y(t)} L := m_1 \frac{d^2}{dt^2} y(t) - I_{ac} m_{2y} \cos(\theta(t)) \cdot \left(\frac{d}{dt} \theta(t) \right)^2 - m_{2y} p \cdot \cos(\dot{i}_p + \phi(t)) \cdot \left(\frac{d}{dt} \phi(t) \right)^2 + m_{2y} \frac{d^2}{dt^2} y(t) + g \cdot m_1 + g \cdot m_2 - m_{2y} p \cdot \sin(\dot{i}_p + \phi(t)) \cdot \frac{d^2}{dt^2} \phi(t) - I_{ac} m_{2y} \sin(\theta(t)) \cdot \frac{d^2}{dt^2} \theta(t)$$

Generalized Forces

The location to generalized forces are listed below.

$$\mathbf{r}_L := (x(t) - p \cdot \sin(\phi(t) + i_p) - l_{ac} \cdot \sin(\theta(t))) \cdot \mathbf{i} + (y(t) + p \cdot \cos(\phi(t) + i_p) + l_{ac} \cdot \cos(\theta(t))) \cdot \mathbf{j}$$

$$\mathbf{r}_{D_w} := (x(t) - p \cdot \sin(\phi(t) + i_p) - l_{ac} \cdot \sin(\theta(t))) \cdot \mathbf{i} + (y(t) + p \cdot \cos(\phi(t) + i_p) + l_{ac} \cdot \cos(\theta(t))) \cdot \mathbf{j}$$

$$\mathbf{r}_{D_g} := (x(t)) \cdot \mathbf{i} + (y(t)) \cdot \mathbf{j}$$

$$\mathbf{r}_T := (x(t) - l_T \cdot \sin(\phi)) \cdot \mathbf{i} + (y(t) + l_T \cdot \cos(\phi)) \cdot \mathbf{j}$$

The generalized forces are listed below.

$$\mathbf{d}_L := L \cdot (-\sin(\gamma_2) \cdot \mathbf{i} + \cos(\gamma_2) \cdot \mathbf{j})$$

$$\mathbf{d}_{D_w} := D_w \cdot (-\cos(\gamma_2) \cdot \mathbf{i} - \sin(\gamma_2) \cdot \mathbf{j})$$

$$\mathbf{d}_{D_g} := D_g \cdot (-\cos(\gamma_1) \cdot \mathbf{i} - \sin(\gamma_1) \cdot \mathbf{j})$$

$$\mathbf{d}_T := T \cdot (\cos(\phi) \cdot \mathbf{i} + \sin(\phi) \cdot \mathbf{j})$$

The magnitude of the generalized forces are listed below.

$$L := \frac{1}{2} \rho \cdot v^2 \cdot S \cdot C_L$$

$$D_w := \frac{1}{2} \rho \cdot v^2 \cdot S \cdot C_{D_w}$$

$$D_g := \frac{1}{2} \rho \cdot v^2 \cdot A \cdot C_{D_g}$$

$$T := T$$

These are the "variations" given in the MIT document [25]

Lift Equations

$$\frac{\partial}{\partial x} r_L := 1 \cdot i + 0 \cdot j$$

$$\frac{\partial}{\partial y} r_L := 0 \cdot i + 1 \cdot j$$

$$\frac{\partial}{\partial \phi} r_L := (-p \cdot \cos(\phi(t) + i_p)) \cdot i + (-p \cdot \sin(\phi(t) + i_p)) \cdot j$$

$$\frac{\partial}{\partial \theta} r_L := (-l_{ac} \cdot \cos(\theta(t))) \cdot i + (-l_{ac} \cdot \sin(\theta(t))) \cdot j$$

Wing Drag Equations

$$\frac{\partial}{\partial x} r_{Dw} := 1 \cdot i + 0 \cdot j$$

$$\frac{\partial}{\partial y} r_{Dw} := 0 \cdot i + 1 \cdot j$$

$$\frac{\partial}{\partial \phi} r_{Dw} := (-p \cdot \cos(\phi(t) + i_p)) \cdot i + (-p \cdot \sin(\phi(t) + i_p)) \cdot j$$

$$\frac{\partial}{\partial \theta} r_{Dw} := (-l_{ac} \cdot \cos(\theta(t))) \cdot i + (-l_{ac} \cdot \sin(\theta(t))) \cdot j$$

Glider Drag Equations

$$\frac{\partial}{\partial x} r_{Dg} := 1 \cdot i + 0 \cdot j$$

$$\frac{\partial}{\partial y} r_{Dg} := 0 \cdot i + 1 \cdot j$$

$$\frac{\partial}{\partial \phi} r_{Dg} := 0 \cdot i + 0 \cdot j$$

$$\frac{\partial}{\partial \theta} r_{Dg} := 0 \cdot i + 0 \cdot j$$

----- *Thrust Equations* -----

$$\frac{\partial}{\partial x} r_{Dg} := 1 \cdot i + 0 \cdot j$$

$$\frac{\partial}{\partial y} r_{Dg} := 0 \cdot i + 1 \cdot j$$

$$\frac{\partial}{\partial \phi} r_{Dg} := (-1_T \cdot \cos(\phi)) \cdot i + (-1_T \cdot \sin(\phi)) \cdot j$$

$$\frac{\partial}{\partial \theta} r_{Dg} := 0 \cdot i + 0 \cdot j$$

Total Forces

$$Q_x = -L \cdot \sin(\gamma_2) - D_w \cdot \cos(\gamma_2) - D_f \cdot \cos(\gamma_1) + T \cdot \cos(\phi(t))$$

$$Q_y = L \cdot \cos(\gamma_2) - D_w \cdot \sin(\gamma_2) - D_f \cdot \sin(\gamma_1) + T \cdot \sin(\phi(t))$$

$$Q_\phi = L \cdot p \cdot \sin(\gamma_2 - \phi(t) - i_p) + D_w \cdot p \cdot \cos(\gamma_2 - \phi(t) - i_p) - T \cdot 1_T$$

$$Q_\theta = L \cdot 1_{ac} \cdot \sin(\gamma_2 - \theta(t)) + D_w \cdot 1_{ac} \cdot \cos(\gamma_2 - \theta(t))$$

] Lagrangian Equation Energy and Forces Setup

Force Definitions and Alphas

$\alpha 1$: Angle of attack for mass 1

$\alpha 2$: Angle of attack for mass 2

$\alpha 2w$: Angle of attack for mass 2 + incidence angle of wing

$$\gamma_1 := -\text{atan} \left(\frac{\frac{d}{dt}y(t)}{\frac{d}{dt}x(t)} \right) \quad \gamma_2 := -\text{atan} \left(\frac{\frac{d}{dt}y(t) - p \cdot \sin(i_p + \phi(t)) \cdot \frac{d}{dt}\phi(t) - l_{ac} \cdot \frac{d}{dt}\theta(t) \cdot \sin(\theta(t))}{\frac{d}{dt}x(t) - p \cdot \cos(i_p + \phi(t)) \cdot \frac{d}{dt}\phi(t) - l_{ac} \cdot \frac{d}{dt}\theta(t) \cdot \cos(\theta(t))} \right)$$

$$\alpha := -\text{atan} \left(\frac{\frac{d}{dt}y(t) - p \cdot \sin(i_p + \phi(t)) \cdot \frac{d}{dt}\phi(t) - l_{ac} \cdot \frac{d}{dt}\theta(t) \cdot \sin(\theta(t))}{\frac{d}{dt}x(t) - p \cdot \cos(i_p + \phi(t)) \cdot \frac{d}{dt}\phi(t) - l_{ac} \cdot \frac{d}{dt}\theta(t) \cdot \cos(\theta(t))} \right) + \text{atan} \left(\frac{l_{ac} \cdot \cos(\theta) - l_{te} \cdot \cos(\theta - \Delta_{te})}{-l_{ac} \cdot \sin(\theta) - l_{te} \cdot \sin(\theta - \Delta_{te})} \right)$$

$\Delta_{te} := \theta - \theta_{te}$ Calculate beforehand.

$$v_1^2 := \left(\frac{d}{dt}x(t) \right)^2 + \left(\frac{d}{dt}y(t) \right)^2$$

$$v_2^2 := \left(\frac{d}{dt}x(t) - p \cdot \cos(i_p + \phi(t)) \cdot \frac{d}{dt}\phi(t) - l_{ac} \cdot \frac{d}{dt}\theta(t) \cdot \cos(\theta(t)) \right)^2 + \left(\frac{d}{dt}y(t) - p \cdot \sin(i_p + \phi(t)) \cdot \frac{d}{dt}\phi(t) - l_{ac} \cdot \frac{d}{dt}\theta(t) \cdot \sin(\theta(t)) \right)^2$$

$$L := \frac{1}{2} \cdot \rho \cdot v_2^2 \cdot S \cdot C_L \quad D_w := \frac{1}{2} \cdot \rho \cdot v_2^2 \cdot S \cdot C_D \quad D_f := \frac{1}{2} \cdot \rho \cdot v_1^2 \cdot A \cdot C_{Df}$$

▼ Force, Gamma, Alpha Functions

$$\gamma_1(x_{\dot{\text{d}}}, y_{\dot{\text{d}}}) := \operatorname{atan}\left(\frac{y_{\dot{\text{d}}}}{x_{\dot{\text{d}}}}\right)$$

$$\gamma_2(x_{\dot{\text{d}}}, y_{\dot{\text{d}}}, \phi, \phi_{\dot{\text{d}}}, \theta, \theta_{\dot{\text{d}}}) := \operatorname{atan}\left(\frac{y_{\dot{\text{d}}} - p \cdot \sin(i_p + \phi) \cdot \phi_{\dot{\text{d}}} - l_{ac} \cdot \theta_{\dot{\text{d}}} \cdot \sin(\theta)}{x_{\dot{\text{d}}} - p \cdot \cos(i_p + \phi) \cdot \phi_{\dot{\text{d}}} - l_{ac} \cdot \theta_{\dot{\text{d}}} \cdot \cos(\theta)}\right)$$

$$\alpha(x_{\dot{\text{d}}}, y_{\dot{\text{d}}}, \phi, \phi_{\dot{\text{d}}}, \theta, \theta_{\dot{\text{d}}}) := \operatorname{atan}\left(\frac{l_{ac} \cdot \cos(\theta) - l_{te} \cdot \cos(\theta - \Delta_{te})}{-l_{ac} \cdot \sin(\theta) - l_{te} \cdot \sin(\theta - \Delta_{te})}\right) - \gamma_2(x_{\dot{\text{d}}}, y_{\dot{\text{d}}}, \phi, \phi_{\dot{\text{d}}}, \theta, \theta_{\dot{\text{d}}})$$

$$v_1(x_{\dot{\text{d}}}, y_{\dot{\text{d}}}) := \sqrt{x_{\dot{\text{d}}}^2 + y_{\dot{\text{d}}}^2}$$

$$v_2(x_{\dot{\text{d}}}, y_{\dot{\text{d}}}, \phi, \phi_{\dot{\text{d}}}, \theta, \theta_{\dot{\text{d}}}) := \sqrt{(x_{\dot{\text{d}}} - p \cdot \cos(i_p + \phi) \cdot \phi_{\dot{\text{d}}} - l_{ac} \cdot \theta_{\dot{\text{d}}} \cdot \cos(\theta))^2 + (y_{\dot{\text{d}}} - p \cdot \sin(i_p + \phi) \cdot \phi_{\dot{\text{d}}} - l_{ac} \cdot \theta_{\dot{\text{d}}} \cdot \sin(\theta))^2}$$

$$L_{\alpha\alpha}^{\alpha}(x_{\dot{\text{d}}}, y_{\dot{\text{d}}}, \phi, \phi_{\dot{\text{d}}}, \theta, \theta_{\dot{\text{d}}}) := \frac{p}{2} \cdot v_2(x_{\dot{\text{d}}}, y_{\dot{\text{d}}}, \phi, \phi_{\dot{\text{d}}}, \theta, \theta_{\dot{\text{d}}})^2 \cdot S \cdot C_L(\alpha(x_{\dot{\text{d}}}, y_{\dot{\text{d}}}, \phi, \phi_{\dot{\text{d}}}, \theta, \theta_{\dot{\text{d}}}))$$

$$D_w(x_{\dot{\text{d}}}, y_{\dot{\text{d}}}, \phi, \phi_{\dot{\text{d}}}, \theta, \theta_{\dot{\text{d}}}) := \frac{p}{2} \cdot v_2(x_{\dot{\text{d}}}, y_{\dot{\text{d}}}, \phi, \phi_{\dot{\text{d}}}, \theta, \theta_{\dot{\text{d}}})^2 \cdot S \cdot C_D(\alpha(x_{\dot{\text{d}}}, y_{\dot{\text{d}}}, \phi, \phi_{\dot{\text{d}}}, \theta, \theta_{\dot{\text{d}}}))$$

$$D_f(x_{\dot{\text{d}}}, y_{\dot{\text{d}}}) := \begin{cases} 0.22481 \cdot \left[(0.024 \cdot 0.3048 \cdot v_1(x_{\dot{\text{d}}}, y_{\dot{\text{d}}}))^2 + 0.249 \cdot 0.3048 \cdot v_1(x_{\dot{\text{d}}}, y_{\dot{\text{d}}}) \right] & \text{if FlagVal} = 1 \vee \text{FlagVal} = 2 \\ \frac{p}{2} \cdot v_1(x_{\dot{\text{d}}}, y_{\dot{\text{d}}})^2 \cdot A \cdot C_{Df} & \text{otherwise} \end{cases}$$

▲ Force, Gamma, Alpha Functions

<p>2] Lagrangian Equations Entire solution not shown</p>	<p>Lagrange Equations x = OX</p> $m_1 \frac{d^2}{dt^2} x(t) + m_{2X} \frac{d^2}{dt^2} x(t) - m_{2X} p \cos(i_p + \phi(t)) \frac{d^2}{dt^2} \theta(t) - I_{ac} m_{2X} \frac{d^2}{dt^2} \theta(t) \cos(\theta(t)) + m_{2X} p \sin(i_p + \phi(t)) \frac{d}{dt} \phi(t) \frac{d}{dt} x(t) + I_{ac} m_{2X} \frac{d}{dt} \phi(t) \frac{d}{dt} x(t) - D_w \cos(\gamma_2) - D_f \cos(\gamma_1) + I \cos(\phi(t)) \text{ solve, } \frac{d^2}{dt^2} x(t) \rightarrow$ $\frac{d^2}{dt^2} x(t) = \frac{m_{2X} p \sin(i_p + \phi(t)) \left(\frac{d}{dt} \phi(t) \right)^2 + I_{ac} m_{2X} \sin(\theta(t)) \left(\frac{d}{dt} \theta(t) \right)^2 - I \cos(\phi(t)) + D_f \cos(\gamma_1) + D_w \cos(\gamma_2) - m_{2X} p \cos(i_p + \phi(t)) \frac{d^2}{dt^2} \phi(t) - I_{ac} m_{2X} \cos(\theta(t)) \frac{d^2}{dt^2} \theta(t)}{m_1 + m_{2X}}$
<p>y = OY</p>	$m_1 \frac{d^2}{dt^2} y(t) - I_{ac} m_{2Y} \cos(\theta(t)) \left(\frac{d}{dt} \theta(t) \right)^2 - m_{2Y} p \cos(i_p + \phi(t)) \left(\frac{d}{dt} \phi(t) \right)^2 + m_{2Y} \frac{d^2}{dt^2} y(t) + g m_1 + g m_2 - m_{2Y} p \sin(i_p + \phi(t)) \frac{d^2}{dt^2} \theta(t) - I_{ac} m_{2Y} \sin(\theta(t)) \frac{d^2}{dt^2} \theta(t) - D_f \sin(\gamma_1) - D_w \sin(\gamma_2) - D_f \sin(\gamma_1) + I \sin(\phi(t)) \text{ solve, } \frac{d^2}{dt^2} y(t) \rightarrow$ $\frac{d^2}{dt^2} y(t) = \frac{m_{2Y} p \cos(i_p + \phi(t)) \left(\frac{d}{dt} \phi(t) \right)^2 + I_{ac} m_{2Y} \cos(\theta(t)) \left(\frac{d}{dt} \theta(t) \right)^2 + I \sin(\phi(t)) - D_f \sin(\gamma_1) - D_w \sin(\gamma_2) + L \cos(\gamma_2) - g m_1 - g m_2 + m_{2Y} p \sin(i_p + \phi(t)) \frac{d^2}{dt^2} \theta(t) + I_{ac} m_{2Y} \sin(\theta(t)) \frac{d^2}{dt^2} \theta(t)}{m_1 + m_{2Y}}$
<p>$\phi = O\phi$</p>	$I_1 \frac{d^2}{dt^2} \phi(t) + m_{2Y} p^2 \frac{d^2}{dt^2} \phi(t) + m_{2X} p^2 \cos(i_p + \phi(t)) \frac{d^2}{dt^2} \phi(t) - m_{2X} p \cos(i_p + \phi(t)) \frac{d^2}{dt^2} x(t) - m_{2Y} p \sin(i_p + \phi(t)) \frac{d^2}{dt^2} y(t) - g m_2 p \sin(i_p + \phi(t)) - m_{2X} p^2 \cos(i_p + \phi(t)) \sin(i_p + \phi(t)) \left(\frac{d}{dt} \phi(t) \right)^2 + m_{2Y} p^2 \cos(i_p + \phi(t)) \left(\frac{d}{dt} \phi(t) \right)^2$ $D_w p \cos(\gamma_2 - i_p - \phi(t)) - I_1 I + L p \sin(\gamma_2 - i_p - \phi(t)) + m_{2X} p \cos(i_p + \phi(t)) \frac{d^2}{dt^2} x(t) + m_{2Y} p \sin(i_p + \phi(t)) \frac{d^2}{dt^2} y(t) + g m_2 p \sin(i_p + \phi(t)) + m_{2X} p^2 \cos(i_p + \phi(t)) \left(\frac{d}{dt} \phi(t) \right)^2 - m_{2Y} p^2 \cos(i_p + \phi(t)) \left(\frac{d}{dt} \phi(t) \right)^2$ $\frac{d^2}{dt^2} \phi(t) = \frac{I_1 + m_{2Y} p^2 + m_{2X} p^2 \cos(i_p + \phi(t)) - m_{2Y} p^2 \cos(i_p + \phi(t))}{I_1 + m_{2Y} p^2 + m_{2X} p^2 \cos(i_p + \phi(t)) - m_{2Y} p^2 \cos(i_p + \phi(t))} \left(\frac{d}{dt} \phi(t) \right)^2 - m_{2Y} p^2 \cos(i_p + \phi(t)) \frac{d^2}{dt^2} x(t) - \phi(t)$
<p>$\theta = O\theta$</p>	$I_{ac} m_{2Y} \frac{d^2}{dt^2} \theta(t) - g I_{ac} m_{2Y} \sin(\theta(t)) + I_{ac} m_{2X} \cos(\theta(t)) \frac{d^2}{dt^2} \theta(t) - I_{ac} m_{2Y} \cos(\theta(t)) \frac{d^2}{dt^2} x(t) - I_{ac} m_{2Y} \sin(\theta(t)) \frac{d^2}{dt^2} y(t) - I_{ac} m_{2X} \cos(\theta(t)) \left(\frac{d}{dt} \theta(t) \right)^2 \cos(\theta(t)) \sin(\theta(t)) - I_{ac} m_{2Y} \left(\frac{d}{dt} \theta(t) \right)^2 \cos(\theta(t)) \sin(\theta(t)) - I_{ac} m_{2X} p \sin(i_p + \phi(t)) \cos(\theta(t)) \sin(\theta(t)) - m_{2X} p \cos(i_p + \phi(t)) \cos(\theta(t)) \frac{d^2}{dt^2} \phi(t) - m_{2Y} p \sin(i_p + \phi(t)) \frac{d^2}{dt^2} \theta(t) =$ $\frac{D_w \cos(\gamma_2 - \theta(t)) + L \sin(\gamma_2 - \theta(t)) + m_{2X} \cos(\theta(t)) \frac{d^2}{dt^2} x(t) + m_{2Y} \sin(\theta(t)) \frac{d^2}{dt^2} y(t) + g m_2 \sin(\theta(t)) + I_{ac} m_{2X} \left(\frac{d}{dt} \theta(t) \right)^2 \cos(\theta(t)) \sin(\theta(t)) - I_{ac} m_{2Y} \left(\frac{d}{dt} \theta(t) \right)^2 \cos(\theta(t)) \sin(\theta(t)) - m_{2X} p \cos(i_p + \phi(t)) \cos(\theta(t)) \frac{d^2}{dt^2} \phi(t) - m_{2Y} p \sin(i_p + \phi(t)) \frac{d^2}{dt^2} \theta(t) + I_{ac} m_{2Y} + I_{ac} m_{2X} \cos(\theta(t))^2 - I_{ac} m_{2Y} \cos(\theta(t))^2}{I_{ac} m_{2Y} + I_{ac} m_{2X} \cos(\theta(t))^2 - I_{ac} m_{2Y} \cos(\theta(t))^2}$
<p>3] Lagrangian Equations</p>	<p></p>

▢ General Lagrangian Equation Solution

φ and θ equations continued below

Due to the complexity of the system terms will not be able to simplify and must be put into function form. While the solution is no longer visible, it should make the equations easier to work with. An arbitrary variable ψ will be used to represent the variables in the equations in order to reduce any chance of errors. This will follow the convention set in the State Space Conversion section.

$$\begin{aligned}
 \psi_1 &:= x & \psi_3 &:= y & \psi_5 &:= \phi & \psi_7 &:= \theta \\
 \psi_2 &:= \frac{d}{dt}x(t) & \psi_4 &:= \frac{d}{dt}y(t) & \psi_6 &:= \frac{d}{dt}\phi(t) & \psi_8 &:= \frac{d}{dt}\theta(t) \\
 \psi_{d2} &:= \frac{d^2}{dt^2}x(t) & \psi_{d4} &:= \frac{d^2}{dt^2}y(t) & \psi_{d6} &:= \frac{d^2}{dt^2}\phi(t) & \psi_{d8} &:= \frac{d^2}{dt^2}\theta(t) \\
 \frac{d^2}{dt^2}x(t) & & & & & & & \\
 & \frac{m_{2x} \cdot p \cdot \sin(\psi_1 + \psi_5) \cdot (\psi_6)^2 + I_{ac} \cdot m_{2x} \cdot \sin(\psi_7) \cdot (\psi_8)^2 - T \cdot \cos(\psi_5) + D_f \cdot \cos(\gamma_1) + D_w \cdot \cos(\gamma_2) + L \cdot \sin(\gamma_2) - m_{2x} \cdot p \cdot \cos(\psi_1 + \psi_5) \cdot \psi_{d6} - I_{ac} \cdot m_{2x} \cdot \cos(\psi_7) \cdot \psi_{d8}}{m_1 + m_{2x}} \\
 \frac{d^2}{dt^2}y(t) & & & & & & & \\
 & \frac{m_{2y} \cdot p \cdot \cos(\psi_1 + \psi_5) \cdot (\psi_6)^2 + I_{ac} \cdot m_{2y} \cdot \cos(\psi_7) \cdot (\psi_8)^2 + T \cdot \sin(\psi_5) - D_f \cdot \sin(\gamma_1) - D_w \cdot \sin(\gamma_2) + L \cdot \cos(\gamma_2) - g \cdot m_1 - g \cdot m_2 + m_{2y} \cdot p \cdot \sin(\psi_1 + \psi_5) \cdot \psi_{d6} + I_{ac} \cdot m_{2y} \cdot \sin(\psi_7) \cdot \psi_{d8}}{m_1 + m_{2y}} \\
 \frac{d^2}{dt^2}\phi(t) & & & & & & & \\
 & \frac{D_w \cdot p \cdot \cos(\gamma_2 - \psi_1 - \psi_5) - T \cdot I_1 + L \cdot p \cdot \sin(\gamma_2 - \psi_1 - \psi_5) + m_{2x} \cdot p \cdot \cos(\psi_1 + \psi_5) \cdot \psi_{d4} + m_{2y} \cdot p \cdot \sin(\psi_1 + \psi_5) \cdot \psi_{d4} + g \cdot m_2 \cdot p \cdot \cos(\psi_1 + \psi_5) \cdot (\psi_6)^2 - m_{2y} \cdot p \cdot \cos(\psi_1 + \psi_5) \cdot \psi_{d6} + I_{ac} \cdot m_{2x} \cdot \cos(\psi_7) \cdot \psi_{d8} - I_{ac} \cdot m_{2y} \cdot \cos(\psi_7) \cdot \psi_{d8}}{I_1 + m_{2y} \cdot p^2 + m_{2x} \cdot p^2 \cdot \cos(\psi_1 + \psi_5) \cdot \cos(\psi_7)} \\
 \frac{d^2}{dt^2}\theta(t) & & & & & & & \\
 & \frac{D_w \cdot \cos(\gamma_2 - \psi_1) + L \cdot \sin(\gamma_2 - \psi_1) + m_{2x} \cdot \cos(\psi_7) \cdot \psi_{d2} + m_{2y} \cdot \sin(\psi_7) \cdot \psi_{d4} + g \cdot m_2 \cdot \sin(\psi_7) + I_{ac} \cdot m_{2x} \cdot (\psi_8)^2 \cdot \cos(\psi_7) \cdot \sin(\psi_7) - I_{ac} \cdot m_{2y} \cdot p \cdot \cos(\psi_1 + \psi_5) \cdot \cos(\psi_7) \cdot \psi_{d8} - I_{ac} \cdot m_{2y} \cdot \cos(\psi_7) \cdot \psi_{d8}}{I_{ac} \cdot m_{2y} + I_{ac} \cdot m_{2x} \cdot \cos(\psi_7)^2 - I_{ac} \cdot m_{2y} \cdot \cos(\psi_7)^2} \\
 \frac{d^2}{dt^2}x(t) & & & & & & & \\
 & \frac{m_{2y} \cdot p^2 \cdot \cos(\psi_1 + \psi_5) \cdot \sin(\psi_1 + \psi_5) \cdot (\psi_6)^2 + I_{ac} \cdot m_{2x} \cdot p \cdot \cos(\psi_1 + \psi_5) \cdot (\psi_8)^2 \cdot \sin(\psi_7) - I_{ac} \cdot m_{2y} \cdot p \cdot \sin(\psi_1 + \psi_5) \cdot (\psi_8)^2 \cdot \cos(\psi_7) \cdot \psi_{d8} - I_{ac} \cdot m_{2y} \cdot p \cdot \sin(\psi_1 + \psi_5) \cdot \sin(\psi_7) \cdot \psi_{d8}}{I_1 \cdot \cos(\psi_1 + \psi_5)^2 - m_{2y} \cdot p^2 \cdot \cos(\psi_1 + \psi_5)^2} \\
 \frac{d^2}{dt^2}y(t) & & & & & & & \\
 & \frac{I_1 \cdot \cos(\psi_7) \cdot \psi_{d6} - m_{2y} \cdot p \cdot \sin(\psi_1 + \psi_5) \cdot \sin(\psi_7) \cdot \psi_{d6} + m_{2x} \cdot p \cdot \sin(\psi_1 + \psi_5) \cdot (\psi_6)^2 \cdot \cos(\psi_7) - m_{2y} \cdot p \cdot \cos(\psi_1 + \psi_5) \cdot (\psi_6)^2 \cdot \sin(\psi_7)}{I_1 \cdot \cos(\psi_7) \cdot \psi_{d6} - m_{2y} \cdot p^2 \cdot \cos(\psi_1 + \psi_5)^2}
 \end{aligned}$$

		Equations continued below
$\gamma_1(\psi_2, \psi_4)$	$\gamma_2(\psi_2, \psi_4, \psi_5, \psi_6, \psi_7, \psi_8)$	
$I(\psi_2, \psi_4, \psi_5, \psi_6, \psi_7, \psi_8)$	$D_{\mathcal{W}}(\psi_2, \psi_4, \psi_5, \psi_6, \psi_7, \psi_8)$	
$\frac{d^2}{dt^2} x(t)$	$m_{2x} p \sin(\dot{\psi}_p + \psi_5) (\psi_6)^2 - I_{ac} m_{2x} \sin(\psi_7) (\psi_8)^2 - I(\dot{t}) \cos(\psi_5) + D_{\mathcal{W}}(\psi_2, \psi_4, \psi_5, \psi_6, \psi_7, \psi_8) + D_{\mathcal{W}}(\psi_2, \psi_4, \psi_5, \psi_6, \psi_7, \psi_8) + I(\psi_2, \psi_4, \psi_5, \psi_6, \psi_7, \psi_8) \cdot \sin(\gamma_2(\psi_2, \psi_4, \psi_5, \psi_6, \psi_7, \psi_8)) - m_{2x} p \cos(\dot{\psi}_p + \psi_5) \psi_{d6} - I_{ac} m_{2x} \cos(\psi_7)$	
$\frac{d^2}{dt^2} y(t)$	$m_{2y} p \cos(\dot{\psi}_p + \psi_5) (\psi_6)^2 + I_{ac} m_{2y} \cos(\psi_7) (\psi_8)^2 + I(\dot{t}) \sin(\psi_5) - D_{\mathcal{F}}(\psi_2, \psi_4, \psi_5, \psi_6, \psi_7, \psi_8) - I_{ac} m_{2x} \sin(\psi_7) \cos(\psi_2(\psi_2, \psi_4, \psi_5, \psi_6, \psi_7, \psi_8)) - D_{\mathcal{W}}(\psi_2, \psi_4, \psi_5, \psi_6, \psi_7, \psi_8) \cdot \sin(\gamma_1(\psi_2, \psi_4, \psi_5, \psi_6, \psi_7, \psi_8)) - g m_1 - g m_2 + m_{2y} p \sin(\dot{\psi}_p + \psi_5)$	
$\frac{d^2}{dt^2} \phi(t)$	$D_{\mathcal{W}}(\psi_2, \psi_4, \psi_5, \psi_6, \psi_7, \psi_8) p \cos(\gamma_2(\psi_2, \psi_4, \psi_5, \psi_6, \psi_7, \psi_8)) - \dot{\psi}_p - \psi_5) + I(\psi_2, \psi_4, \psi_5, \psi_6, \psi_7, \psi_8) \cdot \sin(\gamma_2(\psi_2, \psi_4, \psi_5, \psi_6, \psi_7, \psi_8)) p \sin(\gamma_2(\psi_2, \psi_4, \psi_5, \psi_6, \psi_7, \psi_8)) - \dot{\psi}_p - \psi_5) + m_{2x} p \cos(\dot{\psi}_p + \psi_5) \psi_{d4} + g m_2 p \sin(\dot{\psi}_p + \psi_5) + m_{2x} p^2 \cos(\dot{\psi}_p + \psi_5) :$	
$\frac{d^2}{dt^2} \theta(t)$	$D_{\mathcal{W}}(\psi_2, \psi_4, \psi_5, \psi_6, \psi_7, \psi_8) \cos(\gamma_2(\psi_2, \psi_4, \psi_5, \psi_6, \psi_7, \psi_8)) - \psi_7) + I(\psi_2, \psi_4, \psi_5, \psi_6, \psi_7, \psi_8) \cdot \sin(\gamma_2(\psi_2, \psi_4, \psi_5, \psi_6, \psi_7, \psi_8)) - \psi_7) + m_{2x} \cos(\psi_7) \psi_{d4} + g m_2 \sin(\psi_7) + I_{ac} m_{2x} (\psi_8)^2 \cos(\psi_7) \sin(\psi_7) - I_{ac} m_{2y} (\psi_8)^2 \cos(\psi_7) \sin(\psi_7) :$	

$$x \cdot p \cos(\dot{\psi}_p + \psi_5) \psi_{d6} - I_{ac} m_{2x} \cos(\psi_7) \psi_{d8}$$

$$I_{ac} m_{2y} + I_{ac} m_{2x} \cos(\psi_7)^2 - I_{ac} m_{2y} \cos(\psi_7)^2$$

$$\psi_5) + m_{2x} p^2 \cos(\dot{\psi}_p + \psi_5) \sin(\dot{\psi}_p + \psi_5) (\psi_6)^2 - m_{2y} p^2 \cos(\dot{\psi}_p + \psi_5) \sin(\dot{\psi}_p + \psi_5) (\psi_8)^2 \cos(\psi_7) - I_{ac} m_{2x} p \cos(\dot{\psi}_p + \psi_5) (\psi_6)^2 \cos(\psi_7) - I_{ac} m_{2y} p \cos(\dot{\psi}_p + \psi_5) (\psi_8)^2 \cos(\psi_7) \sin(\psi_7) \psi_{d8}$$

$$^2 \cdot \cos(\dot{\psi}_p + \psi_5)^2 - m_{2y} p^2 \cos(\dot{\psi}_p + \psi_5)^2$$

$$- m_{2y} (\psi_8)^2 \cos(\psi_7) \sin(\psi_7) - m_{2x} p \cos(\dot{\psi}_p + \psi_5) \cos(\psi_7) \psi_{d6} - m_{2y} p \sin(\dot{\psi}_p + \psi_5) \sin(\psi_7) \psi_{d6} + m_{2x} p \sin(\dot{\psi}_p + \psi_5) (\psi_6)^2 \cos(\psi_7) - m_{2y} p \cos(\dot{\psi}_p + \psi_5) (\psi_6)^2 \sin(\psi_7)$$

Solving the System

	Equations continued below
$a_1(\psi_2, \psi_4, \psi_5, \psi_6, \psi_7, \psi_8, \Gamma) = \frac{m_{2x} p \cdot \sin(\dot{i}_p + \psi_5) \cdot (\psi_6)^2 + I_{ac} m_{2x} \sin(\psi_7) \cdot (\psi_8)^2 - T \cdot \cos(\psi_5)}{-(m_1 + m_{2x})} + D_f(\psi_2, \psi_4, \cos(\gamma_1(\psi_2, \psi_4))) + D_w(\psi_2, \psi_4, \psi_5, \psi_6, \psi_7, \psi_8) \cdot \cos(\gamma_2(\psi_2, \psi_4, \psi_5, \psi_6, \psi_7, \psi_8)) + L(\psi_2, \psi_4, \psi_5, \psi_6, \psi_7)$	
$a_2(\psi_2, \psi_4, \psi_5, \psi_6, \psi_7, \psi_8, \Gamma) = \frac{m_{2y} p \cdot \cos(\dot{i}_p + \psi_5) \cdot (\psi_6)^2 + I_{ac} m_{2y} \cos(\psi_7) \cdot (\psi_8)^2 + T \cdot \sin(\psi_5)}{m_1 + m_{2x}} - D_f(\psi_2, \psi_4) \cdot \sin(\gamma_1(\psi_2, \psi_4)) - D_w(\psi_2, \psi_4, \psi_5, \psi_6, \psi_7, \psi_8) \cdot \sin(\gamma_2(\psi_2, \psi_4, \psi_5, \psi_6, \psi_7, \psi_8)) + L(\psi_2, \psi_4, \psi_5, \psi_6, \psi_7)$	
$a_3(\psi_2, \psi_4, \psi_5, \psi_6, \psi_7, \psi_8, \Gamma) = \frac{D_w(\psi_2, \psi_4, \psi_5, \psi_6, \psi_7, \psi_8) \cdot p \cdot \cos(\gamma_2(\psi_2, \psi_4, \psi_5, \psi_6, \psi_7, \psi_8)) - \dot{i}_p - \psi_5}{m_1 + m_{2x}} - T \cdot \Gamma + L(\psi_2, \psi_4, \psi_5, \psi_6, \psi_7, \psi_8) \cdot p \cdot \sin(\gamma_2(\psi_2, \psi_4, \psi_5, \psi_6, \psi_7, \psi_8)) - \dot{i}_p - \psi_5 + g \cdot m_2 \cdot p \cdot \sin(\dot{i}_p + \psi_5) + m_1$	
$a_4(\psi_2, \psi_4, \psi_5, \psi_6, \psi_7, \psi_8) = \frac{D_w(\psi_2, \psi_4, \psi_5, \psi_6, \psi_7, \psi_8) \cdot \cos(\gamma_2(\psi_2, \psi_4, \psi_5, \psi_6, \psi_7, \psi_8)) \cdot \cos(\psi_7) + L(\psi_2, \psi_4, \psi_5, \psi_6, \psi_7, \psi_8) \cdot \sin(\gamma_2(\psi_2, \psi_4, \psi_5, \psi_6, \psi_7, \psi_8)) - \psi_7}{I_{ac} m_{2x} \cdot \cos(\psi_7)^2 + \frac{I_{ac} m_{2y} \cdot \sin(\psi_7)^2}{m_1 + m_{2x}} + \frac{m_1 + m_{2y}}{m_1 + m_{2x}} - 1} + L(\psi_2, \psi_4, \psi_5, \psi_6, \psi_7, \psi_8) \cdot \sin(\gamma_2(\psi_2, \psi_4, \psi_5, \psi_6, \psi_7, \psi_8)) - \psi_7 + g \cdot m_2 \cdot \sin(\psi_7) + I_{ac} m_{2x} \cdot (\psi_8)^2 \cdot \cos(\psi_7) \cdot \sin(\psi_7) - I_{ac} m_{2y} + I_{ac} m_{2x} \cdot \cos(\psi_7)^2 - I_{ac} m_{2y} \cdot \cos(\psi_7)^2$	
$a_5(\psi_2, \psi_4, \psi_5, \psi_6, \psi_7, \psi_8) = \frac{I_{ac} m_{2x} \cdot \cos(\psi_7)^2}{m_1 + m_{2x}} + \frac{I_{ac} m_{2y} \cdot \sin(\psi_7)^2}{m_1 + m_{2x}} - 1$	
$a_6(\psi_2, \psi_4, \psi_5, \psi_6, \psi_7, \psi_8) = \frac{m_{2x}^2 \cdot p \cdot \cos(\dot{i}_p + \psi_5)^2}{m_1 + m_{2x}} + \frac{m_{2y}^2 \cdot p \cdot \sin(\dot{i}_p + \psi_5)^2}{m_1 + m_{2x}} - 1$	
$a_7(\psi_2, \psi_4, \psi_5, \psi_6, \psi_7, \psi_8) = J_1 + m_{2y} p^2 + m_{2x} p^2 \cdot \cos(\dot{i}_p + \psi_5)^2 - m_{2y} p^2 \cdot \cos(\dot{i}_p + \psi_5)^2$	

	$\frac{I(\psi_2, \psi_4, \psi_5, \psi_6, \psi_7, \psi_8) \cdot \sin(\gamma_2(\psi_2, \psi_4, \psi_5, \psi_6, \psi_7, \psi_8))}{I(\psi_2, \psi_4, \psi_5, \psi_6, \psi_7, \psi_8) \cdot \cos(\gamma_2(\psi_2, \psi_4, \psi_5, \psi_6, \psi_7, \psi_8))} - g \cdot m_1 - g \cdot m_2$
$- \psi_5$	$- m_{2y} \cdot p^2 \cdot \cos(\psi_p + \psi_5) \cdot \sin(\psi_p + \psi_5) \cdot \sin(\psi_6)^2 - m_{2y} \cdot p^2 \cdot \cos(\psi_p + \psi_5) \cdot \sin(\psi_p + \psi_5) \cdot \sin(\psi_6)^2 \cdot \sin(\psi_7) - I_{ac} \cdot m_{2y} \cdot p \cdot \sin(\psi_p + \psi_5) \cdot (\psi_8)^2 \cdot \cos(\psi_7)$
$2y \cdot p^2 + m_{2x} \cdot p^2 \cdot \cos(\psi_p + \psi_5)^2 - m_{2y} \cdot p^2 \cdot \cos(\psi_p + \psi_5)^2$	$+ m_{2x} \cdot p \cdot \cos(\psi_7) + m_{2x} \cdot p \cdot \sin(\psi_p + \psi_5) \cdot \sin(\psi_6)^2 \cdot \cos(\psi_7) - m_{2y} \cdot p \cdot \cos(\psi_p + \psi_5) \cdot (\psi_6)^2 \cdot \sin(\psi_7)$
$- I_{ac} \cdot m_{2x} \cdot \cos(\psi_7)^2$	$- I_{ac} \cdot m_{2y} \cdot \cos(\psi_7)^2$

f_θ and f_ϕ equations continued on next page

$\left[a_3(\psi_2, \psi_4, \psi_5, \psi_6, \psi_7, \psi_8, \Gamma) + \right.$	$\left. \frac{a_1(\psi_2, \psi_4, \psi_5, \psi_6, \psi_7, \psi_8, \Gamma) m_{2x} p \cos(\psi_p + \psi_5) + a_2(\psi_2, \psi_4, \psi_5, \psi_6, \psi_7, \psi_8, \Gamma) m_{2y} p \sin(\psi_p + \psi_5)}{a_1(\psi_2, \psi_4, \psi_5, \psi_6, \psi_7, \psi_8) + a_2(\psi_2, \psi_4, \psi_5, \psi_6, \psi_7, \psi_8)} \right] (m_{2x} p \cos(\psi_p + \psi_5) + m_{2y} p \sin(\psi_p + \psi_5))$
$a_4(\psi_2, \psi_4, \psi_5, \psi_6, \psi_7, \psi_8) +$	$\frac{a_6(\psi_2, \psi_4, \psi_5, \psi_6, \psi_7, \psi_8)}{a_6(\psi_2, \psi_4, \psi_5, \psi_6, \psi_7, \psi_8)}$
$f_\theta(\psi_2, \psi_4, \psi_5, \psi_6, \psi_7, \psi_8, \Gamma) :=$	$\frac{m_{2x}^2 p \cos(\psi_p + \psi_5) \cos(\psi_7) \left[\frac{1_{ac} m_{2x} p \cos(\psi_p + \psi_5) \cos(\psi_7) + 1_{ac} m_{2y} p \sin(\psi_p + \psi_5) \sin(\psi_7)}{m_1 + m_{2x}} \sin(\psi_7) - \frac{1_{ac} m_{2x}^2 p \cos(\psi_p + \psi_5)}{m_1 + m_{2x}} \right] - a_5(\psi_2, \psi_4, \psi_5, \psi_6, \psi_7, \psi_8)}{a_6(\psi_2, \psi_4, \psi_5, \psi_6, \psi_7, \psi_8)}$
$m_{2x} p \cos(\psi_p + \psi_5) \left[a_1(\psi_2, \psi_4, \psi_5, \psi_6, \psi_7, \psi_8, \Gamma) + \right.$	$\left. \frac{1_{ac} m_{2x}^2 f_\theta(\psi_2, \psi_4, \psi_5, \psi_6, \psi_7, \psi_8, \Gamma) \cos(\psi_7)}{m_1 + m_{2x}} \right] + m_{2y} p \sin(\psi_p + \psi_5) \left[a_2(\psi_2, \psi_4, \psi_5, \psi_6, \psi_7, \psi_8) + \frac{1_{ac} m_{2y}^2 f_\theta(\psi_2, \psi_4, \psi_5, \psi_6, \psi_7, \psi_8, \Gamma) \cos(\psi_7)}{m_1 + m_{2x}} \right]$
$a_3(\psi_2, \psi_4, \psi_5, \psi_6, \psi_7, \psi_8, \Gamma) +$	$\frac{m_{2x} p \cos(\psi_p + \psi_5) \left[a_1(\psi_2, \psi_4, \psi_5, \psi_6, \psi_7, \psi_8, \Gamma) + \frac{1_{ac} m_{2x}^2 f_\theta(\psi_2, \psi_4, \psi_5, \psi_6, \psi_7, \psi_8, \Gamma) \cos(\psi_7)}{m_1 + m_{2x}} \right] + m_{2y} p \sin(\psi_p + \psi_5) \left[a_2(\psi_2, \psi_4, \psi_5, \psi_6, \psi_7, \psi_8) + \frac{1_{ac} m_{2y}^2 f_\theta(\psi_2, \psi_4, \psi_5, \psi_6, \psi_7, \psi_8, \Gamma) \cos(\psi_7)}{m_1 + m_{2x}} \right]}{a_3(\psi_2, \psi_4, \psi_5, \psi_6, \psi_7, \psi_8, \Gamma) + a_4(\psi_2, \psi_4, \psi_5, \psi_6, \psi_7, \psi_8)}$
$f_\phi(\psi_2, \psi_4, \psi_5, \psi_6, \psi_7, \psi_8, \Gamma) :=$	$\frac{-m_{2x} p \cos(\psi_p + \psi_5) f_\phi(\psi_2, \psi_4, \psi_5, \psi_6, \psi_7, \psi_8, \Gamma) - 1_{ac} m_{2x} \cos(\psi_7) f_\theta(\psi_2, \psi_4, \psi_5, \psi_6, \psi_7, \psi_8, \Gamma) - (m_1 + m_{2x}) m_{2y} p \sin(\psi_p + \psi_5) f_\phi(\psi_2, \psi_4, \psi_5, \psi_6, \psi_7, \psi_8, \Gamma) + 1_{ac} m_{2y} \sin(\psi_7) f_\theta(\psi_2, \psi_4, \psi_5, \psi_6, \psi_7, \psi_8, \Gamma)}{m_1 + m_{2x}}$
$f_x(\psi_2, \psi_4, \psi_5, \psi_6, \psi_7, \psi_8, \Gamma) := a_1(\psi_2, \psi_4, \psi_5, \psi_6, \psi_7, \psi_8, \Gamma) +$	$\frac{-m_{2x} p \cos(\psi_p + \psi_5) f_\phi(\psi_2, \psi_4, \psi_5, \psi_6, \psi_7, \psi_8, \Gamma) - 1_{ac} m_{2x} \cos(\psi_7) f_\theta(\psi_2, \psi_4, \psi_5, \psi_6, \psi_7, \psi_8, \Gamma) - (m_1 + m_{2x}) m_{2y} p \sin(\psi_p + \psi_5) f_\phi(\psi_2, \psi_4, \psi_5, \psi_6, \psi_7, \psi_8, \Gamma) + 1_{ac} m_{2y} \sin(\psi_7) f_\theta(\psi_2, \psi_4, \psi_5, \psi_6, \psi_7, \psi_8, \Gamma)}{m_1 + m_{2x}}$
$f_y(\psi_2, \psi_4, \psi_5, \psi_6, \psi_7, \psi_8, \Gamma) := a_2(\psi_2, \psi_4, \psi_5, \psi_6, \psi_7, \psi_8, \Gamma) +$	$\frac{-m_{2x} p \cos(\psi_p + \psi_5) f_\phi(\psi_2, \psi_4, \psi_5, \psi_6, \psi_7, \psi_8, \Gamma) - 1_{ac} m_{2x} \cos(\psi_7) f_\theta(\psi_2, \psi_4, \psi_5, \psi_6, \psi_7, \psi_8, \Gamma) - (m_1 + m_{2x}) m_{2y} p \sin(\psi_p + \psi_5) f_\phi(\psi_2, \psi_4, \psi_5, \psi_6, \psi_7, \psi_8, \Gamma) + 1_{ac} m_{2y} \sin(\psi_7) f_\theta(\psi_2, \psi_4, \psi_5, \psi_6, \psi_7, \psi_8, \Gamma)}{m_1 + m_{2x}}$

General Lagrangian Equation Solution

f ₀ equation	$\frac{(m_{2x} \cdot p \cdot \cos(\dot{i}_p + \psi_5) \cdot \cos(\psi_7) + m_{2y} \cdot p \cdot \sin(\dot{i}_p + \psi_5) \cdot \sin(\psi_7))}{m_1 + m_{2x}} + m_{2x} \cdot \cos(\psi_7) \left[a_1(\psi_2, \psi_4, \psi_5, \psi_6, \psi_7, \psi_8, \Gamma) \right]$	$m_{2x} \cdot p \cdot \cos(\dot{i}_p + \psi_5) \left[a_3(\psi_2, \psi_4, \psi_5, \psi_6, \psi_7, \psi_8, \Gamma) + \frac{a_1(\psi_2, \psi_4, \psi_5, \psi_6, \psi_7, \psi_8, \Gamma) \cdot m_{2x} \cdot p \cdot \cos(\dot{i}_p + \psi_5)}{a_7(\psi_2, \psi_4, \psi_5, \psi_6, \psi_7, \psi_8, \Gamma)} \right]$
		$\frac{I_{ac} \cdot m_{2y} + I_{ac} \cdot m_{2x} \cdot \cos(\psi_7)^2 - I_{ac} \cdot m_{2y} \cdot \cos(\psi_7)}{m_1 + m_{2x}}$
	$\frac{p \cdot \cos(\dot{i}_p + \psi_5) \cdot \cos(\psi_7) - \frac{I_{ac} \cdot m_{2y}^2 \cdot p \cdot \sin(\dot{i}_p + \psi_5) \cdot \sin(\psi_7)}{m_1 + m_{2y}}}{m_1 + m_{2x}}$	$\left(m_{2x} \cdot p \cdot \cos(\dot{i}_p + \psi_5) \cdot \cos(\psi_7) + m_{2y} \cdot p \cdot \sin(\dot{i}_p + \psi_5) \cdot \sin(\psi_7) \right) \cdot \left[I_{ac} \cdot m_{2x} \cdot p \cdot \cos(\dot{i}_p + \psi_5) \cdot \cos(\psi_7) + I_{ac} \cdot m_{2y} \cdot p \cdot \sin(\dot{i}_p + \psi_5) \cdot \sin(\psi_7) \right] - \frac{I_{ac} \cdot m_{2x}^2 \cdot p \cdot \cos(\dot{i}_p + \psi_5) \cdot \cos(\psi_7)}{m_1 + m_{2x}}$
	$m_1 + m_{2x}$	$a_6(\psi_2, \psi_4, \psi_5, \psi_6, \psi_7, \psi_8) \cdot a_7(\psi_2, \psi_4, \psi_5, \psi_6, \psi_7, \psi_8)$
f ₀ equation	$- \psi_5, \psi_6, \psi_7, \psi_8, \Gamma) + \frac{I_{ac} \cdot m_{2y} \cdot f_0(\psi_2, \psi_4, \psi_5, \psi_6, \psi_7, \psi_8, \Gamma) \cdot \sin(\psi_7)}{m_1 + m_{2y}} \left. \vphantom{\frac{I_{ac} \cdot m_{2y} \cdot f_0(\psi_2, \psi_4, \psi_5, \psi_6, \psi_7, \psi_8, \Gamma) \cdot \sin(\psi_7)}{m_1 + m_{2y}}} \right] - I_{ac} \cdot m_{2x} \cdot p \cdot f_0(\psi_2, \psi_4, \psi_5, \psi_6, \psi_7, \psi_8, \Gamma) \cdot \cos(\dot{i}_p + \psi_5) \cdot \cos(\psi_7) - I_{ac} \cdot m_{2y} \cdot p \cdot f_0(\psi_2, \psi_4, \psi_5, \psi_6, \psi_7, \psi_8, \Gamma) \cdot \sin(\dot{i}_p + \psi_5) \cdot \sin(\psi_7)$	$a_5(\psi_2, \psi_4, \psi_5, \psi_6, \psi_7, \psi_8) \cdot \left(I_{ac} \cdot m_{2y} + I_{ac} \cdot m_{2x} \cdot \cos(\psi_7)^2 - I_{ac} \cdot m_{2y} \cdot \cos(\psi_7) \right)$
	$a_7(\psi_2, \psi_4, \psi_5, \psi_6, \psi_7, \psi_8)$	

f ₀ equation continued	$\frac{(p + \psi_5) + a_2(\psi_2, \psi_4, \psi_5, \psi_6, \psi_7, \psi_8, \Gamma) \cdot m_{2y} \cdot p \cdot \sin(\dot{i}_p + \psi_5)}{\psi_2, \psi_4, \psi_5, \psi_6, \psi_7, \psi_8} + m_{2y} \cdot \sin(\psi_7) \left[a_3(\psi_2, \psi_4, \psi_5, \psi_6, \psi_7, \psi_8, \Gamma) \right]$	$m_{2y} \cdot p \cdot \sin(\dot{i}_p + \psi_5) \left[a_3(\psi_2, \psi_4, \psi_5, \psi_6, \psi_7, \psi_8, \Gamma) + \frac{a_1(\psi_2, \psi_4, \psi_5, \psi_6, \psi_7, \psi_8, \Gamma) \cdot m_{2x} \cdot p \cdot \cos(\dot{i}_p + \psi_5) + a_2(\psi_2, \psi_4, \psi_5, \psi_6, \psi_7, \psi_8, \Gamma) \cdot m_{2y} \cdot p \cdot \sin(\dot{i}_p + \psi_5)}{a_7(\psi_2, \psi_4, \psi_5, \psi_6, \psi_7, \psi_8, \Gamma)} \right]$
	$m_1 + m_{2x}$	$a_6(\psi_2, \psi_4, \psi_5, \psi_6, \psi_7, \psi_8) \cdot (m_1 + m_{2y})$
	$\frac{2 \cdot p \cdot \cos(\dot{i}_p + \psi_5) \cdot \cos(\psi_7) - \frac{I_{ac} \cdot m_{2y}^2 \cdot p \cdot \sin(\dot{i}_p + \psi_5) \cdot \sin(\psi_7)}{m_1 + m_{2y}}}{m_1 + m_{2x}}$	$\left(m_{2x} \cdot p \cdot \cos(\dot{i}_p + \psi_5) \cdot \cos(\psi_7) + m_{2y} \cdot p \cdot \sin(\dot{i}_p + \psi_5) \cdot \sin(\psi_7) \right) \cdot \left[I_{ac} \cdot m_{2x} \cdot p \cdot \cos(\dot{i}_p + \psi_5) \cdot \cos(\psi_7) - \frac{I_{ac} \cdot m_{2x}^2 \cdot p \cdot \sin(\dot{i}_p + \psi_5) \cdot \sin(\psi_7)}{m_1 + m_{2x}} \right] - \frac{I_{ac} \cdot m_{2y}^2 \cdot p \cdot \sin(\dot{i}_p + \psi_5) \cdot \sin(\psi_7)}{m_1 + m_{2y}}$
		$a_6(\psi_2, \psi_4, \psi_5, \psi_6, \psi_7, \psi_8) \cdot a_7(\psi_2, \psi_4, \psi_5, \psi_6, \psi_7, \psi_8) \cdot (m_1 + m_{2y}) \left[\frac{I_{ac} \cdot m_{2x}^2 \cdot p \cdot \sin(\dot{i}_p + \psi_5) \cdot \sin(\psi_7)}{m_1 + m_{2y}} + 1 \right]$

State Space Conversion & Initial Conditions

State Space Conversions (For Initial Conditions)

$$\begin{aligned}
 x_1 &:= x & x_3 &:= y & x_5 &:= \phi & x_7 &:= \theta \\
 x_2 &:= \frac{d}{dt}x(t) & x_4 &:= \frac{d}{dt}y(t) & x_6 &:= \frac{d}{dt}\phi(t) & x_8 &:= \frac{d}{dt}\theta(t)
 \end{aligned}$$

$$\begin{aligned}
 \gamma_1(x_2, x_4) & & \gamma_2(x_2, x_4, x_5, x_6, x_7, x_8) & & \alpha(x_2, x_4, x_5, x_6, x_7, x_8) \\
 L(x_2, x_4, x_5, x_6, x_7, x_8) & & D_w(x_2, x_4, x_5, x_6, x_7, x_8) & & D_f(x_2, x_4)
 \end{aligned}$$

$$x_2 := 26 \quad x_4 := 0 \quad x_5 := 0 \text{deg} \quad x_6 := 0 \quad x_7 := 0 \text{deg} \quad x_8 := 0$$

State Space definitions

Functions for use with x-defined state space equations

Initial guesses

Given

$$\begin{aligned}
 0 &= f_x(x_2, x_4, x_5, x_6, x_7, x_8, T_{ss}) \\
 0 &= f_y(x_2, x_4, x_5, x_6, x_7, x_8, T_{ss}) \\
 0 &= f_\phi(x_2, x_4, x_5, x_6, x_7, x_8, T_{ss}) \\
 0 &= f_\theta(x_2, x_4, x_5, x_6, x_7, x_8, T_{ss})
 \end{aligned}$$

$$x_6 = 0 \quad x_8 = 0 \quad x_2 > 1$$

$$\begin{pmatrix} x_2 \\ x_4 \\ x_5 \\ x_6 \\ x_7 \\ x_8 \end{pmatrix} := \text{Find}(x_2, x_4, x_5, x_6, x_7, x_8) = \begin{pmatrix} 23.291 \\ -1.729 \\ -0.056 \\ 0 \\ 0.117 \\ 0 \end{pmatrix}$$

State Space Conversion & Initial Conditions

▢ Differential Equation Solver

State Space Conversions (For Numerical Solution)

$$\begin{aligned}
 y_1 &:= x & y_3 &:= y & y_5 &:= \phi & y_7 &:= \theta \\
 y_2 &:= \frac{d}{dt}x(t) & y_4 &:= \frac{d}{dt}y(t) & y_6 &:= \frac{d}{dt}\phi(t) & y_8 &:= \frac{d}{dt}\theta(t) \\
 \gamma_1(y_2, y_4) & & \gamma_2(y_2, y_4, y_5, y_6, y_7, y_8) & & \alpha(y_2, y_4, y_5, y_6, y_7, y_8) & & \\
 L(y_2, y_4, y_5, y_6, y_7, y_8) & & D_w(y_2, y_4, y_5, y_6, y_7, y_8) & & D_f(y_2, y_4) & &
 \end{aligned}$$

Solver

$$D(t, y) := \begin{pmatrix} y_2 \\ f_x(y_2, y_4, y_5, y_6, y_7, y_8, I(t)) \\ y_4 \\ f_y(y_2, y_4, y_5, y_6, y_7, y_8, I(t)) \\ y_6 \\ f_\phi(y_2, y_4, y_5, y_6, y_7, y_8, I(t)) \\ y_8 \\ f_\theta(y_2, y_4, y_5, y_6, y_7, y_8, I(t)) \end{pmatrix}$$

$$\begin{aligned}
 (x_2 \ x_4 \ x_5 \ x_7) &= (23.291 \ -1.729 \ -0.056 \ 0.117) \\
 y_0 &:= (0 \ x_2 \ \text{alt } x_4 \ x_5 \ x_6 \ x_7 \ x_8)^T \\
 S1 &:= \text{rkfixed}(y_0, 0, t_{\text{ss}} + t_{\text{res}}, \text{iter}, D)
 \end{aligned}$$

▢ Differential Equation Solver

State Space definitions

Functions for use with x-defined state space equations

Steady state initial conditions (with step input it applies to the initial thrust value)

Initial conditions for system

Solver inputs

Solvers used are primarily rkfixed and Rkadapt. Rkadapt has broken when calculating step inputs, so rkfixed is used instead.

<p>Read values from output matrix</p> <p>Redefine index bounds to work with origin=1</p> <p>Angle of attack results from solver.</p> <p>Note: Due to naming convention, the AoA functions will not work after this section.</p> <p>Glider body total velocity</p> <p>Wing x, y, and total velocities</p> <p>Connection point x, y, and total velocities</p> <p>Total relative velocity between connection point and glider body</p> <p>Total relative velocity between connection point and wing</p> <p>Parafoil wing lift</p> <p>Parafoil wing drag</p> <p>Glider body drag</p>	<p>Solver Outputs and Calculations</p> <p>$t := S1^{(1)}$ $x := S1^{(2)}$ $y := S1^{(4)}$ $\theta := S1^{(8)}$</p> <p>$x_{dot} := S1^{(3)}$ $y_{dot} := S1^{(5)}$ $\phi_{dot} := S1^{(7)}$ $\theta_{dot} := S1^{(9)}$</p> <p>$i := 1 \dots \text{iter} + 1$</p> <p>Angle of Attack</p> <p>$\alpha_{A_1} := \gamma_1(x_{dot}, y_{dot})$</p> <p>$\alpha_{A_2} := \gamma_2(x_{dot}, y_{dot}, \phi_1, \phi_{dot}, \theta_1, \theta_{dot})$</p> <p>$\alpha_{A_3} := \alpha(x_{dot}, y_{dot}, \phi_1, \phi_{dot}, \theta_1, \theta_{dot})$</p> <p>Velocity</p> <p>$V_{tot_i} := V_1(x_{dot}, y_{dot})$</p> <p>$x_{2dot_i} := x_{dot_i} - p \cdot \cos(\phi_p + \phi_i) \cdot \phi_{dot_i} - I_{ac} \cdot \theta_{dot_i} \cdot \cos(\theta_i)$</p> <p>$y_{2dot_i} := y_{dot_i} - p \cdot \sin(\phi_p + \phi_i) \cdot \phi_{dot_i} - I_{ac} \cdot \theta_{dot_i} \cdot \sin(\theta_i)$</p> <p>$V_{wrtot_i} := V_2(x_{dot_i}, y_{dot_i}, \phi_1, \phi_{dot_i}, \theta_1, \theta_{dot_i})$</p> <p>$x_{pdot_i} := x_{dot_i} - p \cdot \cos(\phi_1 + \phi_p) \cdot \phi_{dot_i}$</p> <p>$y_{pdot_i} := y_{dot_i} - p \cdot \sin(\phi_1 + \phi_p) \cdot \phi_{dot_i}$</p> <p>$V_{ptot_i} := V_1(x_{pdot_i}, y_{pdot_i})$</p> <p>$V_{pb_i} := V_{ptot_i} - V_{tot_i}$</p> <p>$V_{pw_i} := V_{ptot_i} - V_{wrtot_i}$</p> <p>Lift & Drag</p> <p>$Lift_i := L(x_{dot_i}, y_{dot_i}, \phi_1, \phi_{dot_i}, \theta_1, \theta_{dot_i})$</p> <p>$Drag_i := D_w(x_{dot_i}, y_{dot_i}, \phi_1, \phi_{dot_i}, \theta_1, \theta_{dot_i})$</p> <p>$Drag_b_i := D_f(x_{dot_i}, y_{dot_i})$</p> <p>Solver Outputs and Calculations</p>
--	---

Animation Support

Readout Support

```
inv1 := 7.5
time := t_sec
      *****
fps := (iter + 1) / t_iter + 1 = 40
k := FRAME + 1
```

Joint & Body Positions

$$\text{inc}_i := \text{atan} \left(\frac{l_{ac} \cdot \cos(\theta_i) - l_{te} \cdot \cos(\theta_i - \Delta t_e)}{-l_{ac} \cdot \sin(\theta_i) - l_{te} \cdot \sin(\theta_i - \Delta t_e)} \right)$$

$$m_{1x_i} := x_i$$

$$m_{px_i} := m_{1x_i} - p \cdot \sin(\phi_i + i \cdot p)$$

$$m_{2x_i} := m_{px_i} - l_{ac} \cdot \sin(\theta_i)$$

$$a_{x_i} := m_{2x_i} + 0.25 \cdot c \cdot \cos(\text{inc}_i)$$

$$b_{x_i} := m_{2x_i} - 0.75 \cdot c \cdot \cos(\text{inc}_i)$$

$$m_{1y_i} := y_i$$

$$m_{py_i} := m_{1y_i} + p \cdot \cos(\phi_i + i \cdot p)$$

$$m_{2y_i} := m_{py_i} + l_{ac} \cdot \cos(\theta_i)$$

$$a_{y_i} := m_{2y_i} + 0.25 \cdot c \cdot \sin(\text{inc}_i)$$

$$b_{y_i} := m_{2y_i} - 0.75 \cdot c \cdot \sin(\text{inc}_i)$$

Force Vectors

$$dGain := 1$$

$$L_{x_i} := m_{2x_i} - Lift_i \cdot \sin(\gamma_{2_i})$$

$$D_{x_i} := m_{2x_i} - dGain \cdot Drag_i \cdot \cos(\gamma_{2_i})$$

$$D_{fx_i} := m_{1x_i} - dGain \cdot Drag_{b_i} \cdot \cos(\gamma_{1_i})$$

$$T_{lx_i} := m_{1x_i} - l_T \cdot \sin(\phi_i)$$

$$T_{x_i} := T_{lx_i} + T(t_i) \cdot \cos(\phi_i)$$

$$L_{y_i} := m_{2y_i} + Lift_i \cdot \cos(\gamma_{2_i})$$

$$D_{y_i} := m_{2y_i} - dGain \cdot Drag_i \cdot \sin(\gamma_{2_i})$$

$$D_{fy_i} := m_{1y_i} - dGain \cdot Drag_{b_i} \cdot \sin(\gamma_{1_i})$$

$$T_{ly_i} := m_{1y_i} + l_T \cdot \cos(\phi_i)$$

$$T_{y_i} := T_{ly_i} + T(t_i) \cdot \sin(\phi_i)$$

Graph step size	
Index to time conversion	
Animation frames per second	
Animation frame index	
Incidence angle	
Glider body	
Connection point	
Parafoil wing c/4	
LE of parafoil wing	
TE of parafoil wing	
Drag (wing & body) gain factor	
Parafoil wing lift	
Parafoil wing drag	
Glider body drag	
Thrust origin	
Thrust end	

$$fVec_{2_i} := (m_{2x_i} + m_{2y_i} \cdot \sqrt{-1} \quad L_{x_i} + L_{y_i} \cdot \sqrt{-1} \quad m_{2x_i} + m_{2y_i} \cdot \sqrt{-1} \quad D_{x_i} + D_{y_i} \cdot \sqrt{-1})^T$$

$$fVec_{1_i} := (m_{1x_i} + m_{1y_i} \cdot \sqrt{-1} \quad D_{fx_i} + D_{fy_i} \cdot \sqrt{-1})^T$$

$$fVec_{t_i} := (T_{1x_i} + T_{1y_i} \cdot \sqrt{-1} \quad T_{x_i} + T_{y_i} \cdot \sqrt{-1})^T$$

Energy

$$PE_{1_i} := m_1 \cdot g \cdot y_i$$

$$PE_{2_i} := m_2 \cdot g \cdot (y_i + p \cdot \cos(\phi_i) + i_p) + I_{ac} \cdot \cos(\theta_i)$$

$$KE_{1_i} := \frac{1}{2} \cdot m_1 \cdot (V_{tot_i})^2$$

$$KE_{2_i} := \frac{1}{2} \cdot m_2 \cdot (V_{wrtot_i})^2$$

$$TE_{1_i} := PE_{1_i} + KE_{1_i}$$

$$TE_{2_i} := PE_{2_i} + KE_{2_i}$$

Paraglider Lines

$$string_i := [m_{1x_i} + .5 \cos(\phi_i) + (m_{1y_i} + .5 \sin(\phi_i)) \cdot \sqrt{-1} \quad m_{1x_i} + m_{1y_i} \cdot \sqrt{-1} \quad m_{1x_i} - .5 \sin(\phi_i) + (m_{1y_i} + .5 \cos(\phi_i)) \cdot \sqrt{-1} \quad m_{1x_i} + m_{1y_i} \cdot \sqrt{-1} \quad m_{px_i} + m_{py_i} \cdot \sqrt{-1} \quad m_{2x_i} + m_{2y_i} \cdot \sqrt{-1} \quad a_{x_i} + a_{y_i} \cdot \sqrt{-1} \quad b_{x_i} + b_{y_i} \cdot \sqrt{-1}]^T$$

Parafoil wing lift and drag vectors

Glider body drag vector

Thrust vector

▾ Data Logging

Delete Previous Data File

Uses delete flag to determine if an existing data file should be deleted. It is a script that will access the desired data file output location and permanently remove it from the computer.

The program has an issue with reading/writing to the output file if it already existed when trying to output.

Source: Code was created by "A.Non" on the plc user community forums
<https://www.plcusercommunity.com/thread/33532>

FileDeleted(File,WamingFlag,DeleteReadOnly) :=

(File WamingFlag DeleteReadOnly)

Delete := $\begin{cases} \text{FileDeleted}(\text{file},1) & \text{if DeleteFlag} \neq 0 \wedge \text{LogFlag} \neq 0 \\ 0 & \text{otherwise} \end{cases}$

Writes Data to File

Uses logging flag to determine if data should be written to the output file. It first writes the labels for the variables followed by the variables for each time step.

```

labels := ("t" "x1" "y1" "V1total" "xp" "yp" "Vptotal" "x2" "y2" "V2total" "AoA1"
"AoA2" "AoA3" "AoAwing" "Lift" "Drag" "BodyDrag" "Altnude" "Relative Velocity - p1" "Relative Velocity - p2" "x" "y" "phi" "theta" "phi" "theta" "CL" "CD")
headers := WRITEPRN(file,labels) if LogFlag = 0
writeall :=  $\begin{cases} \text{for } i \in 1..1000 \\ \text{Data} \leftarrow (i, x_{dot}, y_{dot}, V_{dot}, x_{pdot}, y_{pdot}, V_{pdot}, x_{2dot}, y_{2dot}, V_{2dot}, V_{wrot}, \gamma_1, \gamma_2, \alpha, \text{Lift}, \text{Drag}, \text{Drag}_b, m_{py}, V_{pb}, V_{pw}, x, y, \phi, \theta, \theta_{dot}, C_D(\alpha_i)) \\ \text{APPENDPRN}(\text{file},\text{Data}) \\ 0 & \text{otherwise} \end{cases}$ 
if LogFlag = 0

```

Table continues for other variable outputs

	1	2	3	4	5	6	7	8	9	10	11	12	13	14	15	16
1	"t"	"x1"	"y1"	"V1total"	"xp"	"yp"	"Vptotal"	"x2"	"y2"	"V2total"	"AoA1"	"AoA2"	"AoAwing"	"Lift"	"Drag"	body Drag
2	0	19.026	0.165	19.027	19.026	0.165	19.027	19.026	0.165	19.027	8.69·10 ⁻³	8.69·10 ⁻³	0.054	3.218	0.612	0.1
3	0.02	19.026	0.165	19.027	19.026	0.165	19.027	19.026	0.165	19.027	8.69·10 ⁻³	8.69·10 ⁻³	0.054	3.218	0.612	0.1
4	0.04	19.026	0.165	19.027	19.026	0.165	19.027	19.026	0.165	19.027	8.69·10 ⁻³	8.69·10 ⁻³	0.054	3.218	0.612	0.1
5	0.06	19.026	0.165	19.027	19.026	0.165	19.027	19.026	0.165	19.027	8.69·10 ⁻³	8.69·10 ⁻³	0.054	3.218	0.612	0.1
6	0.08	19.026	0.165	19.027	19.026	0.165	19.027	19.026	0.165	19.027	8.69·10 ⁻³	8.69·10 ⁻³	0.054	3.218	0.612	0.1
7	0.1	19.026	0.165	19.027	19.026	0.165	19.027	19.026	0.165	19.027	8.69·10 ⁻³	8.69·10 ⁻³	0.054	3.218	0.612	0.1
8	0.12	19.026	0.165	19.027	19.026	0.165	19.027	19.026	0.165	19.027	8.69·10 ⁻³	8.69·10 ⁻³	0.054	3.218	0.612	0.1
9	0.14	19.026	0.165	19.027	19.026	0.165	19.027	19.026	0.165	19.027	8.69·10 ⁻³	8.69·10 ⁻³	0.054	3.218	0.612	0.1
10	0.16	19.026	0.165	19.027	19.026	0.165	19.027	19.026	0.165	19.027	8.69·10 ⁻³	8.69·10 ⁻³	0.054	3.218	0.612	0.1
11	0.18	19.026	0.165	19.027	19.026	0.165	19.027	19.026	0.165	19.027	8.69·10 ⁻³	8.69·10 ⁻³	0.054	3.218	0.612	0.1
12	0.2	19.026	0.165	19.027	19.026	0.165	19.027	19.026	0.165	19.027	8.69·10 ⁻³	8.69·10 ⁻³	0.054	3.218	0.612	0.1
13	0.22	19.026	0.165	19.027	19.026	0.165	19.027	19.026	0.165	19.027	8.69·10 ⁻³	8.69·10 ⁻³	0.054	3.218	0.612	0.1
14	0.24	19.026	0.165	19.027	19.026	0.165	19.027	19.026	0.165	19.027	8.69·10 ⁻³	8.69·10 ⁻³	0.054	3.218	0.612	0.1
15	0.26	19.026	0.165	19.027	19.026	0.165	19.027	19.026	0.165	19.027	8.69·10 ⁻³	8.69·10 ⁻³	0.054	3.218	0.612	0.1
16	0.28	19.026	0.165	19.027	19.026	0.165	19.027	19.026	0.165	19.027	8.69·10 ⁻³	8.69·10 ⁻³	0.054	3.218	0.612	0.1

READPRN(file) =

Copy to Spreadsheet

Variables to output

output = augment(x_dot, y_dot, V_tot, x_p_dot, y_p_dot, V_ptot, x_2_dot, y_2_dot, V_wtot, gamma_1, gamma_2, alpha, Lift, Drag, Drag_b, m_py, V_pb, V_pw, x, y, phi, theta, phi_dot, theta_dot, C_L(alpha), C_D(alpha))

Output table

To copy to spreadsheet right-click on the table and select the option "Select All." Then right-click again and select "Copy Selection." The data is then ready to paste into a spreadsheet.

	1	2	3	4	5	6	7	8
1	23.291	-1.729	23.355	23.291	-1.729	23.355	23.291	-1.729
2	23.291	-1.729	23.355	23.291	-1.729	23.355	23.291	-1.729
3	23.291	-1.729	23.355	23.291	-1.729	23.355	23.291	-1.729
4	23.291	-1.729	23.355	23.291	-1.729	23.355	23.291	-1.729
5	23.291	-1.729	23.355	23.291	-1.729	23.355	23.291	...

output =

Verification

	1
1	0
2	0.025
3	0.05
4	0.075
5	0.1
6	0.125
7	0.15
8	0.175
9	0.2
10	0.225
11	0.25
12	0.275
13	0.3
14	0.325
15	0.35
16	...

t =

	1
1	23.291
2	23.291
3	23.291
4	23.291
5	23.291
6	23.291
7	23.291
8	23.291
9	23.291
10	23.291
11	23.291
12	23.291
13	23.291
14	23.291
15	23.291
16	...

x_{dot} =

	1
1	-1.729
2	-1.729
3	-1.729
4	-1.729
5	-1.729
6	-1.729
7	-1.729
8	-1.729
9	-1.729
10	-1.729
11	-1.729
12	-1.729
13	-1.729
14	-1.729
15	-1.729
16	...

y_{dot} =

	1
1	23.355
2	23.355
3	23.355
4	23.355
5	23.355
6	23.355
7	23.355
8	23.355
9	23.355
10	23.355
11	23.355
12	23.355
13	23.355
14	23.355
15	23.355
16	...

V_{tot} =

	1
1	50
2	49.957
3	49.913
4	49.87
5	49.827
6	49.784
7	49.74
8	49.697
9	49.654
10	49.611
11	49.567
12	49.524
13	49.481
14	49.438
15	49.394
16	...

y =

Control

Geometric and Starting Constraints

$$l_e = \frac{49}{12}$$

$$l_{te} = \frac{55}{12}$$

$$alt = 50$$

Response Conditions

$$t_{ss} = 5 \quad T_{ss} = 0.75$$

$$t_{res} = 20 \quad T_{res} = 0$$

$$T(t) = \begin{cases} T_{ss} & \text{if } 0 \leq t \leq t_{ss} \\ T_{res} & \text{otherwise} \end{cases}$$

Solver & Model Control

$$iter = 999$$

$$FlagVal = 0$$

Data Logging

$$LogFlag = 0$$

$$file = "C:\Users\Colin\Desktop\Thesis Aux\DataOut\output.txt"$$

$$DeleteFlag = 1$$

Quick Look

$$simOut := \begin{pmatrix} \frac{i_w}{deg} & T_{ss} & V_{tot1} & x_{pdot1} & y_{pdot1} & \frac{\theta_1}{deg} & \frac{\phi_1}{deg} & \frac{c_1}{deg} & \frac{Lift_1}{deg} & \frac{Drag_1}{deg} \end{pmatrix}$$

$$simOut = (-6.82 \quad 0.75 \quad 23.355 \quad 23.291 \quad -1.729 \quad 6.729 \quad -3.217 \quad 4.153 \quad 5.403)$$

Control

Leading edge line length. To use inches divide by 12.

Trailing edge line length. To use inches divide by 12.

Starting altitude

Duration of and thrust applied in steady-state phase

Duration of and thrust applied in response phase

Applies thrust settings to program

Controls the finess of differential equation solver solution

Sets program for a validation mode described by the validation section of the paper.

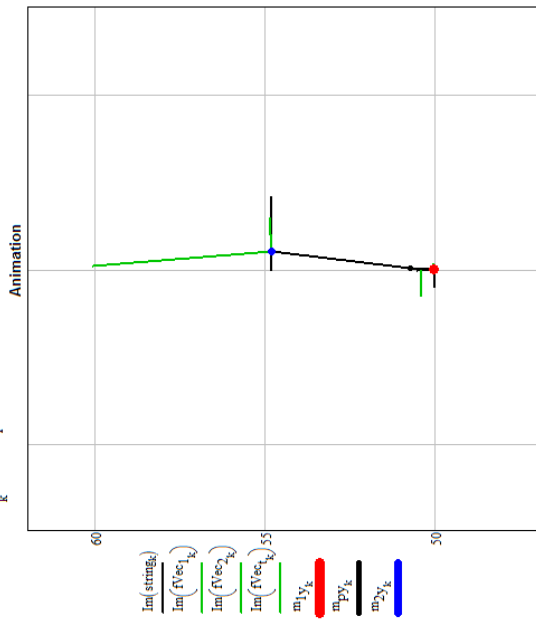
Inputs: Off(0), Calculated CL/CD method values(1), Function method values(2)

Enables(1)/Disables(0) data logging

Data file path

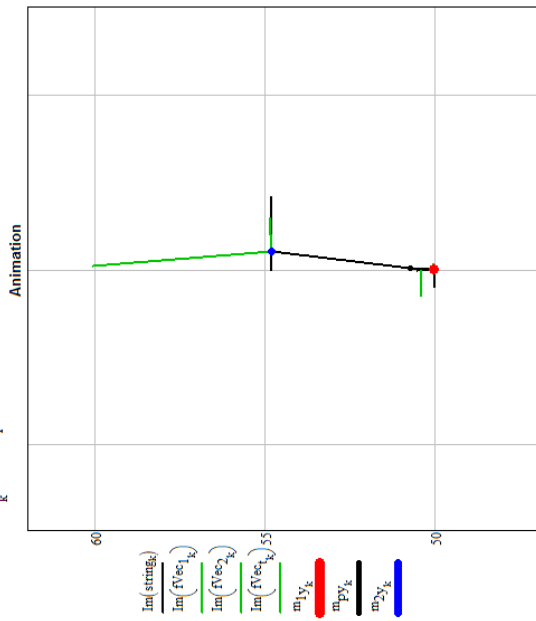
Enables(1)/Disables(0) deletion of previous log file before writing new

$t_{\text{time}_k} = 0 \text{ s}$ $\text{fps} = 40$



$\text{Im}(f(\text{string}_k))$
 $\text{Im}(f(\text{vec}_k))$
 $\text{Im}(f(\text{vec}_2_k))$
 $\text{Im}(f(\text{vec}_3_k))$

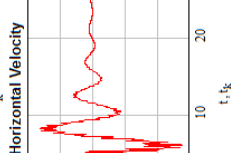
m_{y_k}
 m_{py_k}
 m_{dy_k}



Flight Path

m_{px}, m_{py}
 x_{pdot_k}
 $x_{\text{pdot}_k, 22}$

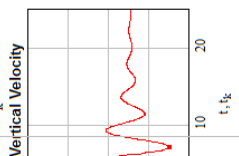
$x_{\text{pdot}_k} = 23.291$



Horizontal Velocity

x_{pdot_k}
 $x_{\text{pdot}_k, 22}$

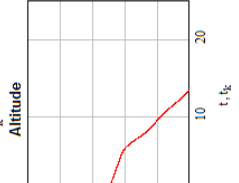
$y_{\text{pdot}_k} = -1.729$



Vertical Velocity

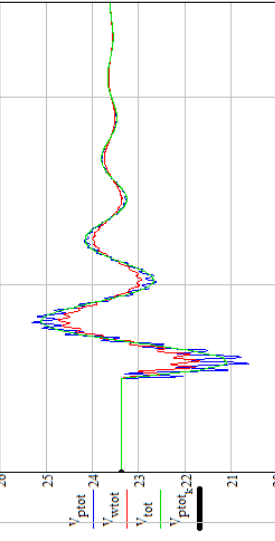
y_{pdot_k}
 $y_{\text{pdot}_k, 22}$

$m_{py_k} = 50.707$



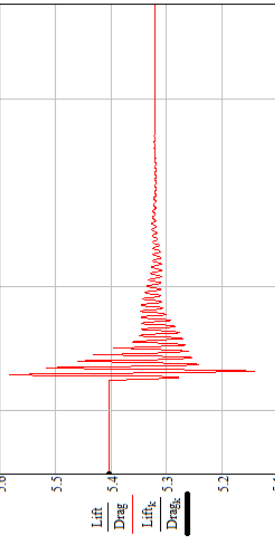
Altitude

Total Velocities



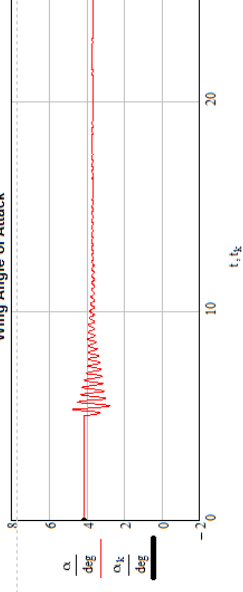
V_{tot}
 V_{wrot}
 V_{pdot}
 $V_{\text{pdot}, 22}$

Lift/Drag Ratio



Lift
 Drag
 Lift_k
 Drag_k

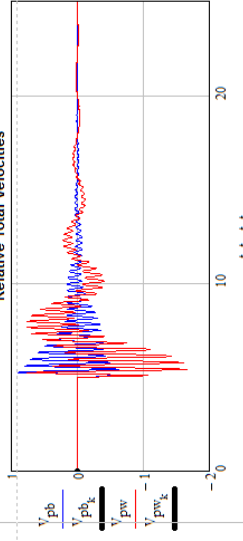
$\alpha_k = 4.153 \text{ deg}$



Wing Angle of Attack

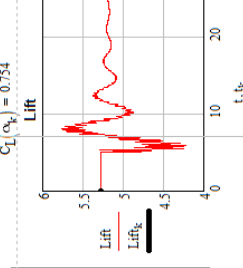
$\frac{\alpha}{\text{deg}}$
 $\frac{\alpha_k}{\text{deg}}$

Relative Total Velocities



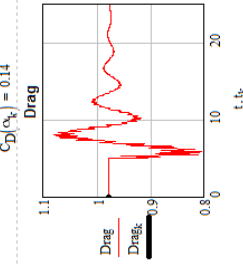
V_{pb}
 V_{pbk}
 V_{pw}
 V_{pwk}

$C_L(\alpha_k) = 0.754$



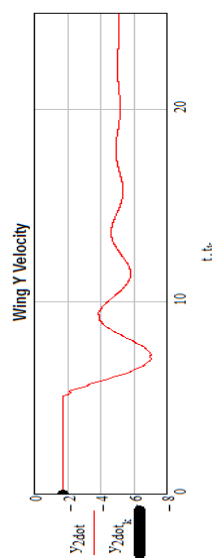
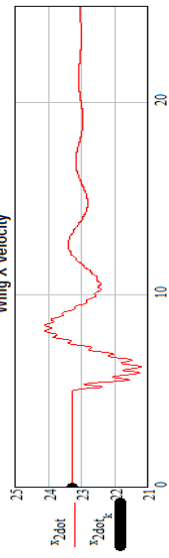
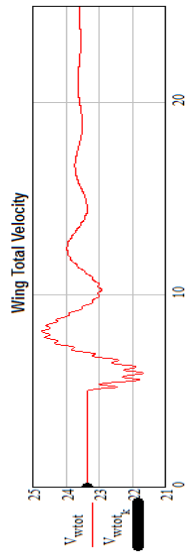
Lift
 Lift_k

$C_D(\alpha_k) = 0.14$

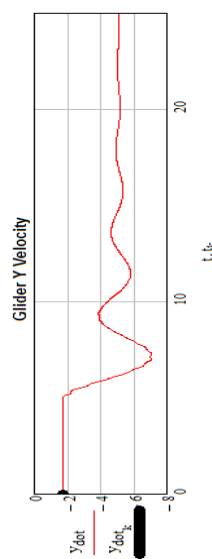
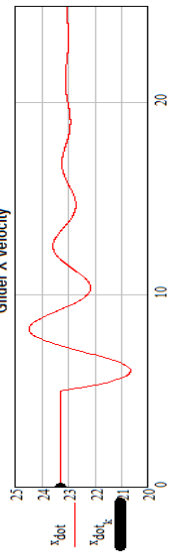
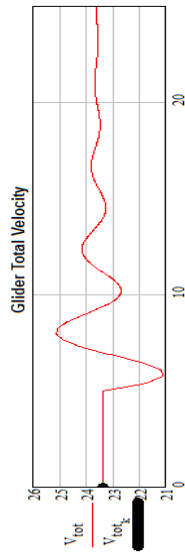


Drag
 Drag_k

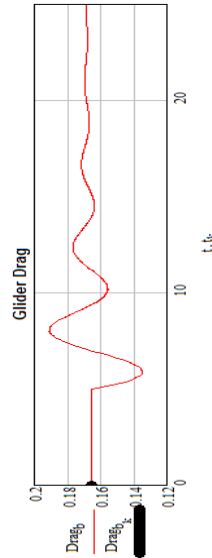
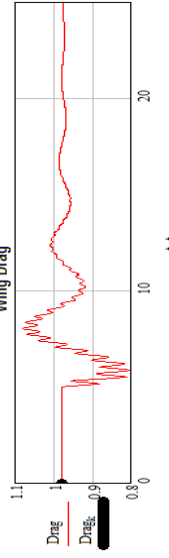
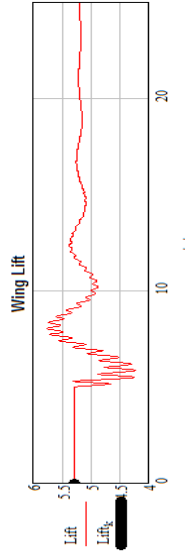
Variables



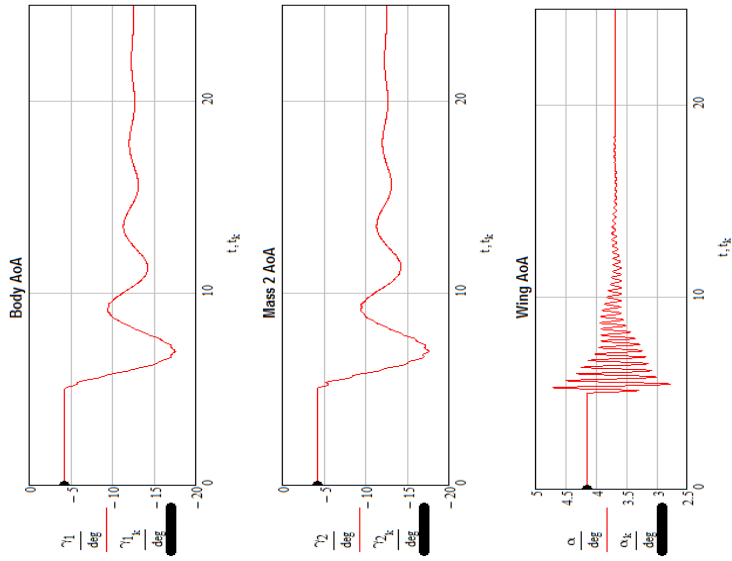
$\text{mean}(V_{tot}) = 23.486$
 $\text{mean}(x_{dot}) = 23.024$
 $\text{mean}(y_{dot}) = -4.384$



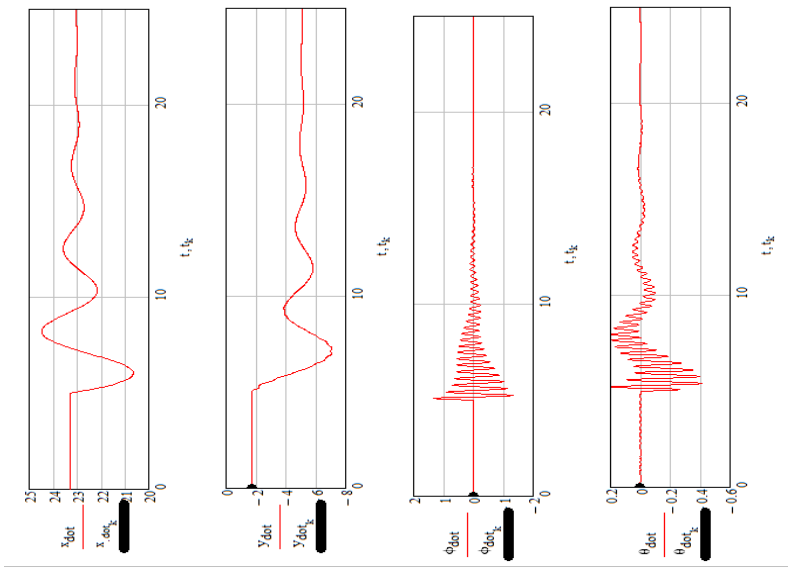
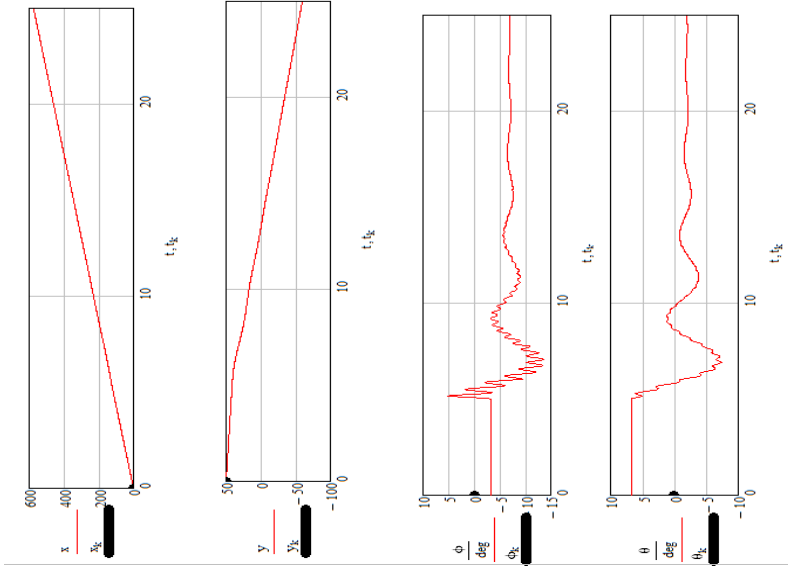
$\text{mean}(V_{tot}) = 23.46$
 $\text{mean}(x_{dot}) = 22.997$
 $\text{mean}(y_{dot}) = -4.385$



$\text{mean}(Lift) = 5.181$
 $\text{mean}(Drag) = 0.971$
 $\text{mean}(Drag_k) = 0.167$



mean(γ_1) = -10.776 deg
 mean(γ_2) = -10.762 deg
 mean(α) = 3.774 deg



Variables

VITA

Colin P. Gibson

Candidate for the Degree of

Master of Science

Thesis: POWERED PARAGLIDER LONGITUDINAL DYNAMIC MODELING AND
EXPERIMENTATION

Major Field: Aerospace Engineering

Biographical:

Education:

Completed the requirements for the Master of Science in Mechanical and
Aerospace Engineering at Oklahoma State University, Stillwater, Oklahoma in
December, 2016.

Completed the requirements for the Bachelor of Science in Mechanical and
Aerospace Engineering at Oklahoma State University, Stillwater, Oklahoma in
May, 2016.

Experience:

Graduate Teaching Assistant: Computer-Aided Design, Compressible Fluid
Flow

Graduate Research Assistant: Design and Fabrication assistant for Bandit, 2014-
2015